The Pennsylvania State University

The Graduate School

Intercollege Graduate Program in Materials

OPTIMIZATION OF MATCHING LAYER DESIGN FOR MEDICAL ULTRASONIC TRANSDUCER

A Dissertation in

Materials

by

Jie Zhu

Submitted in Partial Fulfillment
of the Requirements
for the Degree of

Doctor of Philosophy

August 2008

The dissertation of Jie Zhu was reviewed and approved* by the following:

Wenwu Cao
Professor of Mathematics and Material Science
Dissertation Advisor
Chair of Committee

L. Eric Cross
Evan Pugh Professor Emeritus of Electrical Engineering

Bernhard R. Tittmann
Schell Professor and Professor of Engineering Science and Mechanics

Clive A. Randall
Professor of Materials Science and Engineering

James P. Runt
Professor of Polymer Science
Associate Head for Graduate Studies

*Signatures are on file in the Graduate School

ABSTRACT

This thesis work contains two major parts. In the first part, ultrasonic wave propagation in multilayer structure is investigated. Delaminations between ceramic and electrode layers in multilayer capacitors and multilayer actuators are common defects, which are difficult to detect using traditional ultrasonic imaging method if the size is smaller than 50 microns in diameter. The T-Matrix method is used to treat wave attenuation in periodic structures with alternating ceramic and electrode layers. Multiple penny-shaped delaminations are assumed perpendicular to the incidence wave, and the forward scattering amplitude of the wave from delaminations is calculated by substituting the average effective crack opening displacement into the scattered wave displacement. The effective phase velocity, wave amplitude and the attenuation coefficient have been calculated for different crack densities. The results provide a theoretical base for potential attenuation based ultrasonic non-destructive evaluation (NDE) method.

The second part is a study on matching layers. Matching layers are crucial components in ultrasonic transducers for medical imaging. Without proper matching layers, large acoustic impedance mismatch between piezoelectric resonator and the human body tissue will cause most of the ultrasound energy to be reflected at the interface. For a given frequency, the matching layer thickness should be one quarter of the wavelength and its acoustic impedance should be the geometric mean of the acoustic impedances of piezoelectric material and the imaging body. There are no natural materials that can precisely meet such requirements. Therefore, solid particle/polymer composites are commonly used as matching layer materials. The acoustic impedance of

such composites is generally in the range of 2-15 MRayls. It is a routine task to make such composite for low frequency transducers, but for transducers with operating frequency higher than 40 MHz, the powder size must be sub-microns in order to reduce wave scattering because the wavelength is much smaller. High volume loading fine powder composite is very difficult to make using conventional composite fabrication technique because air bubbles will be trapped in the mixture. Therefore, all ultrahigh frequency transducers currently used or under development are not properly matched because the lacking of desired matching layer materials. This problem hinders the development of finer resolution ultrahigh frequency ultrasonic imaging.

There are some progress made in the past 3 years and there are sol-gel SiO_2/polymer nano-composites being developed that can have acoustic impedance up to 5.7 MRays. In this thesis work, TiO_2 nano-structured material has been developed. The material has porous nano-structure with the volume fraction of voids being controlled by the amount of bonding amorphous phase in the material and its acoustic impedance can be further tuned by heat treatment at slightly elevated temperatures. Using the quarter wavelength thickness characterization method, the acoustic properties of this nano-structured material were accurately characterized. It was found that the acoustic impedance can reach as high as 7.19 MRayls, which is a concrete improvement compared to that of the best nano-composites available.

Because of recent rapid development of the single crystal PMN-PT and PZT-PT materials for medical ultrasonic transducer applications, there is a new excitement to develop transducers with very broad bandwidth because the electromechanical coupling coefficient of these single crystals are better than 90%. For such very broad bandwidth transducers, the front matching layer will be the limiting factor because the quarter wavelength matching layer acts like a filter whose bandwidth is generally less than 100%. One of the main tasks of this thesis is to investigate matching layer design with gradient acoustic impedance to achieve much broader bandwidth (> 100%). Wave propagation within an inhomogeneous multilayer structure has been analyzed and simulated using the finite difference time domain numerical technique. By adjusting the acoustic impedance distribution function, we have found the best gradient design which has super broad bandwidth. In fact, the passband only has a low frequency cut-off and it works for almost all frequencies beyond the cut-off frequency. To certain extend, this optimized design is universal so that such a matching layer can be used in all medical transducers of different frequencies.

TABLE OF CONTENTS

LIST OF FIGURES

LIST OF TABLES

ACKNOWLEDGEMENTS

Graduate study at the Pennsylvania State University has been a long and arduous journey for me. People here make Penn State a special place and I would like to thank those who helped me completing this journey.

Fist of all, I would like to begin by expressing my sincere appreciation to my thesis advisor, Prof. Wenwu Cao. He’s a brilliant researcher who has given me invaluable academic and personal growth guidance. Without his insightful advice, continuous instruction and encouragement throughout my graduate study, this thesis would never become a reality.

I am deeply grateful for having an excellent thesis committee. Prof. Clive Randall has given me a lot of help in improving my academic knowledge on dielectric materials and some physical concepts. Prof. L. Eric Cross and Prof. Bernhard R. Tittmann also provided insightful comments and valuable suggestions.

Although it is impossible to thank everyone who helped me for my thesis research work, I would like to give special thanks to: Dr. Wenhua Jiang, Ms. Bei Jiang, Dr. Haifeng Wang, Dr. Rui Zhang and Dr. Qifa Zhou. I am grateful for their help and assistance in carrying out many experimental works, it's indeed an honor to work with all of these wonderful people.

I want to thank the NSF Center for Dielectric Studies and the National Institute of Health for providing financial support through a center project grant and the grant #P41 EB2182-10. I also want to thank the Penn State University and the Department of

Materials Science and Engineering for their support in various matters relating to my thesis research and graduate studies.

Finally, I wish to dedicate this thesis to my parents and my wife for their genuine support while I pursue this Ph.D degree. My parents have always been there for me for all these years. Without their love and encouragement I would not be where I am today. Their confidence gave me the strength to overcome many difficulties and to aim at high goals in life. Thanks to my wife Lei for her love, sacrifice and patience with me in the last 6 years. I am fortunate to have such a companion in my life and I hope I have also made you proud.

Chapter 1

INTRODUCTION

1.1 MLCC and Delaminations

In multilayer structures, such as multilayer ceramic capacitor (MLCC), delaminations are considered detrimental to the electrical properties and mechanical integrity since they separate the electrode and ceramic layers. During fabrication, thermal mismatch between metal electrodes, ceramic dielectric and the termination material can lead to delaminations as a result of interfacial thermal stresses [Chan, et al. 1995]. Current non-destructive evaluation (NDE) methods for detecting delaminations in MLCC include speckle correlation [Chan, et al. 1995], X-ray radiography [Spiiggs, Cronshagen, 1976], neutron radiography [Cozzolino, et al. 1978], acoustics microscopy [Love, Ewell 1978] and acoustic emission [Kahn, Checkaneck 1983]. These methods are limited in terms of resolution and penetration depth.

Conventional ultrasonic imaging technology uses the time delay of reflected pulses from delaminations to form an image of defects. This strategy has limited resolution because the reflection of ultrasonic waves only occurs when the defect size is comparable to or greater than the wavelength. If the defect size is much smaller than the wavelength, there will be no reflected plane waves but only scattered waves. On the other hand, smaller wavelength ultrasound waves, (such as GHz ultrasonic waves) cannot penetrate deep enough into the structure because of strong attenuation. Therefore, defects smaller than 50 μm are generally invisible to the reflection wave based ultrasonic inspection methods. Detecting such small defects, however, is very critical for preventing device failure, especially since the layer thickness is already down to the microns.

1.2 Medical Ultrasonography

Medical Ultrasonography is one of the most popular medical imaging methods nowadays. Ultrasound pulses travel through the imaging body, form echoes from the imperfection and tissue interfaces, the echoes can be used to construct an image of the targeted area through advanced data processing.

Medical ultrasonography has various notable strengths: Its real-time "live" imaging capability quickens diagnosis procedure [Pavlin and Foster 1995]; it is noninvasive so normally does not cause any discomfort and long-term side effects. [Shung, Smith and Tsui 1992]; the operating cost is relatively low compared to computed X-ray tomography (CT) and magnetic resonance imaging (MRI) [Zagzebski 1996]; also the equipments are comparatively small and portable, which leads to less limitation to the examination location [Shung and Zipparo 1996].

New applications for medical ultrasonography have been developed during the last two decades. The sensitivity of an ultrasonography system depends on its lateral resolution, which can be estimated by:

$$\text{Resolution} = \frac{\text{Wavelength}}{\text{Center frequency}} * \text{F} - \text{number} \quad \text{(Eq. 1-1)}$$

Where F-number is the transducer's focal length to diameter ratio. The recently emergence of new intravascular applications, such as ophthalmological imaging, determatological imaging and mammography imaging require better imaging capability (resolution smaller than 50μm), hence high frequency ultrasonic transducers (30-100MHz and even higher) are needed [Error! Not a valid link.] for disease diagnosis and monitoring improvement of medical treatments. Those transducers provide better resolution in both the axial and lateral directions and are suitable for clinical imaging.

Fig. **1-1**: Ultrasonic diagnostic system and transducer. [www.medical.philips.com]

1.3 Matching Layers for High Frequency Ultrasonic Transducer

Ultrasonic waves produced by probe-cased piezoelectric transducers are focused and sent into human body through matching layer and liquid-based coupling material. Those ultrasonic waves are longitudinal waves [Hoskins, Thrush, et al 2003]. When the adjacent particles move away from each other, the region will become rarefactive. After the adjacent particles move toward each other, the region will become compressive. The wave frequency is the number of wave peaks passing through a fixed point per second. It is determined by the source of waves. Human ears can detect sound waves with frequencies in the range of 20 to 20000Hz. Any other wave with higher frequency than that is called ultrasonic wave. Commonly ultrasonic waves used in medical ultrasonography are between 2-10 MHz. Wave direction and focus point can be adjusted by using phased array technique. The sound speed depends on the density and stiffness of propagating medium. It is relatively low in gas and high in solids with liquids in the middle. The traveling wave will be partially reflected at each boundary between different body tissues having acoustic impedance difference. Those reflected signals are collected by transducer to form the final image. The acoustic impedance Z of a medium is analogous to the electrical impedance and is defined as the product of the velocity and density.

A lot of research have been done on piezoelectric ceramic (PZT), piezocomposite materials and the design of high frequency transducers in the past. However, another crucial component in medical imaging ultrasonic transducer – the matching layer, did not get enough attention. It is known that the quarter wavelength matching layers between piezoelectric material and imaging medium are critical for the performance of high sensitivity transducers because the wave can not be sent into the imaging body when there is a large difference between the piezoelectric resonator and the body tissue [Shung and Zipparo 1996]. Table **1-1** shows the acoustic parameters of some biological and non-biological materials. Without one or multiple proper matching layers, the huge acoustic impedance mismatch will cause 80% of the ultrasound energy being reflected at the interface of piezoelectric resonator and human body tissue [Xiang and Zhang 1995]. For single frequency transducers, such reflection greatly reduces the power efficiency and sensitivity. For a broadband transducer, in addition to the reduced sensitivity, a long ringdown can be produced, which will reduce the resolution if the backing material does not absorb the reflected energy. Traditional modeling techniques, like the Mason Equivalent Circuit [Mason 1964], Wave Guide and Krimholtz-Lee-Mathaei Equivalent Circuit [Krimholtz, Leedom and Mathaei 1971] have been conducted by many researchers on ultrasonic transducer and matching layer design. Theoretically, if the transducer is designed with lossy backing layer, the best acoustic impedance Z_m of the matching layer should be the geometric mean of the piezoelectric material (Z_p) and the imaging tissue (Z_t) [Alvarez-Arenas 2004]:

$$Z_m = \sqrt{Z_p Z_t} \qquad \text{(Eq 1-2)}$$

For air backed broadband transducer with finite piezoelectric section, the optimized acoustic impedance of the matching layer can be set at [Goll and Auld 1975] [DeSilets, Fraser and Kino 1978]:

$$Z_m = Z_p^{1/3} Z_t^{2/3} \qquad \text{(Eq 13)}$$

Commonly used matching layer design sets the thickness at the quarter wavelength of the center frequency of a broadband transducer with the acoustic impedance in the range of 3-15 MRayl, depending on the type of the piezoelectric material. There are no natural materials can meet these requirements, therefore, solid particle polymer composites are widely used for this purpose [Zhou, Cha et al. 2006].Although a routine fabricating process, making such composites became extremely challenging for the case of ultra high frequency transducers [Error! Not a valid link.]. Because the thickness of the quarter wavelength is less than 10μm, the composite particle size is required to be much less than 1μm in order for the composite to behave like a single phase material to avoid wave scattering. The lack of desired materials hinders the development of high frequency medical ultrasonic imaging.

1.4 The Objectives

In order to investigate wave propagation in MLCC containing multiple delaminations, the T-matrix technique is used to describe the wave transmission in multilayer periodic structures. The scattering of incident wave by multiple delaminations is treated by the scattering theory. To find suitable matching layer materials for ultra high frequency medical ultrasonic transducers, a novel TiO_2 nano-structured material with higher acoustic impedance than that of SiO_2 nano-composite and with a simplified processing procedure has been developed in this thesis work. Acoustic impedance property of this porous nano-structured material can be adjusted by controlling the total volume fraction of voids. Subsequently, by using the quarter wavelength thickness characterization method [Wang and Cao 2004; Zhu and Cao 2007], acoustic properties of this nano-structured material have been accurately characterized. Gradient acoustic impedance matching is another technique for improving the matching layer design. We found that such design can lead to great improvement on transducer sensitivity, transmission efficiency and especially improved bandwidth. In this thesis work, gradient acoustic impedance matching layer design and new nano materials are studied in theoretical and simulation work to get a better understanding on advanced matching layer optimization for medical ultrasonic transducers.

Table 1-1: Acoustic parameters of typical materials [Angelsen 2000].

Materials	Mass Density kg/m^3	Compressibility $10^{-12} m^2/Nt$	Sound Speed m/s	Acoustic Impedance MRayls
Biological Materials:				
Fat	950	508	1440	1.37
Neurons	1030	410	1540	1.59
Blood	1025	396	1570	1.61
Kidney	1040	396	1557	1.62
Liver	1060	375-394	1547-1585	1.64-1.68
Spleen	1060	380-389	1556-1575	1.65-1.67
Muscles	1070	353-393	1542-1626	1.65-1.74
Bone	1380-1810	25-100	2700-4100	3.75-7.4
Non Biological Materials:				
Air($0^{\circ}C$)	1.2	$8*10^{-6}$	330	0.0004
Rubber	950	438	1550	1.472
Fresh Water ($25^{\circ}C$)	988	452	1497	1.48
Salt Water	1025	416	1531	1.569
Polystyrene	1120	143	2500	2.8
Hard PVC	1350	175	2060	2.78
Araldit	1200	160	2300	2.8
Silicon RTV-11	1260	739	1000	1.26
Quartz	2650	11.4	5750	15.2
PZT-5A	7750	5.65	4350	33.71
Gold	19290	4.93	3240	62.5
Aluminum	2875	9	6260	18

The objectives of this Ph.D. study are:

1. To investigate ultrasonic wave propagation in multilayer structures and to explore attenuation based ultrasonic technique to evaluate defects in multilayer structures.
2. To establish a method for thin film acoustic property characterization.
3. To develop new nano-structure materials for high frequency ultrasonic transducer matching layers.
4. To study the effect of gradient acoustic impedance matching on transducer sensitivity, transmission efficiency and bandwidth.

Chapter 2

TRANSMISSION MATRIX TECHNIQUE

2.1 Wave Transmission and Reflection

When a plane wave meets an interface between different materials, the wave will be divided into two parts: transmitted and reflected waves. Suppose that the incident wave is given by:

$$u_I = Ae^{i(\omega t - k_1 x)} \qquad \text{(Eq 2-1)}$$

The transmitted wave and the reflected wave can be expressed as:

$$u_T = A_T e^{i(\omega t - k_2 x)} \qquad \text{(Eq 2-2)}$$

$$u_R = A_R e^{i(\omega t + k_1 x)} \qquad \text{(Eq 2-3)}$$

The combined wave in medium 1 and 2 respectively are:

$$u_1 = Ae^{i(\omega t - k_1 x)} + A_R e^{i(\omega t + k_1 x)} \qquad \text{(Eq 2-4)}$$

$$u_2 = A_T e^{i(\omega t - k_2 x)} \qquad \text{(Eq 2-5)}$$

By applying the continuity of pressure and normal particle velocity as boundary condition, can get:

$$A + A_R = A_T \qquad \text{(Eq 2-6)}$$

$$\rho_1 v_1 (1 - A_R) = \rho_2 v_2 A_T \qquad \text{(Eq 2-7)}$$

Solving these two equations gives:

$$A_T = \frac{2\rho_1 v_1}{\rho_1 v_1 + \rho_2 v_2} A \qquad \text{(Eq 2-8)}$$

$$A_R = \frac{\rho_1 v_1 - \rho_2 v_2}{\rho_1 v_1 + \rho_2 v_2} A \qquad \text{(Eq 2-9)}$$

And the stresses of the incident, transmitted and reflected waves are expressed as:

$$\delta_I = ik_1(\lambda_1 + 2K_1)e^{i(\omega t - k_1 x)} \qquad \text{(Eq 2-10)}$$

$$\delta_T = ik_1(\lambda_2 + 2K_2)e^{i(\omega t - k_2 x)} \qquad \text{(Eq 2-11)}$$

$$\delta_R = -ik_1(\lambda_2 + 2K_2)e^{-(\omega t - k_1 x)} \qquad \text{(Eq 2-12)}$$

Where λ is the wavelength and K denotes the longitudinal elastic stiffness coefficient. The transmission and reflection coefficients can be derived as:

$$T = \frac{(\lambda_2 + 2K_2)k_2}{(\lambda_1 + 2K_1)k_1} \frac{A_T}{A} = -\frac{2\rho_2 v_2}{\rho_1 v_1 + \rho_2 v_2} \qquad \text{(Eq 2-13)}$$

$$R = -\frac{A_R}{A} = \frac{\rho_2 v_2 - \rho_1 v_1}{\rho_1 v_1 + \rho_2 v_2} \qquad \text{(Eq 2-14)}$$

And the intensity coefficients are:

$$T_I = \frac{4\frac{\rho_2 v_2}{\rho_1 v_1}}{\left(\frac{\rho_2 v_2}{\rho_1 v_1} + 1\right)^2} \qquad \text{(Eq 2-15)}$$

$$R_I = \left(\frac{\frac{\rho_2 v_2}{\rho_1 v_1} - 1}{\frac{\rho_2 v_2}{\rho_1 v_1} + 1}\right)^2 \qquad \text{(Eq 2-16)}$$

2.2 Derivation of the T-Matrix

When ultrasonic wave travels through a structure with multiple sub-layers, refractions and reflections happen at every interface between different sub-layers due to acoustic impedance difference. The outgoing wave's amplitude is influenced by the acoustic properties of those sub-layer materials and the formation of the whole structure. Transfer matrix or the T-matrix technique can be used to analyze the ultrasound in such structures.

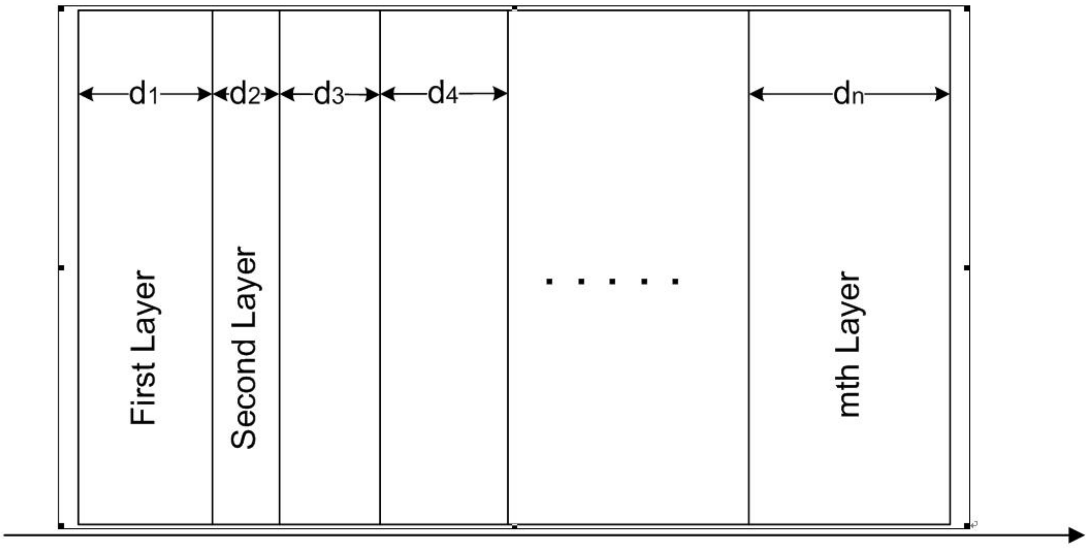

Fig. 2-1 : Illustration of the Multilayer Structure.

Consider a multilayer structure shown in Fig. 2-1. Suppose that there is a continuous longitudinal plane wave $y(x,t)$ entering the structure from the left at $x = 0$, the following wave functions can be obtained inside the first layer after the wave reaches steady state:

$$y_1 = A_1 e^{i(\omega t - k_1 x)} + B_1 e^{i(\omega t + k_1 x)} \qquad \text{(Eq 2-17)}$$

Similarly, inside the mth layer, we have:

$$y_m = A_m e^{i(\omega t + k_m x)} + B_m e^{i(\omega t - k_m x)} \qquad \text{(Eq 2-18)}$$

Where ω is the angular frequency, k_n is the wave number given by

$$k_n = \omega / v_n \qquad \text{(Eq 2-19)}$$

The subscript n indicates that the quantity is for the n[th] layer. The relationship among different coefficients in the n[th] cell can be calculated by applying the conditions of the continuity of pressure and normal particle velocity at the layer boundaries:

$$A_{n+1} + B_{n+1} = A_n e^{ik_n a} + B_n e^{-ik_n a} \qquad \text{(Eq 2-20)}$$

$$Z_{n+1}A_{n+1} - Z_{n+1}B_{n+1} = Z_n C_n e^{ik_n a} - Z_n D_n e^{-ik_n a} \qquad \text{(Eq 2-21)}$$

Where the acoustic impedance of the material in each layer is defined as the product of material density and sound velocity:

$$Z_n = \rho v_n \qquad \text{(Eq 2-22)}$$

Eq 2-20 and Eq 2-21 lead to:

$$\begin{pmatrix} A_n \\ B_n \end{pmatrix} = \frac{1}{2Z_n}\begin{pmatrix} (Z_n + Z_{n+1})e^{ik_n d_n} & (Z_n - Z_{n+1})e^{-ik_n d_n} \\ (Z_n - Z_{n+1})e^{ik_n d_n} & (Z_n + Z_{n+1})e^{-ik_n d_n} \end{pmatrix}\begin{pmatrix} A_{n+1} \\ B_{n+1} \end{pmatrix} = \left[T_{d_n}\right]\begin{pmatrix} A_{n+1} \\ B_{n+1} \end{pmatrix} \qquad \text{(Eq 2-23)}$$

Similarly, Wave transmission and reflection at the boundary between the (n+1)[th] and the (n+2)[th] layers can be acquired by applying the same boundary condition:

$$\begin{pmatrix} A_{n+1} \\ B_{n+1} \end{pmatrix} = \frac{1}{2Z_{n+1}}\begin{pmatrix} (Z_{n+1} + Z_{n+2})e^{ik_{n+1} d_{n+1}} & (Z_{n+1} - Z_{n+2})e^{-ik_{n+1} d_{n+1}} \\ (Z_{n+1} - Z_{n+2})e^{ik_{n+1} d_{n+1}} & (Z_{n+1} + Z_{n+2})e^{-ik_{n+1} d_{n+1}} \end{pmatrix}\begin{pmatrix} A_{n+2} \\ B_{n+2} \end{pmatrix} = \left[T_{d_{n+1}}\right]\begin{pmatrix} A_{n+2} \\ B_{n+2} \end{pmatrix} \qquad \text{(Eq 2-24)}$$

From Eq 2-23 and Eq 2-24**,** we can get the following recurrence condition:

$$\begin{pmatrix} A_n \\ B_n \end{pmatrix} = [T_{d_n}][T_{d_{n+1}}]\begin{pmatrix} A_{n+2} \\ B_{n+2} \end{pmatrix} \qquad \text{(Eq 2-25)}$$

Considering a multilayer structure with m different layers, the following relation is derived according to the recurrence equation from Eq 2-25:

$$\begin{pmatrix} A_1 \\ B_1 \end{pmatrix} = [T(m)] \begin{pmatrix} A_{m+1} \\ B_{m+1} \end{pmatrix} \qquad \text{(Eq 2-26)}$$

where

$$[T(m)] = [T_{d_1}][T_{d_2}]\cdots[T_{d_{m-1}}][T_{d_m}] \qquad \text{(Eq 2-27)}$$

There is only transmitted wave (no reflection wave) at the far right output side, hence, $B_{m+1} = 0$, so that:

$$\frac{A_{m+1}}{A_1} = \frac{1}{T(m)_{11}} \qquad \text{(Eq 2-28)}$$

By applying the T-Matrix technique, amplitude of the output wave can be quickly determined when incident wave properties and target structure information are provided.

2.3 Wave Propagation in Periodic Multi-layer Structures

One interesting special multilayer structure case is the periodic structure such as multilayer ceramic capacitors (MLCC) or multilayer ceramic actuators (MLCA) as shown in Fig. 2-2. This structure consists of multiple identical unit cells. Each cell has one electrode layer and one ceramic layer. This system can be treated by one-dimensional T-Matrix technique. In Fig. 2-2, a and b are the thickness of the electrode and ceramic layers, respectively, and $d = a + b$, is the periodicity of the unit cell.

Assume that the sound speeds in the electrode layer and ceramic layer materials are, respectively, 2690m/s and 3400m/s. The densities of those two materials are $10490\ \mathrm{kg/m^3}$ and $6020\ \mathrm{kg/m^3}$. The electrode layers and the ceramic layers are respectively, 10 microns and 40 microns thick.

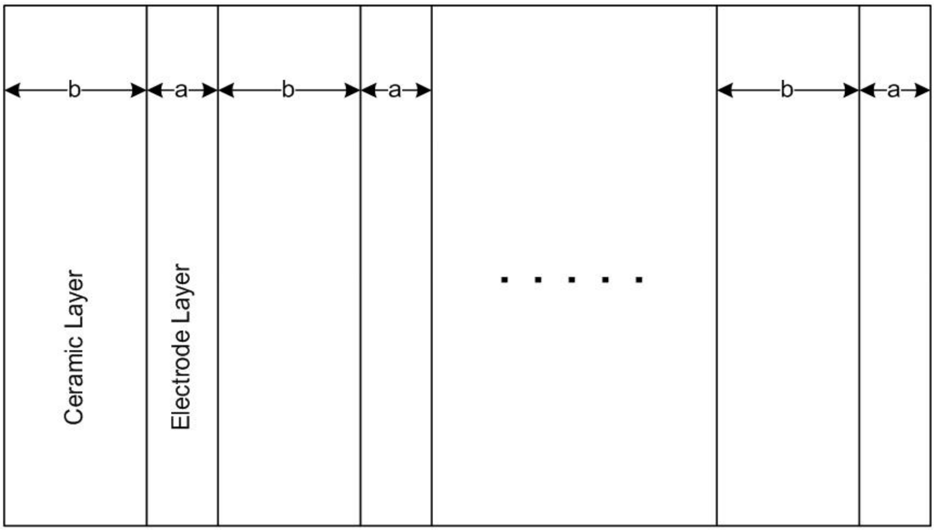

Fig. **2-2**: Periodic Multilayer Structure of MLCC

We consider several scenarios with different cell unit numbers (1, 5, 10, 50) and calculated the transmission coefficient of the total structure. The results are shown in Fig. **2-3** to Fig. **2-6**. It is quite interesting to see that some band structures begin to appear even when there are only a few cell units. Due to structural resonance, complete ultrasound transmission can happen at certain frequencies. At some other frequencies, we will get nearly complete reflection. As the unit cell number increases, passbands and stopbands will start to form as shown in the case of 50 cell structure in Fig. **2-6**.

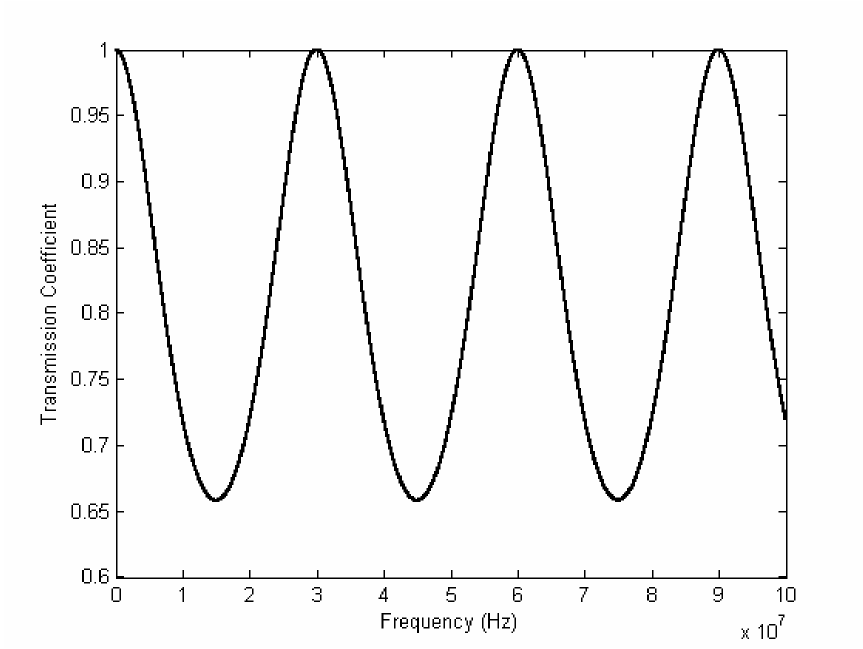

Fig. 2-3: Transmission coefficient versus frequency (1 cell)

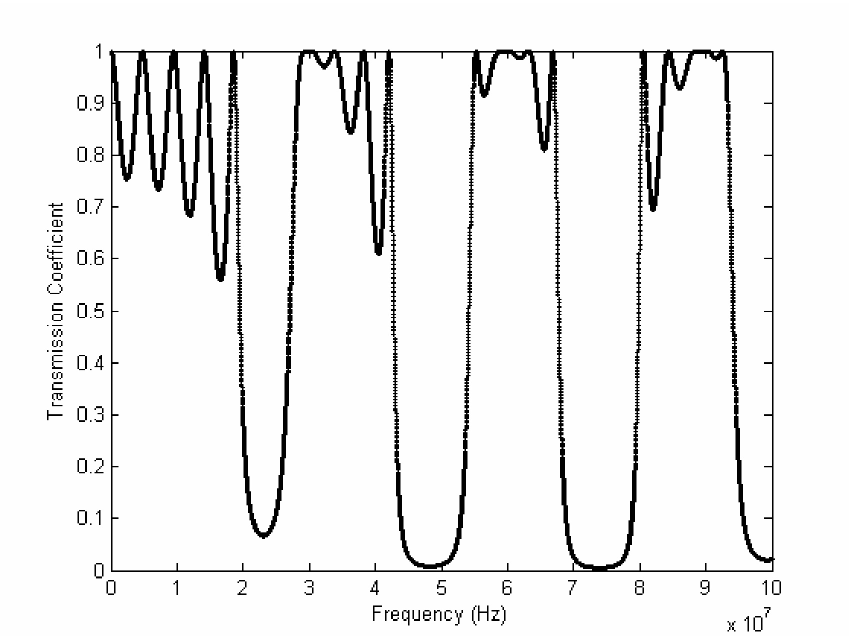

Fig. 2-4: Transmission coefficient versus frequency (5 cells)

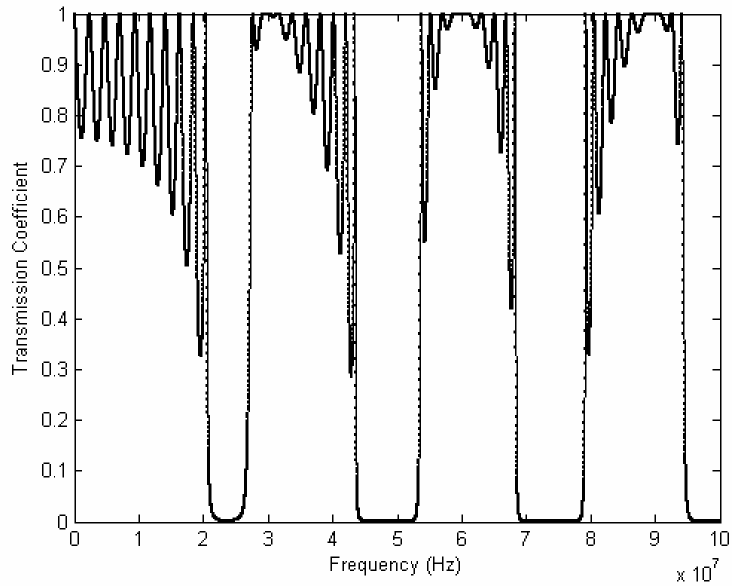

Fig. **2-5**: Transmission coefficient versus frequency (10 cells)

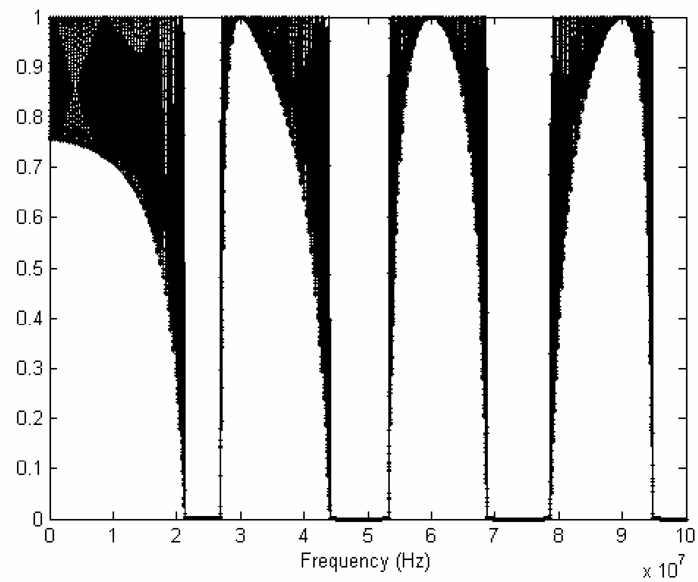

Fig. **2-6**: Transmission coefficient versus frequency (50 cells)

2.4 Ultrasonic NDE for Multilayer Structures Containing Multiple Delaminations.

2.4.1 Introduction

In multilayer ceramic capacitor (MLCC) and multilayer ceramic actuators (MLCA) structures, delaminations as shown in Fig. 2-7 break the attachment between the electrode and ceramic layers.

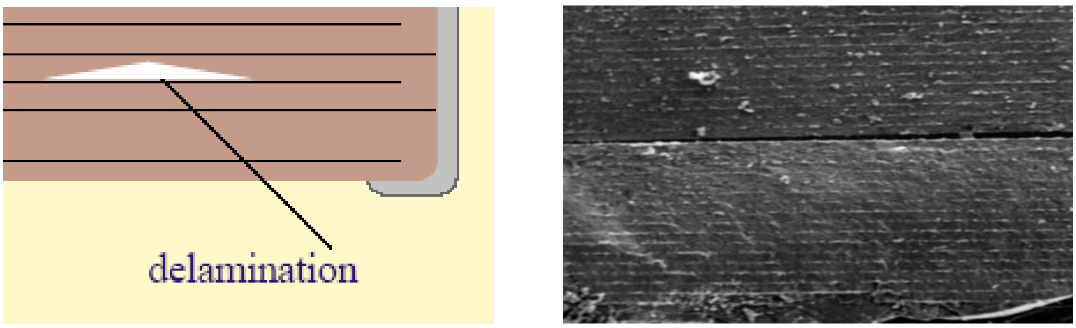

Fig. 2-7: Schematic and actual photo of Delamination in MLCC

We conducted theoretical analysis to correlate the velocity, amplitude and attenuation of ultrasonic waves to the delamination situation in a multilayer structure containing multiple delaminations [Zhu, Cao 2007]. Conventional ultrasonic imaging technology as presented in Fig. 2-8 uses the time delay of reflected pulses from delaminations to form the image of defects. This strategy only provides limited resolution because the reflection of ultrasonic waves only occurs when the defect size is comparable to or greater than the ultrasound wavelength. If the defect size is much smaller than the wavelength, there will be no reflected plane waves but only scattered waves.

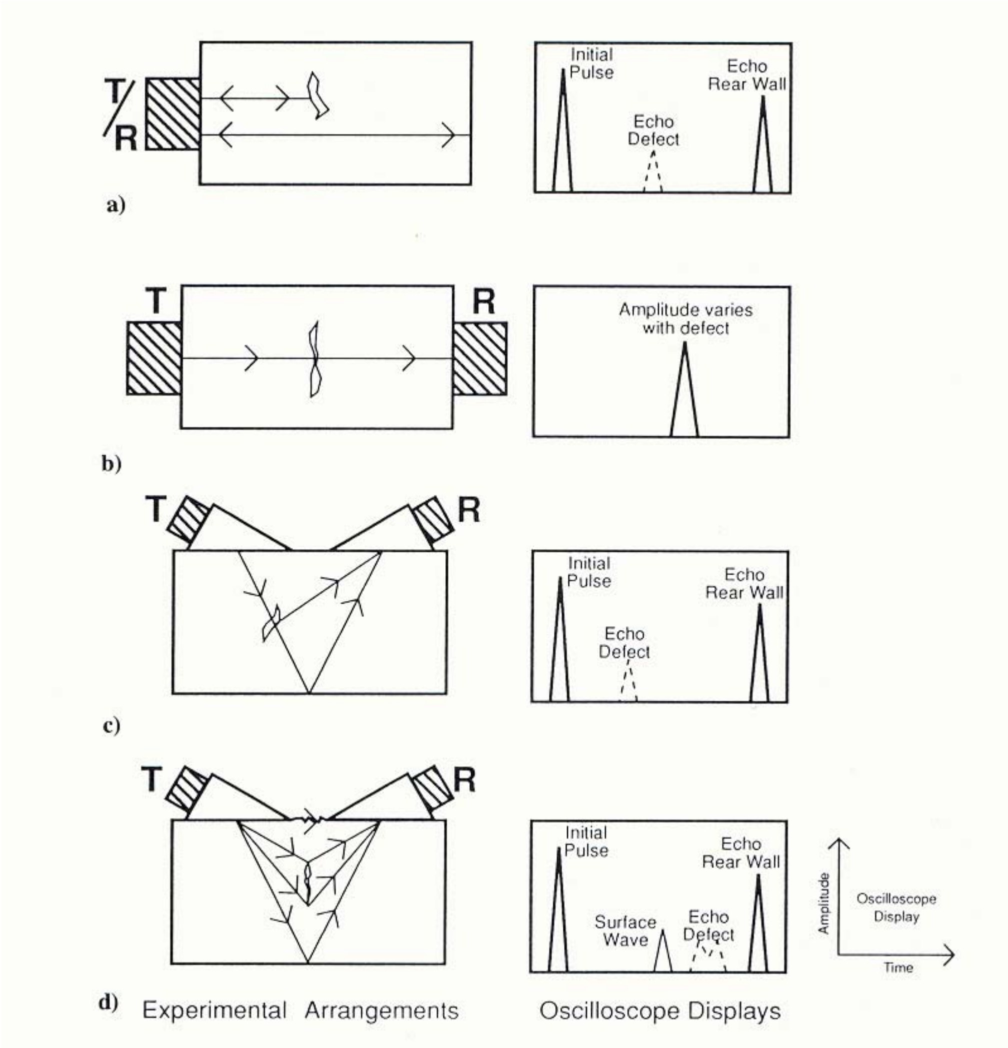

Fig. 2-8: Conventional ultrasonic imaging technology uses the time delay of reflected pulses from delaminations to form an image of defects.

The ultrasonic attenuation, on the other hand, is very sensitive to such small defects because of scattering effects. The amplitude change for waves going through the target structure carries a lot of information and it is known that the ultrasonic attenuation can detect microscopic defects that are only fractions of a wavelength. Therefore, we could get more information about the delaminations in multilayer structures under inspection if both the velocity and attenuation data were used

Our method of treating multiplayer structures is mainly based on the transmission matrix technique, while the approach described in [Foldy 1945] [Sotiropoulos, Achenbach 1988] [Zhang, Achenbach 1991] is applied to deal with the scattering problem. Because the delaminations are at the interfaces of the electrode and ceramic layers, they are generally oriented parallel to each other along the interface planes. For simplicity, all the delaminations are assumed to be penny-shaped and have the exactly same size.

2.4.2 Wave Scattering

When the incidence wave encounters a delamination, a small fraction of the wave may transmit through it if the delamination only opens a very thin gap, but the main portion of the wave is scattered or reflected. The theoretical work presented in this thesis is based on the model proposed by Leslie L. Foldy [Foldy 1945] for multiple scattering together with the approaches developed in [Sotiropoulos, Achenbach 1988] and [Zhang, Achenbach 1991]. The crack-opening displacement of the reference delamination is divided into two parts: one for single delamination and the other for induced component due to the presence of other delaminations. Following this idea, the average forward scattering amplitude for the incident longitudinal wave can be divided into two parts. The first part is for a single delamination, the boundary condition on the surface of the delamination is given by:

$$\sigma^{in}(x)+\sigma^{tm}(x)+\sigma^{sc}(x)=0, \quad x \in A^{\pm} \qquad \text{(Eq 2-29)}$$

where σ^{in} is the stress component of the incidence wave, σ^{tm} is the stress component of the transmitted wave and σ^{sc} is the stress component of the scattered wave from the delamination. $A^{\pm}$ denote the surface area of the delamination (positive and negative side). The scattered wave displacement is given by

$$u_k^{sc}(x)=\int_{A^+}\sigma_{ijk}^{G}(x;y)\Delta u_i(y)n_j dS(y) \qquad \text{(Eq 2-30)}$$

where $\sigma_{ijk}^{G}(x;y)$ is the Green's function for stress, which denotes stress components at position x due to a time-harmonic, unit point force at position y in the direction of y_k, Δu_i is the crack-opening displacement, and n_j is the unit normal of the surface A^+.

From Eq 2-30 we get:

$$\sigma_{3q}^{in}(x)+\sigma_{3q}^{tm}(x)=-c_{3qkl}\frac{d}{dx_l}\int_{A+}\sigma_{ijk}^{G}(x;y)\Delta u_i(y)n_j dS(y) \qquad x \in A^{\pm} \qquad \text{(Eq 2-31)}$$

Here c_{3qkl} is the elastic constant tensor component. Eq 2-31 can be solved numerically using the method given in [Roy 1987]. Finally, the combined crack-opening displacement is given by:

$$\Delta u_i(x) = \sum_{m=0}^{3} \frac{(ik_T)^m}{m!} \Delta u_i^{(m)}(x) + O(k_T r)^4 \qquad \text{(Eq 2-32)}$$

r is the radius of the delamination. The incident wave amplitude is normalized to 1 so that the final forward scattered wave amplitude can be written as:

$$\begin{aligned} F &= \frac{k_L^2 r^3 (Z_m - Z_{air})}{3\pi k (Z_m + Z_{air})} * \\ &\{\frac{1}{\kappa(1-\kappa^2)}(g_1^0 - \frac{(k_L r)^2}{10\kappa^2}(g_1^2 + g_1^3 + g_1^4) - \frac{i(k_L r)^3}{6\kappa^3} g_1^5 + O(k_T r)^4)\} \end{aligned} \qquad \text{(Eq 2-33)}$$

In Eq 2-33:

$$\kappa = k_L / k_T \qquad \text{(Eq 2-34)}$$

$$\begin{aligned} g_1^0 &= 1 \\ g_1^2 &= -\frac{1}{9}[\frac{6(1-\kappa^2)^2 + 4\kappa^2}{(1-\kappa^2)}] \\ g_1^3 = g_1^4 &= -\frac{1}{9}[\frac{3(1-\kappa^2)^2 + 2\kappa^2}{2(1-\kappa^2)}] \\ g_1^5 &= -\frac{2}{3\pi}[\frac{32\kappa^5 - 40\kappa^3 + 15\kappa + 8}{5(1-\kappa^2)}] \end{aligned} \qquad \text{(Eq 2-35)}$$

The second part of influence to be put into consideration is the interaction of randomly distributed delaminations. If the total number of delaminations is n, the scattering displacement is given by [Zhang, Achenbach 1991]:

$$u_k^{sc}(x) = \sum_{p=1}^{n} \int_{A_p^+} \sigma_{ijk}^G (x;y) \Delta u_i^p (y) n_j dS(y), \qquad x \in \sum_{p=1}^{n} A_p^+ \qquad \text{(Eq 2-36)}$$

A_p^+ and Δu_i^p indicate insonified area and the crack-opening displacement of the p^{th} delamination, then:

$$\sigma_{3q}^{in}(x)+\sigma_{3q}^{tm}(x)=-\sum_{p=1}^{n}C_{3tkl}\frac{d}{dx_l}*\int_{A_p^+}\sigma_{ijk}^{G}(x;y)\Delta u_i^p(y)n_j dS(y) \qquad x\in\sum_{p=1}^{n}A_p^+ \qquad \text{(Eq 2-37)}$$

From the approach in [Sotiropoulos, Achenbach 1988], the continuously distributed dipoles of the p^{th} delamination are replaced by an approximation to their resultants at the geometrical center of the p^{th} delamination using the Green's function of stress. Assuming the influences of all other delaminations are the same, if we do not consider the multilayer effect at this point on those influences, the average forward scattering amplitude caused by the interaction from other random distributed delaminations would be given by:

$$<F^*>=-\frac{i(Z_m-Z_{air})(k_L r)^2}{3\pi(Z_m+Z_{air})}*$$
$$[\frac{1}{1-\kappa^2}\{\overset{-0}{g_1}-\frac{(k_L r)^2}{10\kappa^2}(5\overset{-2}{g_1}+\overset{-3}{g_1}+\overset{-4}{g_1})-\qquad \text{(Eq 2-38)}$$
$$\frac{i(k_L r)^3}{6\kappa^3}\overset{-5}{g_1}+O[(k_L r)^4]\}<\sigma_{33}^{u}>]nA_{tu}^{-1}V_t^0$$

In Eq 2-38:

$$\bar{g}_1^0 = 1$$
$$\bar{g}_1^2 = -\frac{1}{9}[\frac{6(1-\kappa^2)^2 + 4\kappa^2}{(1-\kappa^2)}]$$
$$\bar{g}_1^3 = \bar{g}_1^4 = -\frac{1}{9}[\frac{3(1-\kappa^2)^2 + 2\kappa^2}{2(1-\kappa^2)}] \qquad \text{(Eq 2-39)}$$
$$\bar{g}_1^5 = \frac{32\kappa^5 - 40\kappa^3 + 15\kappa + 8}{5(1-\kappa^2)}$$

2.4.3 Wave Attenuation and Velocity

When an ultrasonic wave transmits through a multilayer structure containing multiple delaminations, it attenuates due to both the reflection caused by the layer boundaries and the reflection, scattering caused by the delaminations. We used the T-matrix technique described in the previous section to treat the multi-layer effects. The attenuation coefficient for such a periodic structure is given in Eq 2-28. For the wave propagating and scattering through multiple delaminations, we can use the Foldy's theory [Foldy 1945] to simplify the problem, i.e., *the average of the square of wave function at any point is equal to the square of the average wave function at the point plus contributions representing scattering from all other portions of the medium*. These contributions are proportional to the average of the squares of the wave function and the scattering cross section per unit volume at each point. Therefore, after going through these delaminations, the effective wave number relation of the ultrasonic wave can be written as:

$$(k_L^{'}r)^2 = (k_L r)^2 + (4\pi E - o(4\pi E))(\frac{F + F^* + F^T}{r}) \qquad \text{(Eq 2-40)}$$

Where $k_L^{'}$ is the wave number for structures with delaminations, k_L is the wave number for system without delaminations, $o(\,)$ denotes overlapping scattering cross section percentage, F^T is the amplitude of wave transmitted through delaminations, which is given by:

$$F^T = \frac{4Z_{air}Z_m}{(Z_c + Z_{air})(Z_e + Z_{air})} \qquad \text{(Eq 2-41)}$$

The parameter E is the delamination density. By solving Eq **2-41**, we can get the effective phase velocity and attenuation coefficient of the wave due to the presence of delaminations:

$$\mathrm{Re}(\frac{k_L^{'}r}{k_L r}) = \frac{V_L}{V_L^{'}} \qquad \text{(Eq 2-42)}$$

$$\mathrm{Im}(k_L^{'}r) = \frac{r}{2}\alpha' \qquad \text{(Eq 2-43)}$$

In these two equations, V_L is the longitudinal wave velocity without delaminations, $V_L^{'}$ is the longitudinal wave velocity with the presence of delaminations, α' is the attenuation coefficient of the transmission wave due to the scattering of delaminations. Assuming the η^{th} cell is where the first delamination locates, by combining with the T-matrix results in previous sections, we can get the total attenuation coefficient of wave transmitted through multilayer capacitor with multiple delaminations and also the phase relationship between the incident wave and the transmitted wave.

$$\alpha = 1 - \frac{e^{ik_e Nd}}{[T1(\eta) * (1-\alpha') * T2(N-\eta)]_{11}} \qquad \text{(Eq 2-44)}$$

2.4.4 Numerical Results and Discussions.

Calculations based on the theoretical work above are executed for several selected scenarios. We consider the multiplayer structure consist of Ag electrode layer and $BaTiO_3$ dielectric layer. The acoustic impedance of each material is: $Z_{air} = 0.0004 MRayl$, $Z_c = 24 MRayl$, $Z_e = 38 MRayl$. The Poisson's ratios of the Ag and ceramic both are set as 0.33 and the delaminations are assumed uniformly distributed. To demonstrate the concept, first calculation was conducted on the structure with 5 electrode layers and 4 ceramics layers. The thickness of electrode and ceramic layers are 2μm and 10μm, respectively. The capacitor volume is normalized to one for the convenience of calculations.

Fig. 2-9 shows the ratio of the effective phase velocity over the incidence wave velocity against the delamination density parameter at different frequencies. The $E = 0$ condition implies no delaminations in the multilayer structure; hence, no wave velocity change takes place in this case. When the number of delaminations or the size of delaminations increases, the effective wave velocity decreases. The reduction of phase velocity is nonlinear and the effect is stronger for higher frequencies.

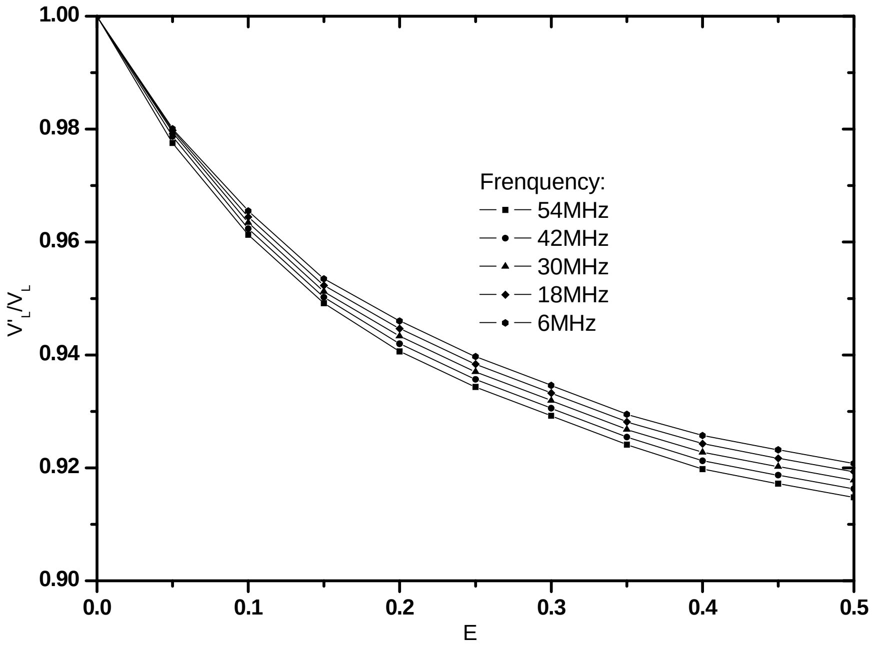

Fig. **2-9**: Normalized wave velocity vs delamination density at different frequencies.

As expected, the attenuation coefficient increases with the delamination density as shown in Fig. **2-10**. It is interesting to see a jump of the attenuation coefficient at higher frequencies. This jump is due to the resonance nature of the periodic structure as shown in Fig. **2-11**. An ultrasonic wave can only pass through at certain frequencies even without other attenuation sources in a periodic structure while it is strongly attenuated at other frequencies. At low frequencies, the delamination density does not show strong influence to the attenuation. Based on Fig. **2-11**, one may conclude that if the attenuation is used for the NDE purpose, the frequency of the incidence wave should be greater then 45 MHz, beyond which the curves for different delamination densities split.

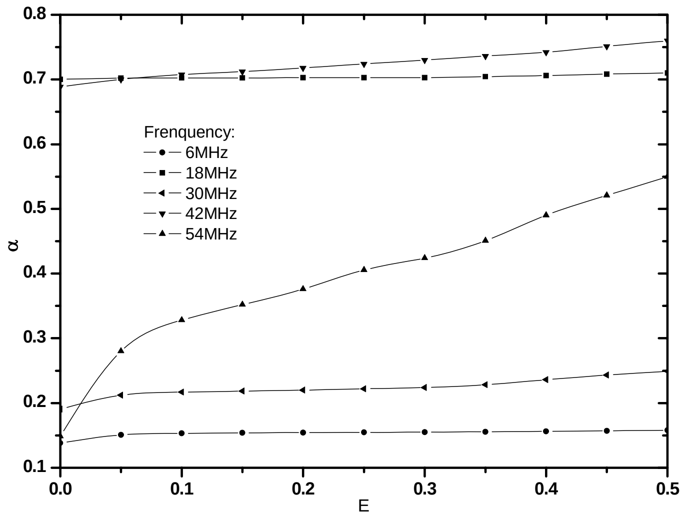

Fig. **2-10**: Attenuation coefficient vs delamination density at different frequencies.

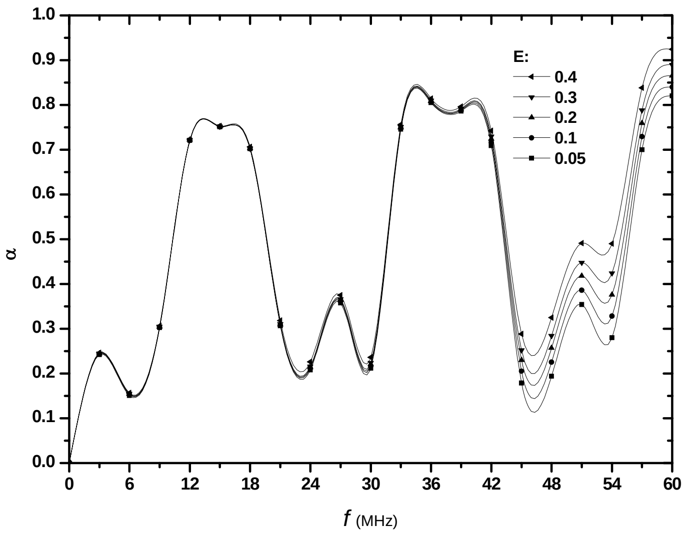

Fig. **2-11**: Attenuation coefficient vs incidence wave frequency for different delamination densities.

Fig. 2-12 and Fig. 2-13 show the influence of the total cross section of delaminations to the frequency dependence of the phase velocity and attenuation coefficient, respectively. The cross section variation represents the situation of delamination overlapping in different layers. When some of the delaminations in different layers block one another along the wave pathway, the effective total cross section is reduced, so that the attenuation is decreased. On the other hand, part of the wave that can transmit through one delamination is further attenuated due to the scattering of two or more delaminations, which causes the attenuation for the transmitted portion of the wave to increase.

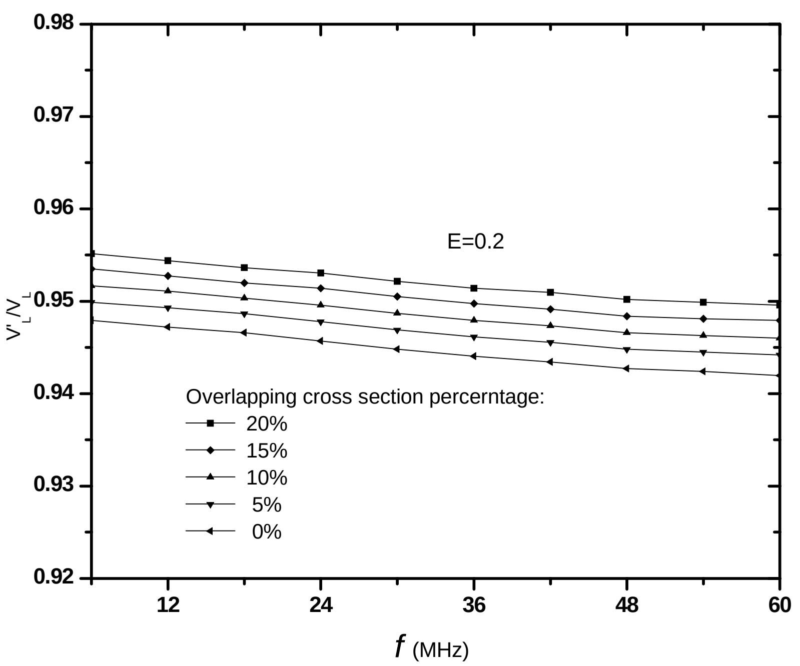

Fig. 2-12: Normalized wave velocity vs incidence wave frequency for different delamination overlapping percentage.

Overall, due to the very large acoustic impedance mismatch between air (inside the delamination gap) and the ceramic or the electrode, the waves transmit through the first delamination is already very weak, therefore, the net effect of delamination overlapping is to reduce the total effective attenuation coefficient caused by the reduction of scattering cross section per unit volume. In other words, for the same number of delaminations, if overlapping occurs, the effective wave velocity increases while the attenuation decreases.

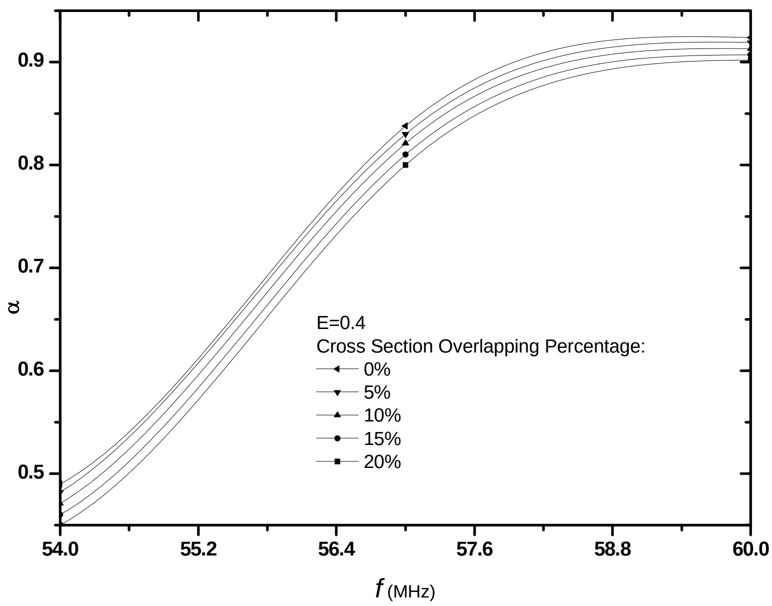

Fig. 2-13: Attenuation coefficient vs incidence wave frequency for different delamination overlapping percentage.

In addition to study the case of 5 electrode layers and 4 ceramics layers (total 9 layers), we have also calculated the case of 7 electrode layers and 6 ceramics layers (total 13 layers) and the results are compared in Fig. 2-14. As expected, the effective attenuation coefficient increases when the number of layers increases. It is important to note the frequency effect due to the periodic nature of the multilayer structure.

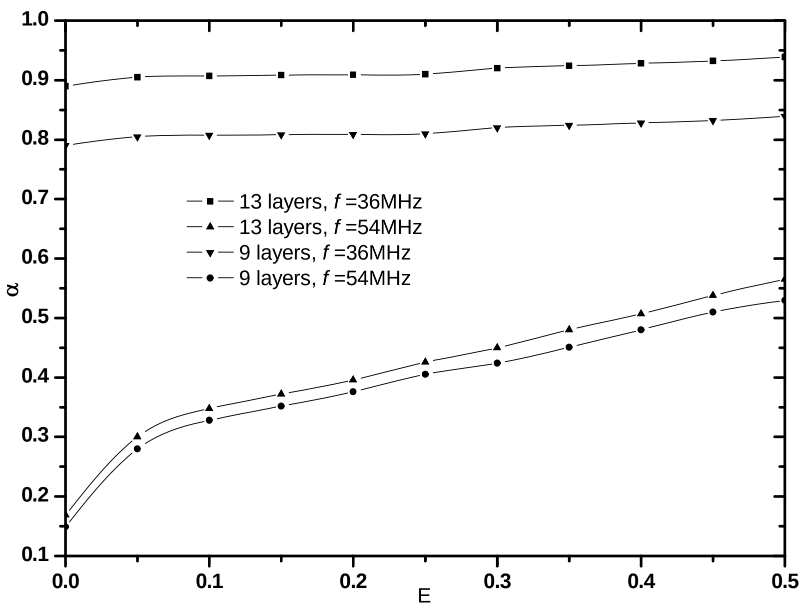

Fig. 2-14: Attenuation coefficient vs delamination density for two different scenarios of layers and two incidence frequencies.

2.4.5 Theoretical Results Analysis

As expected, the attenuation coefficient increases with the density of delaminations. At the same time, the effective phase velocity of the ultrasonic wave is reduced. The periodic nature of the multilayer structure has strong influence on the attenuation coefficient due to the multiple reflections at the ceramic-electrode interfaces. We have treated the multilayer reflection/transmission at the interfaces using the T-matrix technique. Strong frequency dependence occurs for the attenuation coefficient due to the periodic nature and the acoustic impedance mismatch between the electrode and the ceramics. For waves going through the delaminations, we have mainly studied the scattering phenomena to account for the effect of multiple small size delaminations. The combined effect of interface reflection and multiple delamination scattering has been calculated for several scenarios. It is shown that the changes of velocities and attenuation coefficient depend on several factors, i.e., the number of layers in the capacitor, the type of material in each layer, the delamination density, the incidence wave frequency and the degree of delamination overlapping in different layers. Such quantified information is very useful for the future development of attenuation based ultrasonic NDE technique, which can be used to detect small size delaminations that are beyond the resolution of conventional ultrasonic imaging. In the layer dimensions studied here, the incidence wave frequency must be greater than 45 MHz in order to detect the delamination density changes since there is no obvious difference in terms of velocity and attenuation coefficient for waves of lower frequencies.

Chapter 3

QUARTER WAVELENGTH MATCHING LAYER DESIGN

3.1 Matching Layer for Ultrasonic Transducers

3.1.1 Construction of Ultrasound Transducers

As mentioned in the first chapter, transducer is the most important component in medical ultrasonography system, which is the limiting factor for the resolution because other components, such as electronics and signal processing are well developed. An ultrasonic transducer has three major parts as shown in Fig. 3-1: piezoelectric resonator, backing and front matching layer(s).

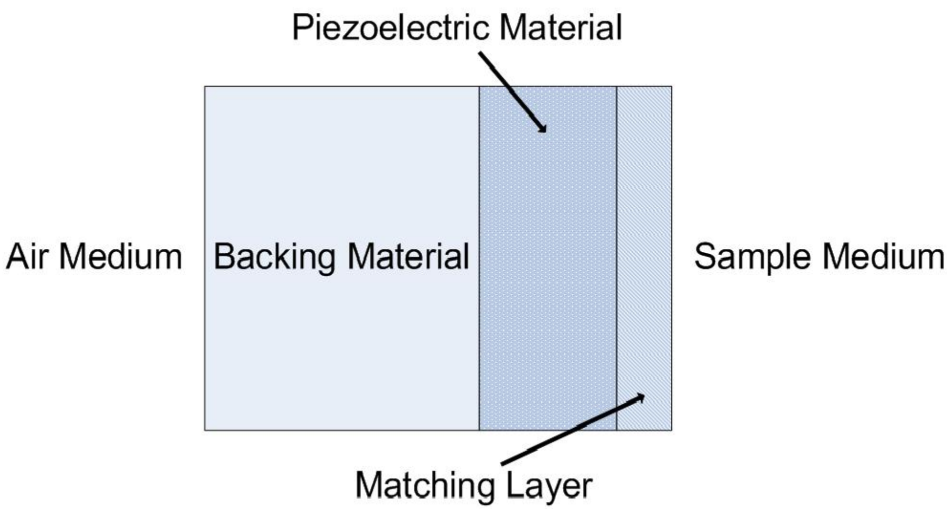

Fig. 3-1: Schematic of single element transducer.

The performance of ultrasonic transducers is decided by many factors, such as material properties of each component, external mechanical and electrical load conditions, mechanical and electrical structure designs, including radiation surface area, mechanical damping, housing, connector, etc. The main component for generating sound wave and receiving incoming signal is the piezoelectric resonator. In the transmission mode, it converts ac electric signal into a sinusoidal mechanical wave, while in receiving mode, it will generate voltage across it when acted upon by a mechanical pressure.

In medical ultrasonic imaging area, the widely used piezoelectric transducer material is lead zirconate titanate ceramic (PZT). Based on the specific requirements, such as the sensitivity or ability to cope with large acoustic power, properties of the PZT can be tuned by adding different dopants. In recent years, researchers have found a new series of piezoelectric material, lead magnesium niobate- lead titanate (PMN-PT) single crystals [Brown, et al. 1997] [Ritter, et al. 2000]. When the crystals are being poled along the [001] direction, its piezoelectric coefficient can be larger than 2000 pC/N and its electromechanical coupling coefficient better than 90%. Under the same working condition, these new piezoelectric materials can generate much stronger electrical signals to provide better sensitivity, penetration depth, axial resolution and much broader transducer bandwidth. There are also other types of engineered piezoelectric materials, like composite PZT, which can produce higher electromechanical coupling coefficient. The piezocomposites are made by dicing the piezoelectric then fill the kerfs by inert polymer materials. Because the acoustic impedance of piezocomposite is lower than that of PZT ceramic, it is easier for acoustic impedance matching.

After choosing proper piezoelectric material, electrodes will be deposited onto both sides of the thin piezoelectric plate. The thickness of the transducer plate is usually half-wavelength, there are also designs using quarter wavelength resonator for special applications. For a broadband transducer, the thickness is designed based on the center frequency of the transducer.

Ringdown is a big problem for a broadband transducer, it often happens after the piezoelectric material is excited by an electric pulse [De Ana, O'Donnell 2002]. When there is large acoustic impedance difference between piezoelectric and probing medium, a major fraction of the generated wave will be reflected back and forth in the piezoelectric material between the boundaries to cause the repeated output [Grewe 1989]. Duration of ringdown increases with time and causes the pulses to be too long which leads to the decline of the axial resolution [Zipparo 1996; Gururaja 1994; Grewe 1989]. Adding a backing layer can partially solve the ringdown problem. The backing is usually made of a material with acoustic impedance close to the piezoelectric resonator and having very high damping coefficient. Because the acoustic impedance of backing layer material is similar to that of the piezoelectric material, most of the backward transmitted wave quickly attenuates and become heat, only very little portion may bounce back [Kinsler 1982] so that the ringdown will be greatly reduced. However, this method doesn’t come without a price: large portion of the electrical energy is wasted and converted to thermal energy. The total energy transmitted into tissue sample will decrease so that the sensitivity will be reduced and the transducer insertion loss will be increased [Cannata, Ritter, et al. 2003]. There are also some other special techniques to solve the ringdown problem, including using multiple wavelength thick ceramics and fabricating ceramics with complicated shapes. But these methods all suffer from the same shortcoming of very low sensitivity, therefore, these method are only used in some special cases.

Commonly used backing layer materials include tungsten-loaded epoxy, pyrolytic, brass and carbon etc [Brown 2000]. Although they still play the role of damping the backward waves, today's transducer industry use proper front matching layer to solve the ringdown problem. Proper matching layer can increase the energy transmitting efficiency from the front end so that less energy will be reflected. If the matching layer is optimized, backing layer may not be needed. In fact, there are air backing designs

Transducers are designed to perform different tasks. Some are fabricated to have larger penetration depth while others are built to be especially for better resolution. A transducer that performs well in one application may not provide acceptable results under a different situation. The most important properties of ultrasonic transducer are frequency and bandwidth. Normally the frequency marked on a transducer is the central active frequency. Transducers with lower frequencies provide greater penetration depth, while the ones with high frequency provide less penetration but better resolution to smaller scale tissues. High frequency transducer can dramatically improve the resolution and measurement capability when configured properly with other components. Broader frequency band could provide transducer with higher resolving power under pulse-echo operation [Hoskins, et al. 2003]. Fig. 3-2 shows transmission function spectrum of a lithium niobate transducer without matching layer. The center frequency is set at 104.29MHz and 6dB two-way bandwidth is found to be 29.26%. Obviously this bandwidth is low for medical applications. Narrower bandwidth will erase the resolution gain from increasing operating frequency.

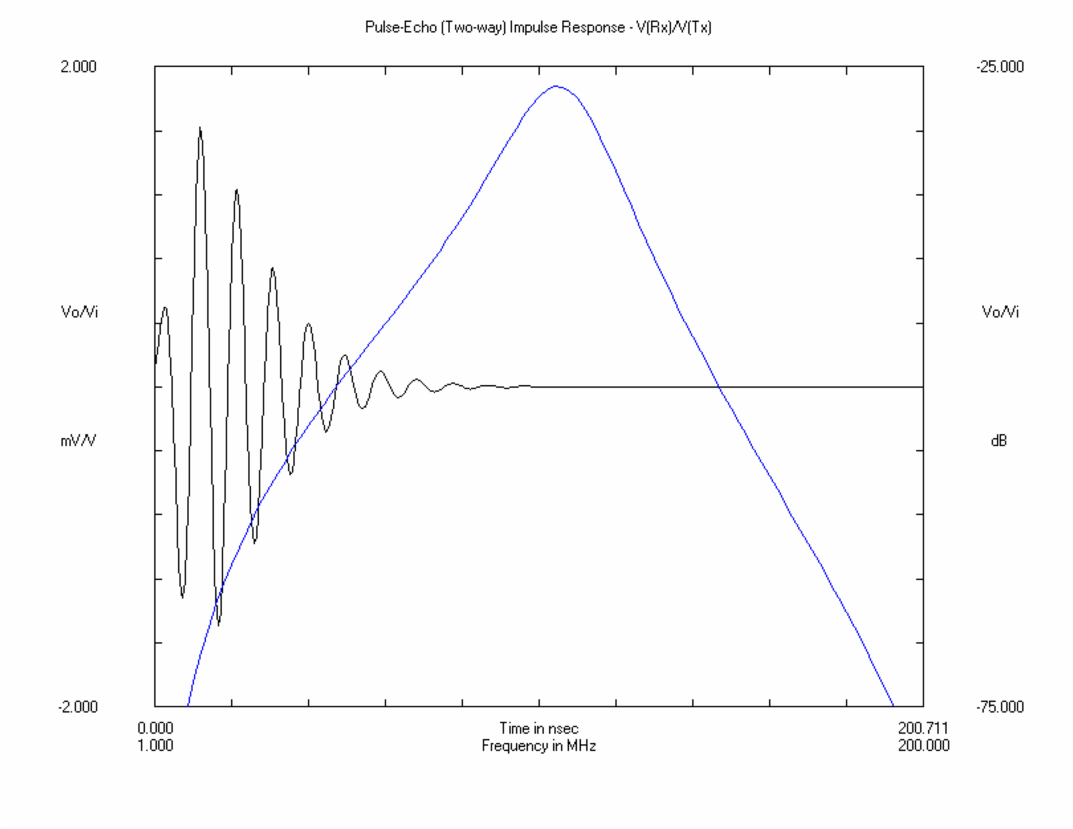

Fig. 3-2: Frequency spectrum of lithium niobate ultrasonic transducer without matching layer.

3.1.2 Principle of Quarter Wavelength Matching Layer

Matching layer is employed between the target medium and the front face of piezoelectric material in order to improve the ultrasonic wave transmission from piezoelectric section into the target medium. In matching layer design theory, the best acoustic impedance matching scenario can be achieved when the thickness of matching layer is quarter wavelength of the transducer central operating frequency. As shown in Fig. 3-3, sound wave reflects back and forth repeatedly within the matching layer, producing a series of overlapping waves that are in phase with each other, hence joining together to provide a larger resultant wave. At the same time, another series of waves also transmit back into the piezoelectric material layer and nicely cancel out the originally reflected incident wave at the piezoelectric material layer - matching layer interface [Hoskins, et al. 2003].

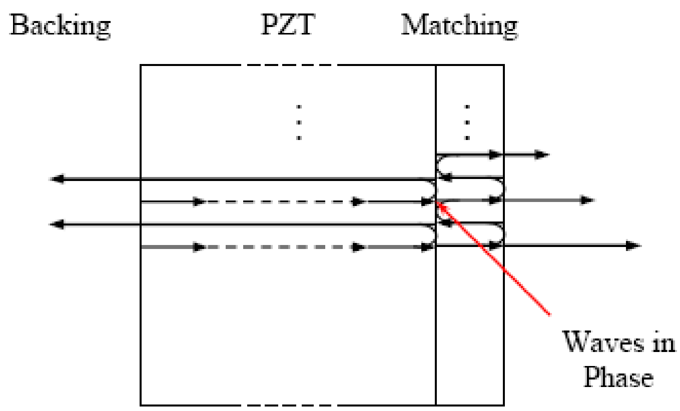

Fig. 3-3: Reverberation waves in matching layer.

The effect of adding matching layer is very clear from the figure above. The stepwise deduction of acoustic impedance by putting matching layer in between the piezoelectric and probing mediums greatly cuts the energy loss in the transmission of original signals and increases the amplitude of the received returning signals. Fig. 3-4 shows the transmission function spectrum of the same transducer in Fig. 3-2 after one layer of parylene is attached. The transmitted signal strength is almost three times larger than the no-matching layer case. The 6dB two-way bandwidth also improves to 35.53%.

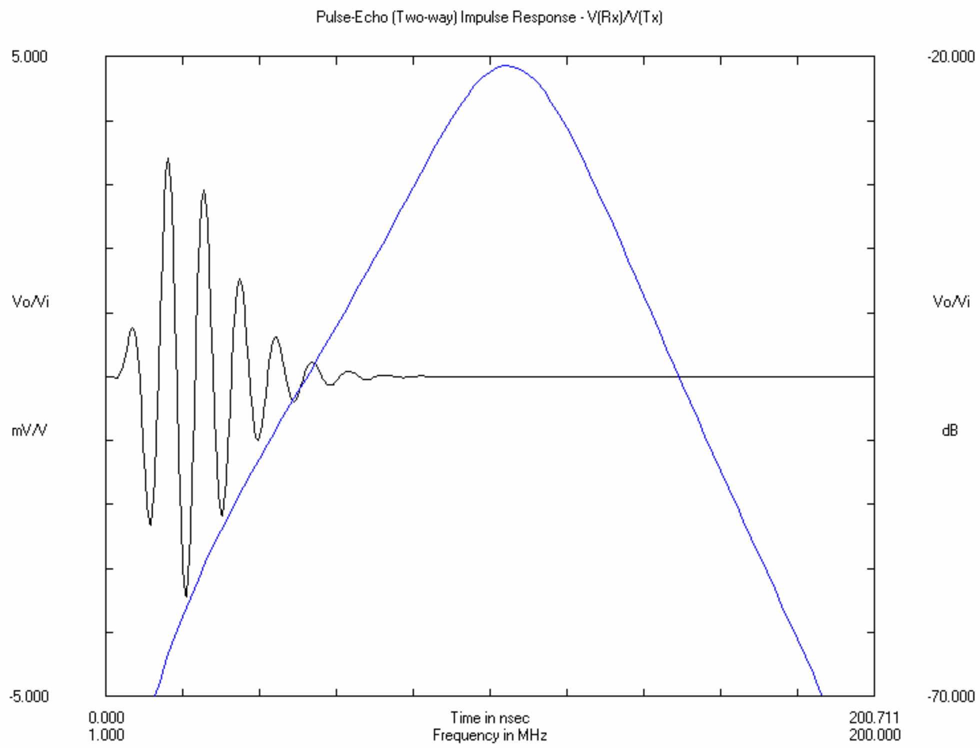

Fig. 3-4: Spectrum of lithium niobate ultrasonic transducer with single layer parylene.

3.2 Determine the Best Acoustic Impedance for Matching Layer Material

3.2.1 Geometric Mean

A quarter-wavelength matching layer made of material with appropriate acoustic impedance can further improve the system sensitivity. In order to better analyze the function of acoustic impedance in matching layer design, Transmission matrix technique and monochromatic approximation [Stumpf 1980] have been used in studying a structure as shown in Fig. 3-5.

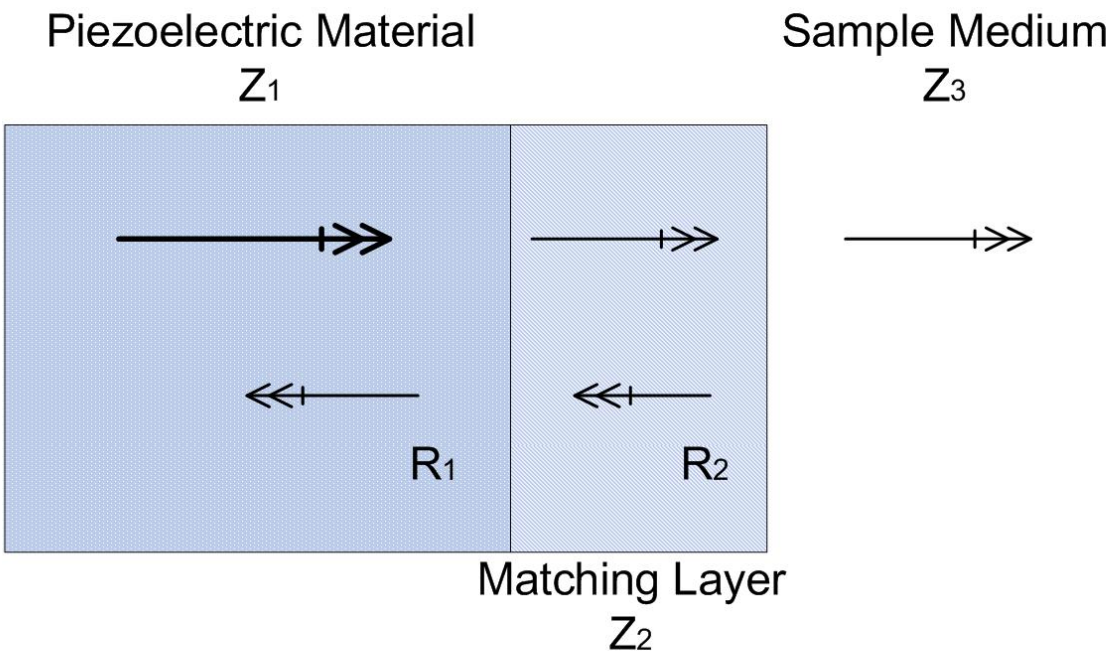

Fig. 3-5: Schematic of wave transmission in quarter wavelength matching layer.

The acoustic impedance for a plane wave is defined as:

$$Z = \rho \cdot v \qquad \text{(Eq 3-1)}$$

Where ρ is the material density and v is the sound speed. The sample medium is assumed to extend infinitely so that no reflection wave is produced. From [Draheim 1997], the reflection coefficient R_1 is:

$$R_1 = \frac{Z_3\cos(k_2\cdot L)+j\cdot Z_2\sin(k_2\cdot L)-Z_1\cos(k_2\cdot L)-j\dfrac{Z_1\cdot Z_3}{Z_2}\sin(k_2\cdot L)}{Z_3\cos(k_2\cdot L)+j\cdot Z_2\sin(k_2\cdot L)+Z_1\cos(k_2\cdot L)+j\dfrac{Z_1\cdot Z_3}{Z_2}\sin(k_2\cdot L)} \quad \text{(Eq 3-2)}$$

Z_1, Z_2 and Z_3 are respectively acoustic impedances of piezoelectric, matching and sample materials. k_1, k_2 and k_3 denote the wave numbers in those materials. R_1, R_2 are reflection coefficients at the two boundaries, while L is the thickness of matching layer. Using the definition of sound intensity, the intensity reflection coefficient is derived as:

$$\alpha_R = \frac{(1-Z_{13})^2\cos^2(k_2\cdot L)+(Z_{23}-Z_{12})^2\sin^2(k_2\cdot L)}{(1+Z_{13})^2\cos^2(k_2\cdot L)+(Z_{23}+Z_{12})^2\sin^2(k_2\cdot L)} \quad \text{(Eq 3-3)}$$

Where $Z_{ij} = \frac{Z_i}{Z_j}$. Based on the fact that energy transmitted is the total energy minus energy reflected, we can get the transmission coefficient:

$$\alpha_T = \frac{4Z_{13}}{(1+Z_{13})^2\cos^2(k_2\cdot L)+(Z_{23}+Z_{12})^2\sin^2(k_2\cdot L)} \quad \text{(Eq 3-4)}$$

When $L = (2n-1)\frac{\lambda}{4}$:

$$\alpha_T = \frac{4Z_{13}}{(Z_{12}+Z_{23})^2)} \quad \text{(Eq 3-5)}$$

To have a total transmission, α_T should be set to 1, which leads to the optimized relation between the acoustic impedances of three materials:

$$Z_2 = \sqrt{Z_1\cdot Z_3} \quad \text{(Eq 3-6)}$$

Eq 3-6 shows that if the specific acoustic impedance of matching layer is the geometric mean of that of piezoelectric and interest materials, also the matching layer is quarter wavelength thick, there will be a complete energy transmission at the center frequency. Fig. 3-6 presents the transmission function spectrum of the same transducer with non-matching spectrum given in Fig. 3-2 where it is attached with one matching layer having geometric mean acoustic impedance. The transmitted signal strength increases more than four times. The 6dB two-way bandwidth is now improved to 52.47%.

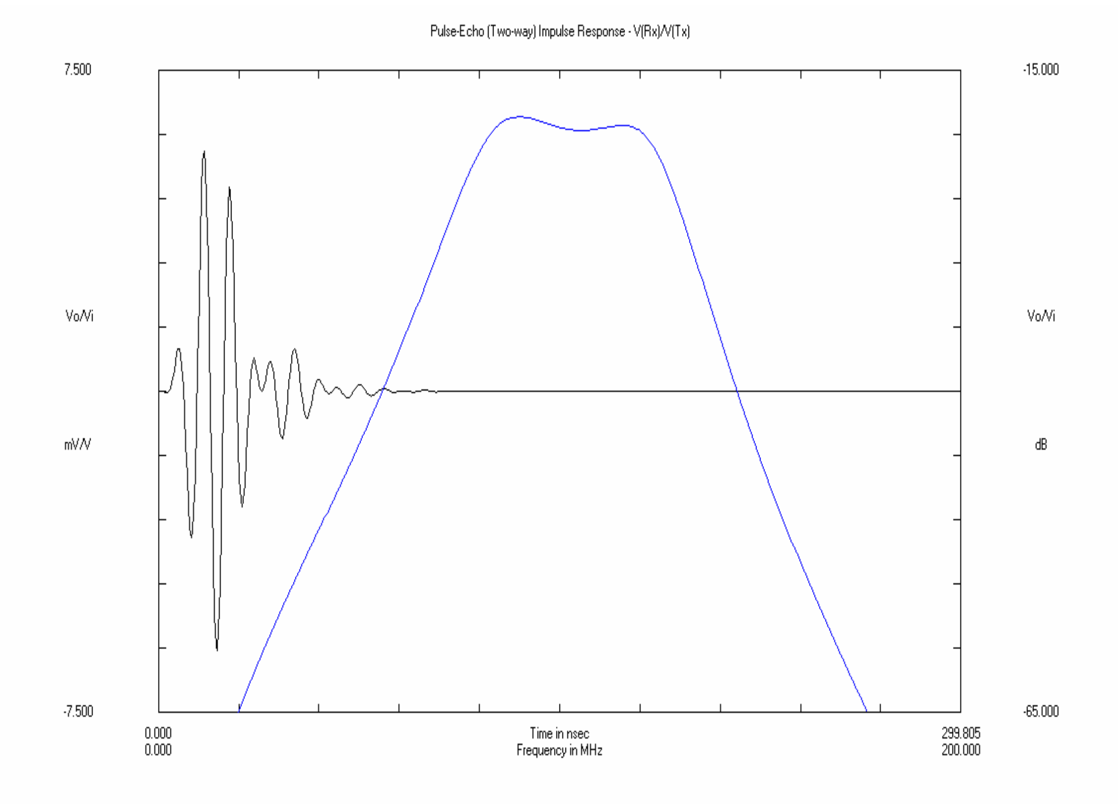

Fig. 3-6: Spectrum of lithium niobate ultrasonic transducer with single layer material having geometric mean acoustic impedance.

3.2.2 Desilets & Fraser Model.

Another approach [DeSilets, Fraser and Kino 1978] to find the optimized matching layer acoustic impedance value was taken by using Krimholtz, Leedom, and Matthaei (KLM) model [Krimholtz, et al.1971] [Leedom, et al.1971]. In the KLM model, transducer is regarded like a transmission line with essentially a short circuit termination. The principle of DeSilets & Fraser model is to treat the whole front half of the transducer as a quarter-wave matching layer. Transformers will be designed to have appropriate impedances at the center terminal of the KLM model. The optimized impedance formula is given as:

$$\ln\left(\frac{Z_{n+1}}{Z_n}\right) = 2^{-N} C_n^N \ln\left(\frac{Z_T}{Z_{IN}}\right) \qquad \text{(Eq 3-7)}$$

Z_T is the terminating load impedance, Z_{IN} is transmission line system input impedance, Z_n is the impedance of nth quarter wavelength matching layer. $C_n^N = \dfrac{N!}{n!(N-n)!}$. Z_R denotes the effective impedance at the transducer surface. A list of the calculation results is given in table 3-1. The transmission function spectrum of transducer in Fig. 3-2 attached with one matching layer having Desilets & Fraser Model impedance is provided in Fig. 3-7. The transmitted signal strength increase is almost the same compared to the data in Fig. 3-6 and the 6dB two-way bandwidth is 45.18%.

Table 3-2: Matching Layer Acoustic Impedance Formulas.

Impedance	Z_{IN}	Z_2	Z_3	Z_R
One Layer	$\frac{Z_C^{2}}{Z_T}$			Z_T
Two Layers	$\frac{Z_C^{\frac{4}{3}}}{Z_T^{\frac{1}{3}}}$	$Z_T^{\frac{2}{3}} Z_C^{\frac{1}{3}}$		$Z_c^{\frac{2}{3}} Z_T^{\frac{1}{3}}$
Three Layers	$\frac{Z_c^{\frac{8}{7}}}{Z_T^{\frac{1}{7}}}$	$Z_T^{\frac{3}{7}} Z_C^{\frac{4}{7}}$	$Z_T^{\frac{6}{7}} Z_C^{\frac{1}{7}}$	$Z_c^{\frac{6}{7}} Z_T^{\frac{1}{7}}$

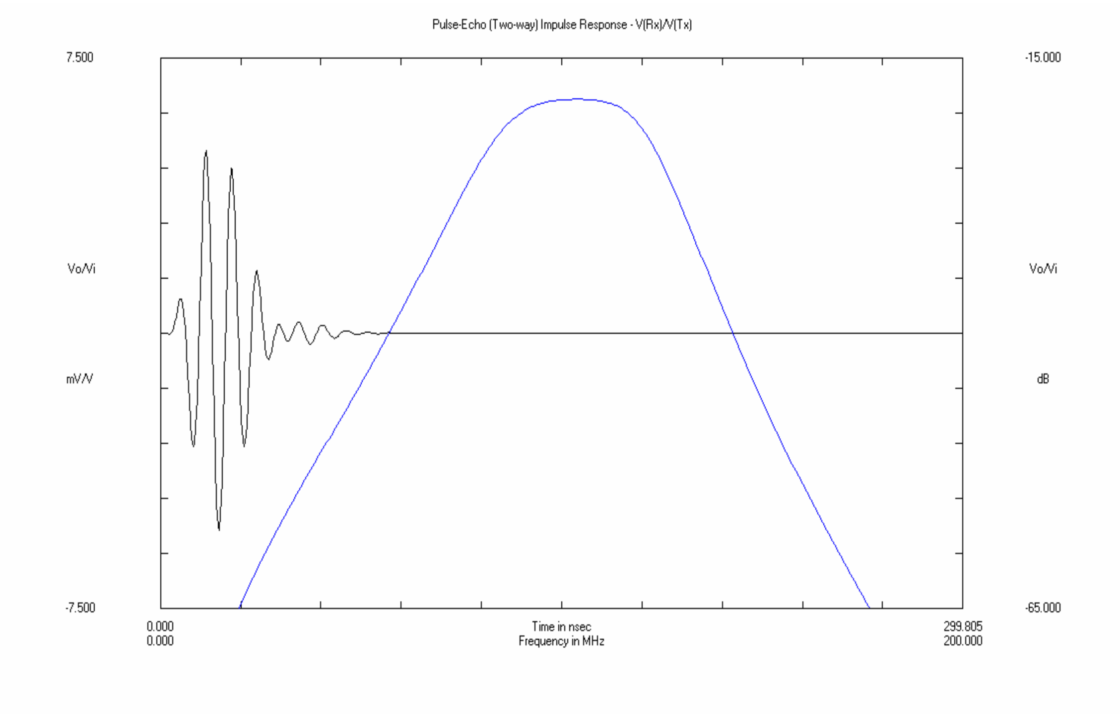

Fig. 3-7: Spectrum of lithium niobate ultrasonic transducer with matching layer material having Desilets & Fraser model acoustic impedance.

3.3 Limitations of Quarter Wavelength Matching Layer Design

Quarter wavelength matching layer design has been used in industry for a long time because its characteristics suit PZT based transducer very well. However, in recent years, research in medical ultrasonic transducer using single crystal PMN-PT or PZN-PT materials has made great progress [Gururaja, et al. 1999] [Sung, Jung 2007]. Different work was done in developing crystal growth technologies, optimizing material properties, and prototyping single crystal ultrasonic devices. Experiments indicate a dramatic bandwidth improvement when using PMN-PT single crystal material to replace PZT ceramics. One single crystal transducer could cover the frequency range of two traditional PZT ceramic transducers as shown in Fig. **3-6**. This extended broad bandwidth and sensitivity could greatly improve transducer's performance in penetration depth and resolution of ultrasonic imaging [Chen, Panda 2005].

Harmonic imaging is now widely used in medical ultrasonic imaging. However, the utilization of this imaging technique was often limited due to its need for simultaneously transmitting f_o and receiving $2f_o$ frequency waves. In order to conduct second harmonic imaging, the ultrasonic transducer must have a very broad bandwidth. Currently used PZT ceramic transducers normally have -6dB bandwidth of about 60%. This is not enough for harmonic imaging. Compared to PZT ceramics, PZN-PT and PMN-PT single crystals can provide -6dB bandwidth of over 100%. This offers a good opportunity in second harmonic imaging. Fig. **3-7** shows a simple schematic comparison between PZT and PMN-PT single crystal transducers. Due to the bandwidth limitation, PZT transducers provide lower sensitivity, while single crystal transducer can offer much higher sensitivity for harmonic imaging.

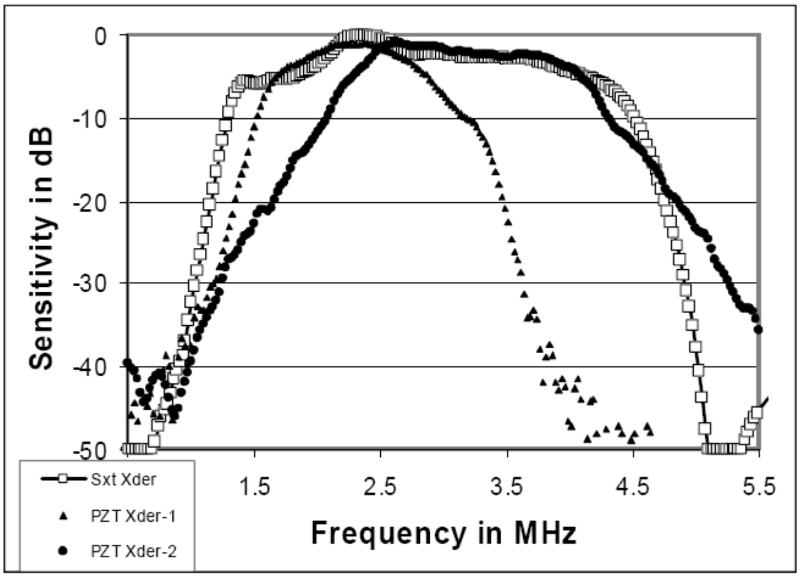

Fig. 3-6: Frequency spectrums of one single crystal transducer and two PZT transducers [Chen, Panda 2005].

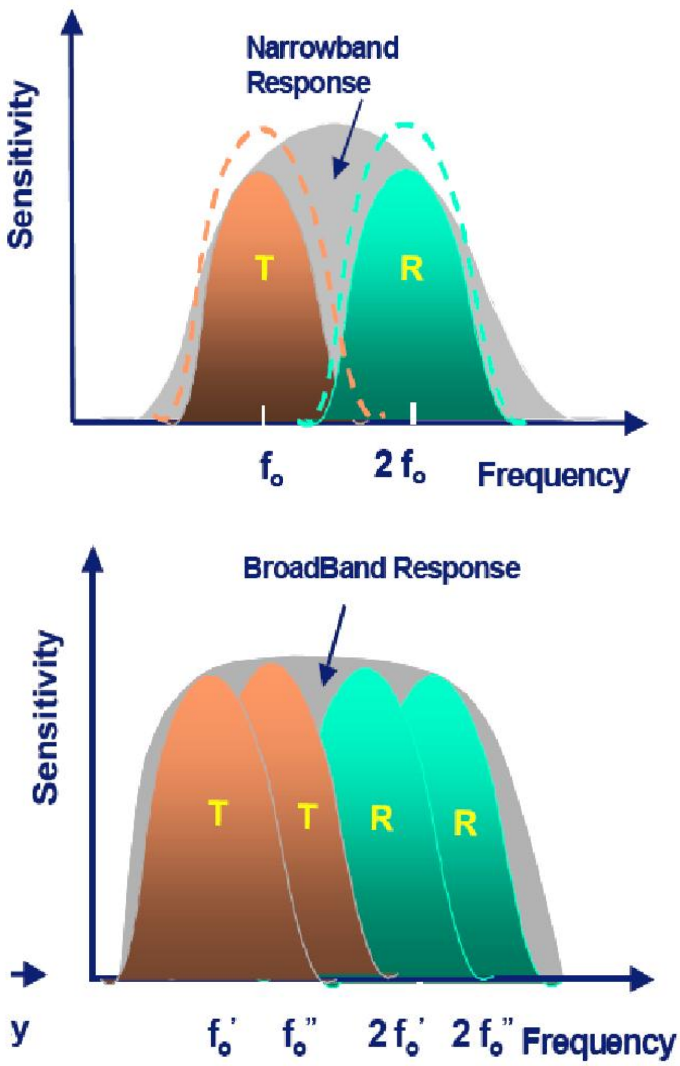

Fig. 3-7: Schematic of frequency spectra of PZT transducer and PMN-PT single crystal transducer [Chen, Panda 2005].

Chapter 4

NEW TiO_2 NANO-STRUCTURED MATERIAL FOR MATCHING LAYER

4.1 Need for New Practical Matching Layer Material for Ultrahigh Frequency Transducers

As discussed in chapter 3, the acoustic impedance of a quarter wavelength matching layer material should be in the range of 5-12 MRayls. At the same time, the attenuation coefficient of matching material should be as low as possible to decrease the energy loss through scattering [Wang et al. 2001]. There are no natural materials that can meet such requirements for matching different piezoelectric resonators. Therefore, powderc-loaded epoxy, vacuum-deposited thin-film of glass and parylene are widely used as matching layer materials, whose acoustic impedance may be tailored by the volume fraction of solid powder. Because the thickness of the matching layer for 100 MHz transducer is only about 8 microns, one must use nano-particles to make the matching layer to avoid scattering effect. However, making high particle loading composites are very difficult, particularly when the particle size is very small. Air bubbles will be trapped into the composite. Vacuum-deposited materials only suit for gigahertz frequencies and matching layer composites become impossible to fabricate using conventional processing techniques beyond 100MHz range [Hadimioglu, Khuri-Yakub].

As mentioned above, conventional composite processing becomes extremely difficult in the case of ultra high frequency transducers whose center frequency climbs beyond 50 MHz [Lockwood, et al. 1996] because under such circumstance, the thickness of matching layer is less than 10 microns, which requires the composite particles' size to be much less than 1 micron.

Previous experience showed that it is hard to load high volume fraction fine powders into a composite without introducing air bubbles using conventional composite processing techniques. Therefore, ultra high frequency transducers currently used or under development are not properly matched because of the lacking of desired materials. This problem hinders the development progress of ultrahigh frequency ultrasonic medical imaging devices with improved resolution.

Recently, some solid nano-particle/polymer composites are developed using sol-gel processing [Zhou, et al. 2006]. This provides a possible solution to solve the high frequency transducer matching problem. The first nano-composite matching layer material developed was a SiO_2 based nano-composite [Wang, Cao, et al. 2004]. This composite has good uniformity and its acoustic impedance can be adjusted from 2.2 -5.7 MRayls. Although this is a big step forward in the right direction, the acoustic impedance of this SiO_2 nano-composite is still not high enough for a lot of practical medical applications. Particularly, for those transducers require high sensitivity, the acoustic impedance of the matching layer should be about 8 MRayls. If double matching layers are used, the outer layer must have impedance about 12 MRayls.

In addition, the Sol-Gel film is difficult to lift off the substrate and the spin-coating method is not convenient to use. Therefore, it would be desirable if the fabrication process can be further simplified and the processing temperature can be lowered so that the matching layers can be directly coated onto the transducer without causing depoling of the piezoelectric piece.

4.2 Components & Fabrication

We have developed a novel TiO_2 nano-structured material with higher acoustic impedance than the previous SiO_2 nano-composite but much simpler processing procedure. This material has porous nano-structure. The volume fraction of voids is controlled by the amount of bonding amorphous phase in the material. Its acoustic impedance can be tuned by adjusting the total volume fraction of voids using different sintering temperatures.

Nano-sized titanium dioxide (TiO_2) is one of the most important materials currently being studied in various fields. It has great potential for many practical applications [Carotta, Ferroni, et al. 1999] [Grätze 2001]. However, the attention so far has been mainly focused on its optoelectric and dielectric characteristics. Up to date, there has not been investigation reported on utilizing TiO_2's acoustic properties. Compared to SiO_2, the acoustic impedance of TiO_2 is almost two times (~16 MRayls) high. Therefore, we can expect materials made of TiO_2 nano particles to have higher acoustic impedance and better tunability than SiO_2 nano-composites.

From recent researches on designing dye-sensitized solar cells [Zhang, Yoshida, et al. 2006] [Zhang, Downing, et al. 2006], it was found that TiO_2 nano particles can be turned into porous nanostructures at room temperature by adding small amount of Ti^{iV} tetraisopropoxide (TTIP) and diluting the mixture with ethanol solution. TTIP (molecular structure is shown in Fig. 4-1) is a chemical compound normally used in organic synthesis and materials science field, especially in depositing titanium dioxide [Dalapati, et al. 2003] [Campbell, et al. 1997].

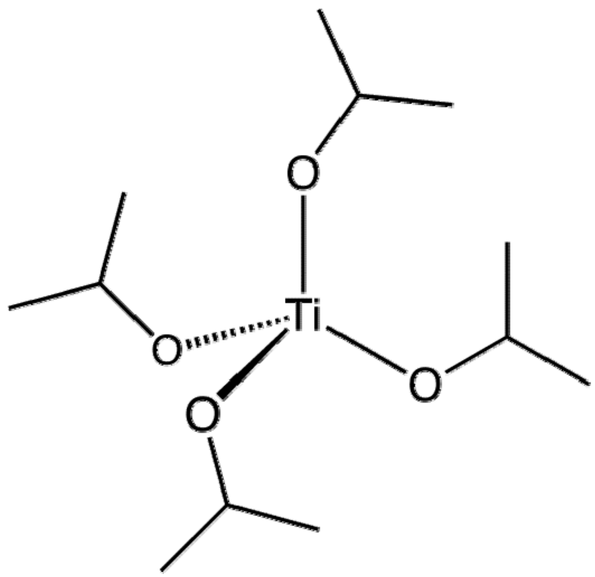

Fig. 4-1: Titanium Tetraisopropoxide [Wright, Williams 1968].

TTIP can be hydrolyzed in situ at room temperature to form bonds between TiO_2 nano particles. Ethanol will evaporate at room temperature. The TiO_2 formed from TTIP is amorphous which can crystallize if the sample is annealed at a temperature > 400 ^oC.

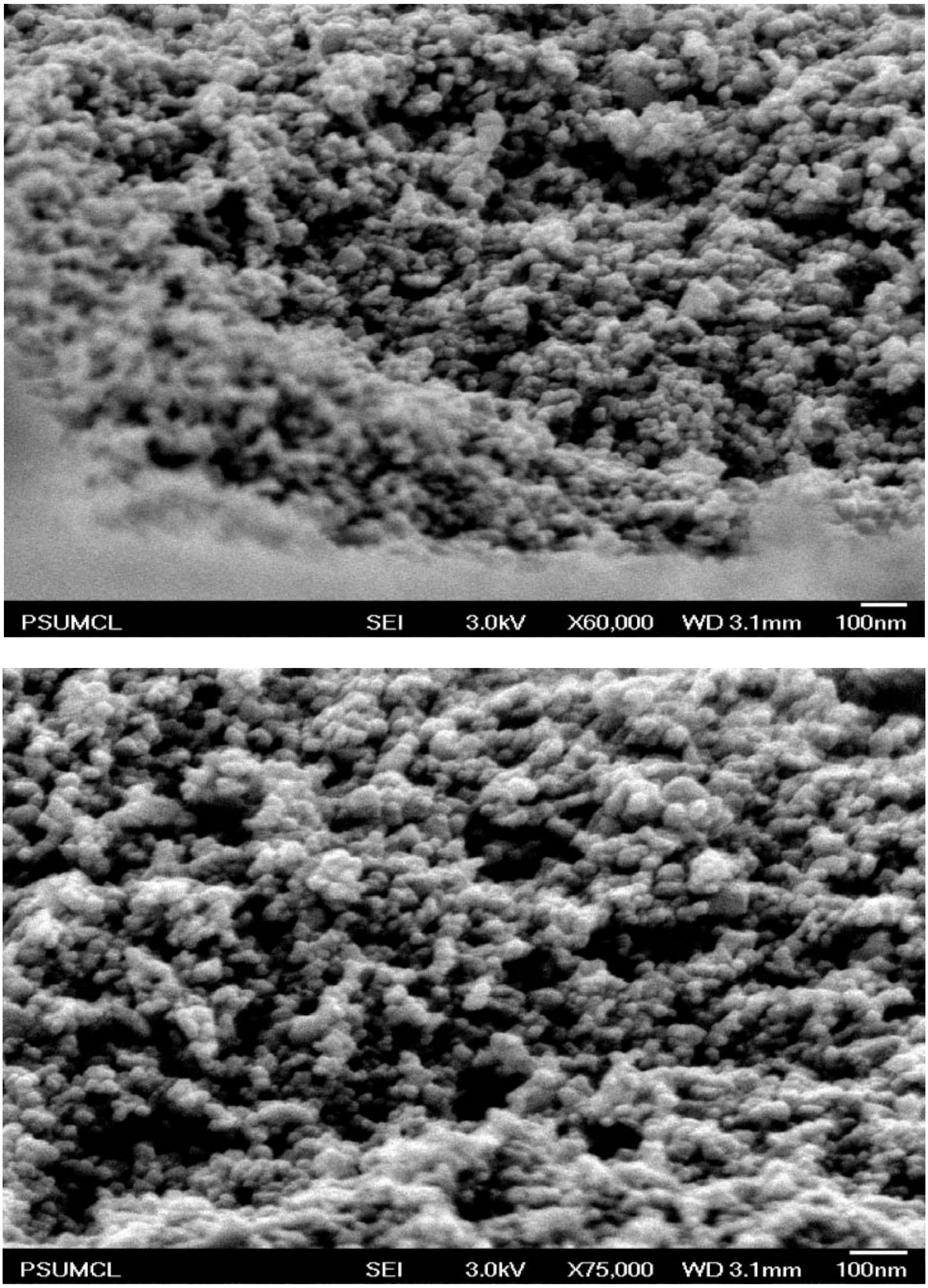

Fig. 4-2: SEM photos of TiO_2 nano-structured material with nano-size TiO_2 particles.

However, for matching layer applications, the acoustic impedance is the key parameter while crystallization is irrelevant. Because the TTIP does not completely fill the voids between the TiO_2 nano-particles, the film contains sub-nanometer pores (closed type). Such porous nano-structured material is a natural TiO_2/air nanocomposite. Microstructure photos of this material obtained through scanning electron microscopy (SEM) are shown in Fig. **4-2**.

The TiO_2 nano particles were purchased from Degussa, Germany. These particles contain 30% rutile and 70% anatase, the average particle size is around 25nm. To make the mixture, molar ratio of TiO_2/TTIP/Ethanol was set at 1.0:0.05:6.0. The mixture was dispersed using an ultrasonic horn for 30 minutes.

Ultrasonic horn is a device that can concentrates acoustic energy locally and applies it. When the horn tip is brought in contact with the mixture at a certain pressure, frictional heat is generated causing the mixture to plasticize locally, creating a connection between two materials in a short period of time. After the horn is removed, the mixture will cure and create the bond. Typical frequency used ranges from 20 to 60 kHz. There are many horns having difference sizes and configurations depending on the task. Fig. **4-3** shows several different ultrasonic horn devices. In our experiments, we used Hielscher-Ultrasonic Technology UP400S system which is shown in Fig. **4-34**.

The amount of TTIT can be adjusted to control the acoustic impedance of final material since it determines the size of the voids (generally sub-nanometer) in the final products. The porous structure is 3-D continuous as shown with the atomic force microscopy (AFM) micrograph in Fig. 4-66. Several samples we made all presented the same microstructure and uniformity.

Fig. 4-3: Different ultrasonic horn devices. www.mtiinstruments.com

Fig. 4-4: Hielscher-Ultrasonic Technology UP400S ultrasonic horn system.
www.hielscher.com

Thin films of ~10 μm thick can be prepared using the doctor-blade method by coating the mixture onto glass or piezoelectric material substrates. A flat blade is fixed at certain height above a moving substrate, with the mixture reservoir behind the blade to spread a uniform thin coating onto the substrate as shown in Fig. 4-5. The fabricated films using doctor-blade technique have similar morphology with those fabricated by traditional method [Barbé, Arendse, et al. 1997].

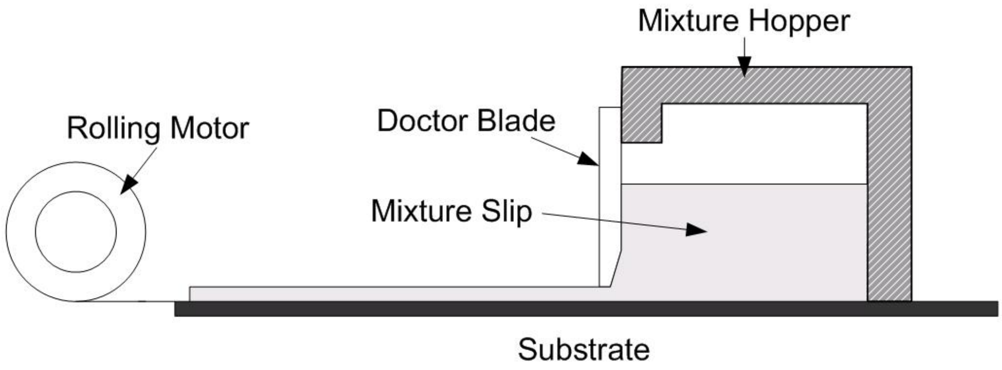

Fig. 4-5: Schematic of doctor-blade technique system.

Fig. 4-87 presents the photo taken by scanning electron microscopy (SEM) of final thin film material deposited on silicon substrate, homogeneously distributed TiO_2 nano particles are well bonded together. The histogram shows the particle size distribution in this nano-structured material ranges between 20-30 nanometers. Fig. 4-8 is another SEM micrograph but with less resolution, it clearly shows that the thin film is firmly attached to the silicon substrate and the doctor-blade technique produced uniform film.

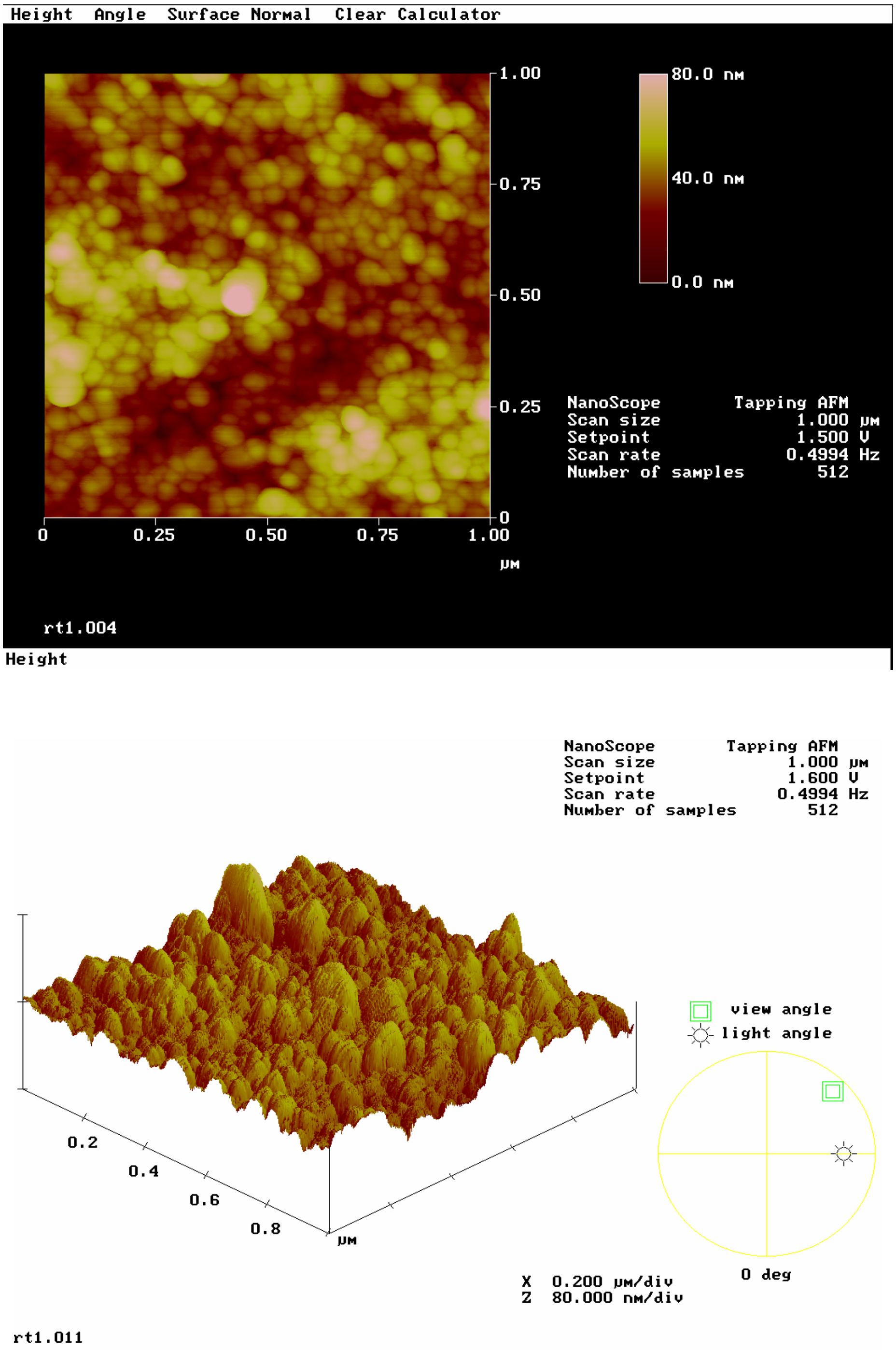

Fig. 4-6: AFM micrograph of TiO_2-polymer nano-composite.

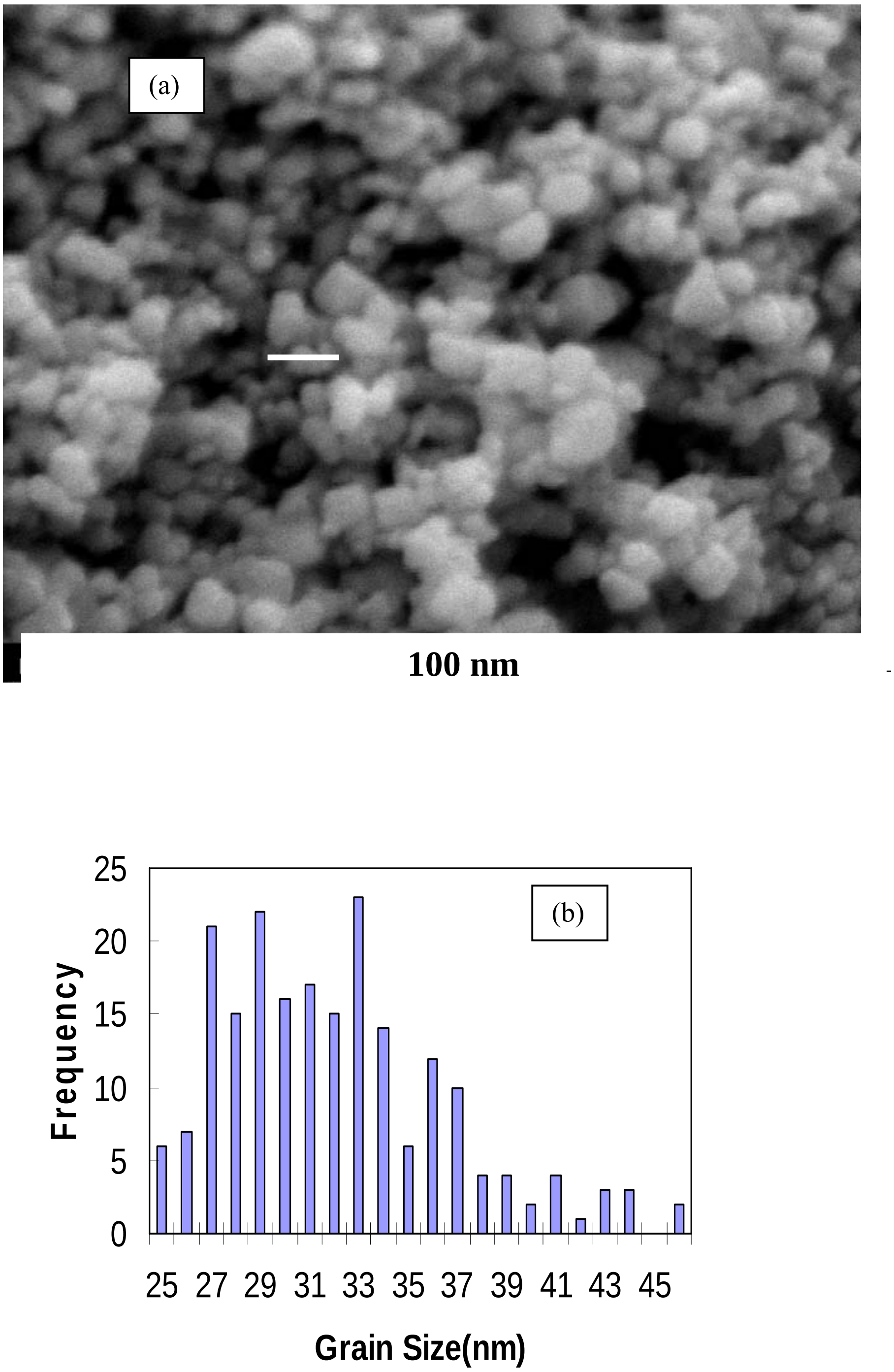

Fig. 4-7: (a) SEM micrograph of TiO_2 nano-structured film shows the size of TiO_2 particle around 25nm. (b) The histogram showing the particle size distribution.

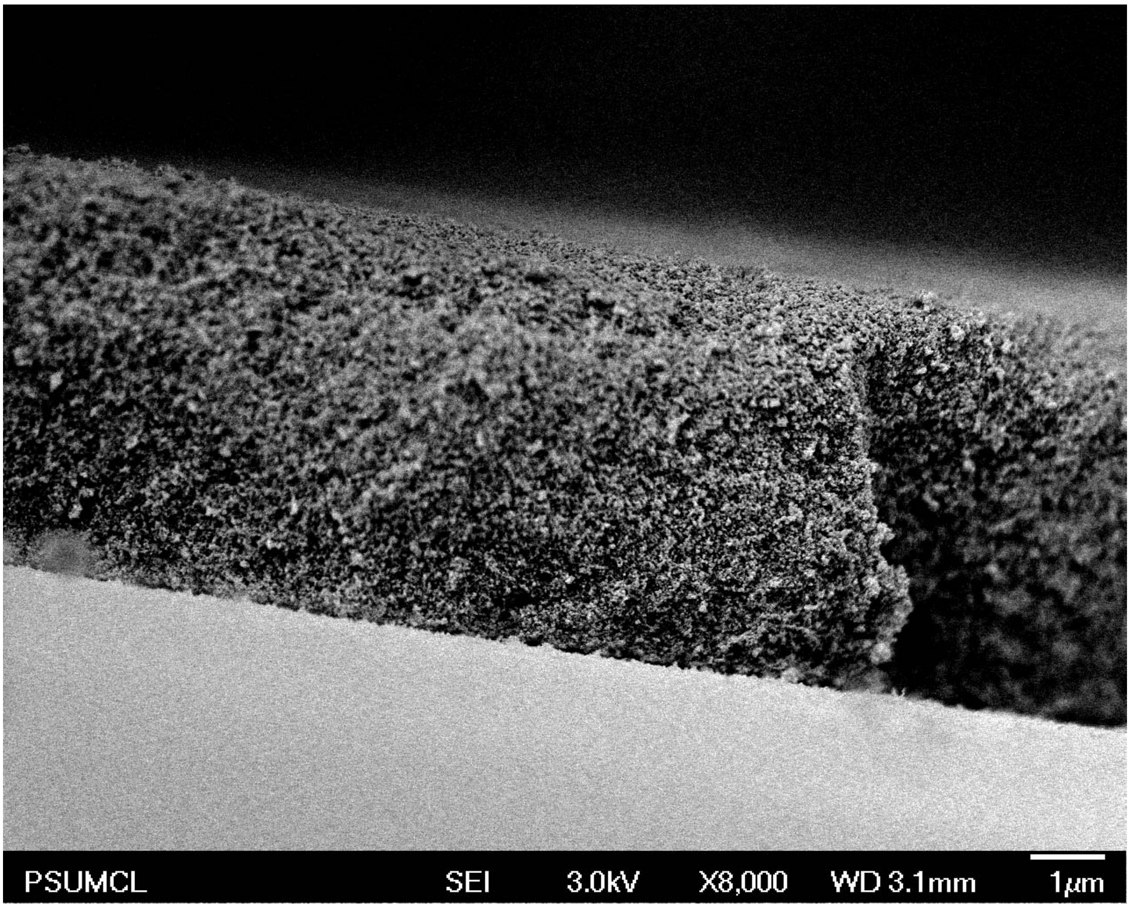

Fig. **4-8**: SEM photo shows new TiO_2 nano-structure material particle is well bonded together and firmly attached to the substrate.

4.3 Acoustic Property Measurements

4.3.1 Traditional Pulse-echo Method

Tradition pulse echo method has been widely used in sound speed measurement. As presented in Fig. 4-9, acoustic pulse wave is reflected at the front and back surface of the sample. Using the sample thickness d and the time difference T between two reflected consecutive echoes, the sound speed of the measured sample v can be calculated by:

$$v = 2d / T \qquad \text{(Eq 4-1)}$$

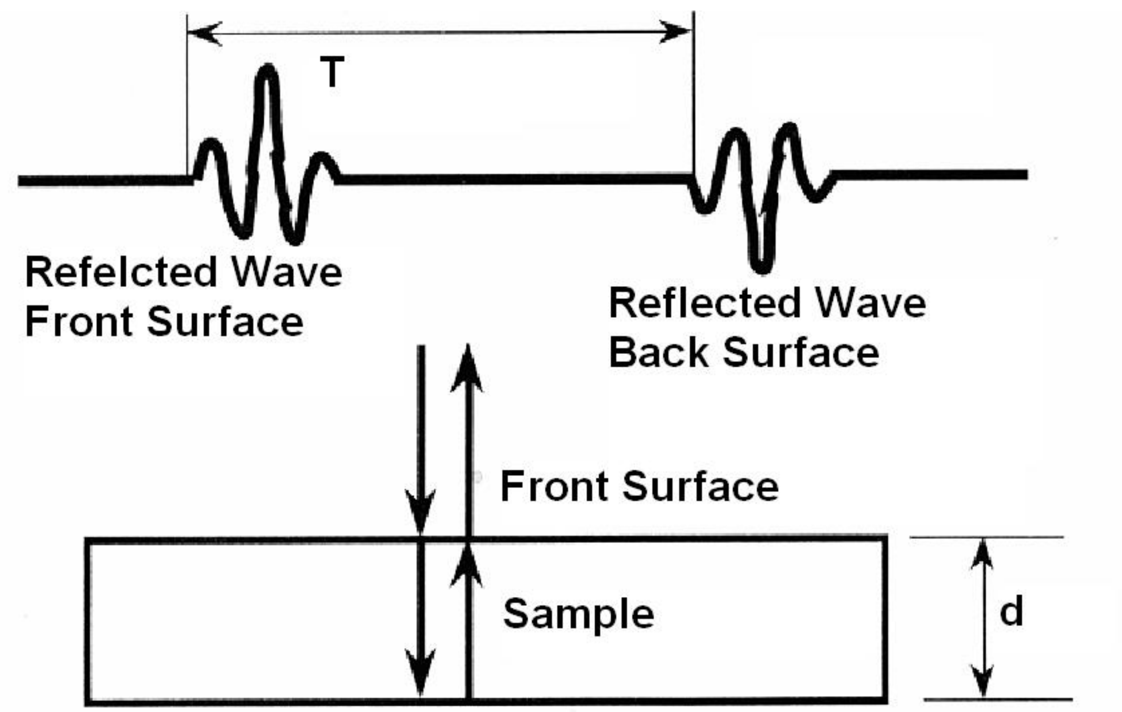

Fig. 4-9: Traditional method for sound speed measurement.

However, samples used in this method are required to have thickness at least three times larger than the wavelength of the ultrasonic wave so that the two successive reflected pulses can be well separated. Due to size effect, very thin layer material may have different properties than that of the bulk material [Lu, Rhyne, et al. 1998]. Many thin film technique also could not produce the properties of bulk materials. Therefore, new methods are still needed to directly characterize even thinner layer materials.

4.3.2 New Methods for Thin Layer Material Characterization

Two methods, based on ultrasonic quarter wavelength matching and T-matrix technique principle, respectively, have been developed to measure the acoustic properties of TiO_2 nano-structured thin film material.

The quarter wavelength method is more applicable when the substrate is relatively thick so that the multiple reflected waves within the thin film layer can be separated from the successive waves reflected back from the substrate/water interface.

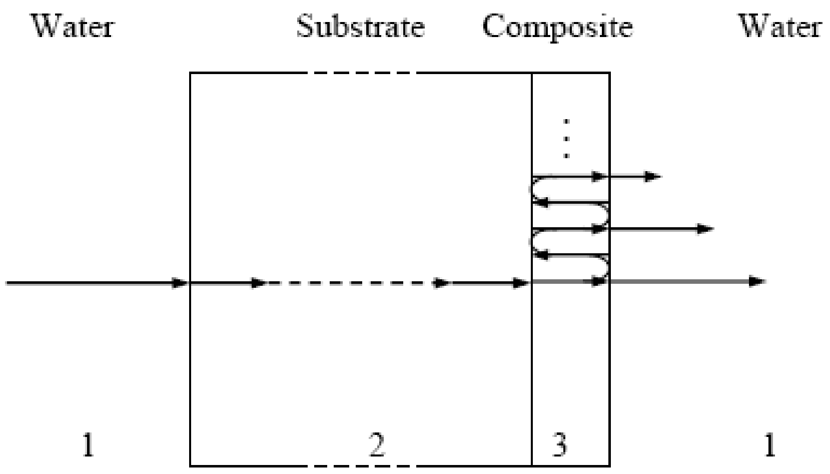

Fig. **4-10**: Pulse signal transmitted through thin layer composite on a thick glass substrate immersed in water.

By analyzing wave propagation in the structure shown in Fig. **4-10**, the incident wave can be expressed by:

$$u^{in} = u_0(2\pi f - k_1 x) \qquad \text{(Eq 4-2)}$$

Where f is the wave frequency and k_1 is the wave number in material 1. The multiple reflected/transmitted signals in thin film can be written as [Wang, Cao, et al. 2003]:

$$\begin{aligned}
&u^{I}(x,t) = T_{12}T_{23}T_{31}u_0(2\pi ft - k_1x - (k_2 - k_1)d_2 - (k_3 - k_1)d_3) \\
&u^{II}(x,t) = T_{12}T_{23}T_{31}R_{31}R_{32}u_0(2\pi ft - k_1x - (k_2 - k_1)d_2 - (3k_3 - k_1)d_3) \\
&u^{III}(x,t) = T_{12}T_{23}T_{31}(R_{31}R_{32})^2u_0(2\pi ft - k_1x - (k_2 - k_1)d_2 - (5k_3 - k_1)d_3) \\
&\cdots\cdots \\
&\cdots\cdots
\end{aligned} \qquad \text{(Eq 4-3)}$$

d_i denotes the thickness of layer i. T_{ij} and R_{ij} are, respectively, transmission and reflection coefficients between layer i and j. The hybrid transmitted signal at x=L, consisting of u^I, u^{II}, u^{III} and so on, is given by:

$$\begin{aligned} u^T(L,t) &= g(t) \\ &= T_{12}T_{23}T_{31}\sum_{m=0}^{\infty}(R_{31}R_{32})^m u_0(2\pi ft - k_1x - (k_2-k_1)d_2 - ((2m+1)k_3-k_1)d_3) \end{aligned} \quad \text{(Eq 4-4)}$$

Suppose that G(f) and $U_0(f)$ are the FFTs of g(t) and $u_0(t)$, we have:

$$G(f) = T_{12}T_{23}T_{31}e^{-i(k_2-k_1)d_2}e^{-i(k_3-k_1)d_3}U_0^*(f)\sum_{m=0}^{\infty}(R_{31}R_{32}e^{-i2k_3d_3})^m \quad \text{(Eq 4-5)}$$

If we define $\delta = R_{31}R_{32}e^{-i2k_3d_3}$, when $|\delta| < 1$, $\sum_{m=0}^{\infty}\delta^m = \frac{1}{1-\delta}$, then:

$$G(f) = T_{12}T_{23}T_{31}e^{-i(k_2-k_1)d_2}e^{-i(k_3-k_1)d_3}U_0(f)\frac{1}{1-R_{31}R_{32}e^{-i2k_3d_3}} \quad \text{(Eq 4-6)}$$

Now we consider the scenario of only the substrate in the water medium, i.e., layer 3 in Fig. 4-10 no longer exists, the first transmitted signal at x = L is

$$h(f) = T_{12}T_{23}u_0(2\pi ft - k_1L - (k_2-k_1)d_2) \quad \text{(Eq 4-7)}$$

The corresponding Fourier transform is:

$$H(f) = T_{12}T_{21}e^{-i(k_2-k_1)d_2}U_0(f) \quad \text{(Eq 4-8)}$$

Dividing Eq 4-6 by Eq 4-8 gives:

$$\frac{G(f)}{H(f)}=\frac{T_{23}T_{31}}{T_{21}}\frac{e^{-i(k_3-k_1)d_3}}{1-R_{31}R_{32}e^{-i2k_3d_3}} \qquad \text{(Eq 4-9)}$$

For dispersive mediums, wave numbers are complex numbers: k=β-iα, α is the attenuation coefficient. Eq **4-9** can be rearranged as:

$$\frac{G(f)}{H(f)}=\frac{T_{23}T_{31}}{T_{21}}\frac{e^{-i(\beta_3-\beta_1)d_3}e^{-(\alpha_3-\alpha_1)d_3}}{1-R_{31}R_{32}e^{-2\alpha_3d_3}e^{-i2\beta_3d_3}} \qquad \text{(Eq 4-10)}$$

From the above equation, the amplitude of the spectrum ratio can be derived:

$$\left|\frac{G(f)}{H(f)}\right|=\frac{T_{23}T_{31}}{T_{21}}\frac{e^{-(\alpha_3-\alpha_1)d_3}}{\left|1-R_{31}R_{32}e^{-2\alpha_3d_3}e^{-i2\beta_3d_3}\right|} \qquad \text{(Eq 4-11)}$$

Because the acoustic impedance having the relation of $Z_1 < Z_3 < Z_2$, $R_{31}R_{32}<0$, therefore, the ratio |G(f)/H(f)| peaks when $\beta_3 d_3 = (n+1/2)\pi$, n= 0, 1, 2, …, and the corresponding frequency is:

$$f_{max,n}=(n+\frac{1}{2})\frac{v_3(f_{max,n})}{2d_3} \qquad \text{(Eq 4-12)}$$

When n = 0, the sound speed of the thin layer at the corresponding frequency is

$$v = 4f_{max,0}d_3 \qquad \text{(Eq 4-13)}$$

where d_3 is the thickness of the thin film.

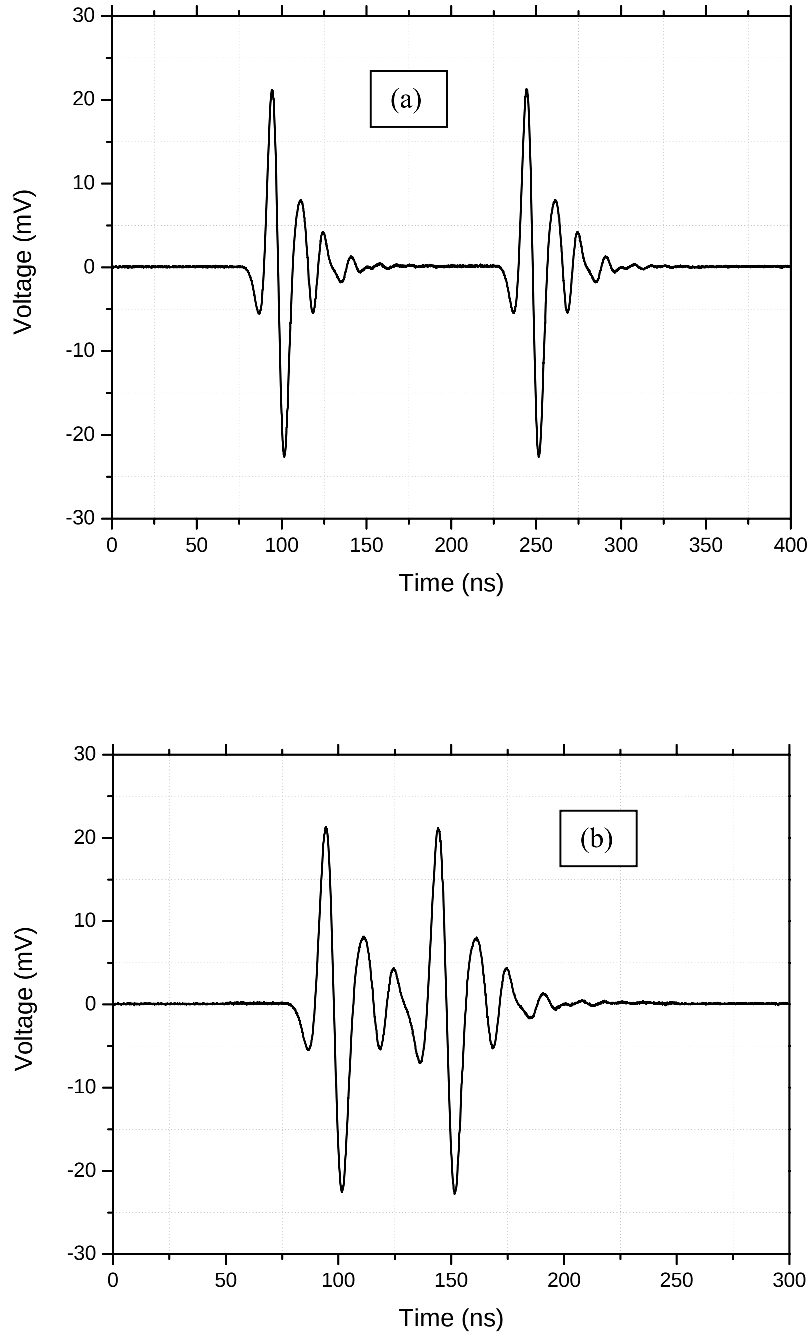

Fig. 4-11: (a) The two signals are separated. (b) Two signals are too close and the wave forms interfere with each other.

When the thickness of substrate becomes close to that of thin film, as shown in Fig. 4-11(b), the reflected waves from the layer 2-3 interface will interfere with the waves reflected from the 1-2 interface. Those waves are no longer separable from each other as presented in Fig. 4-111(a). For such cases, it becomes almost impossible to use the quarter wavelength method to perform the characterization. Wave propagation under such condition is illustrated in Fig. 4-12:

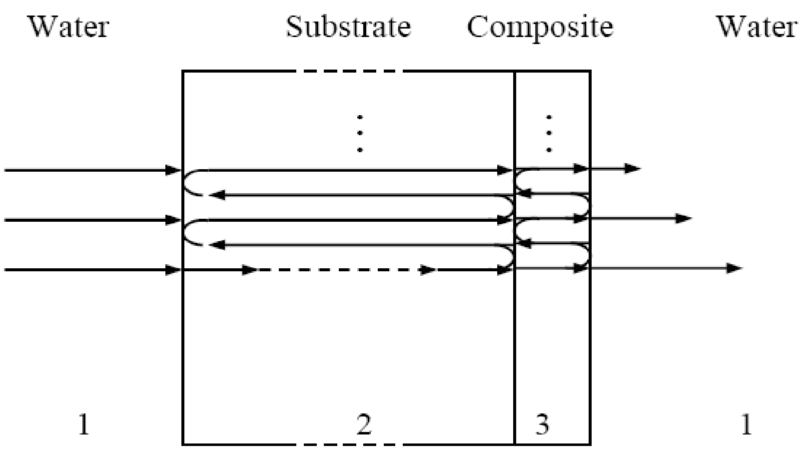

Fig. 4-12: Continuous wave transmitted through thin composite layer deposited on thin substrate immersed in water.

To deal with material characterization under this complex situation, method based on the T-matrix principle is developed to treat wave propagation in two thin layers. Continuous or tone burst ultrasonic waves as shown in Fig. 4-13 are utilized.

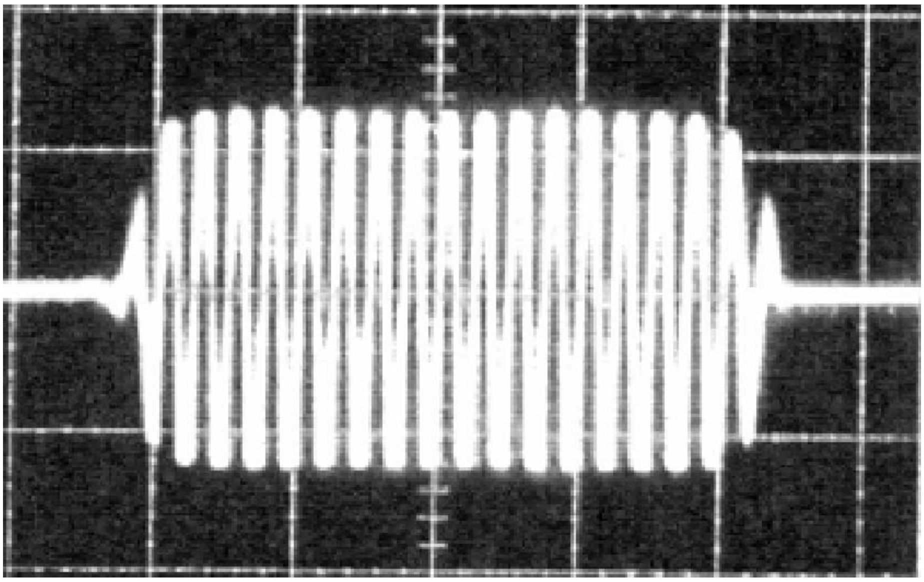

Fig. **4-13**: Tone-Burst ultrasonic wave form.

Base on the description in Chapter 2, for a multilayer structure shown in Fig. **4-12**, the continuous wave form in each layer is:

$$y_j = A_j e^{i(\omega t - k_j x)} + B_j e^{i(\omega t + k_j x)} \qquad \text{(Eq 4-14)}$$

The transmission matrix of A_j and B_j at each boundary, the total transmission matrix [T] and the out-to-in wave amplitude ratio are, respectively,

$$\begin{pmatrix} A_j \\ B_j \end{pmatrix} = \left[T_{j,j+1}\right] \begin{pmatrix} A_{j+1} \\ B_{j+1} \end{pmatrix} = \frac{1}{2Z_j} * \begin{pmatrix} (Z_j + Z_{j+1})e^{ik_{j+1}(l_{j+1}-l_j)} & (Z_j - Z_{j+1})e^{-ik_{j+1}(l_{j+1}-l_j)} \\ (Z_j - Z_{j+1})e^{ik_{j+1}(l_{j+1}-l_j)} & (Z_j - Z_{j+1})e^{-ik_{j+1}(l_{j+1}-l_j)} \end{pmatrix} \begin{pmatrix} A_{j+1} \\ B_{j+1} \end{pmatrix} \qquad \text{(Eq 4-15)}$$

$$[T] = [T_{1,2}][T_{2,3}][T_{3,1}] \qquad \text{(Eq 4-16)}$$

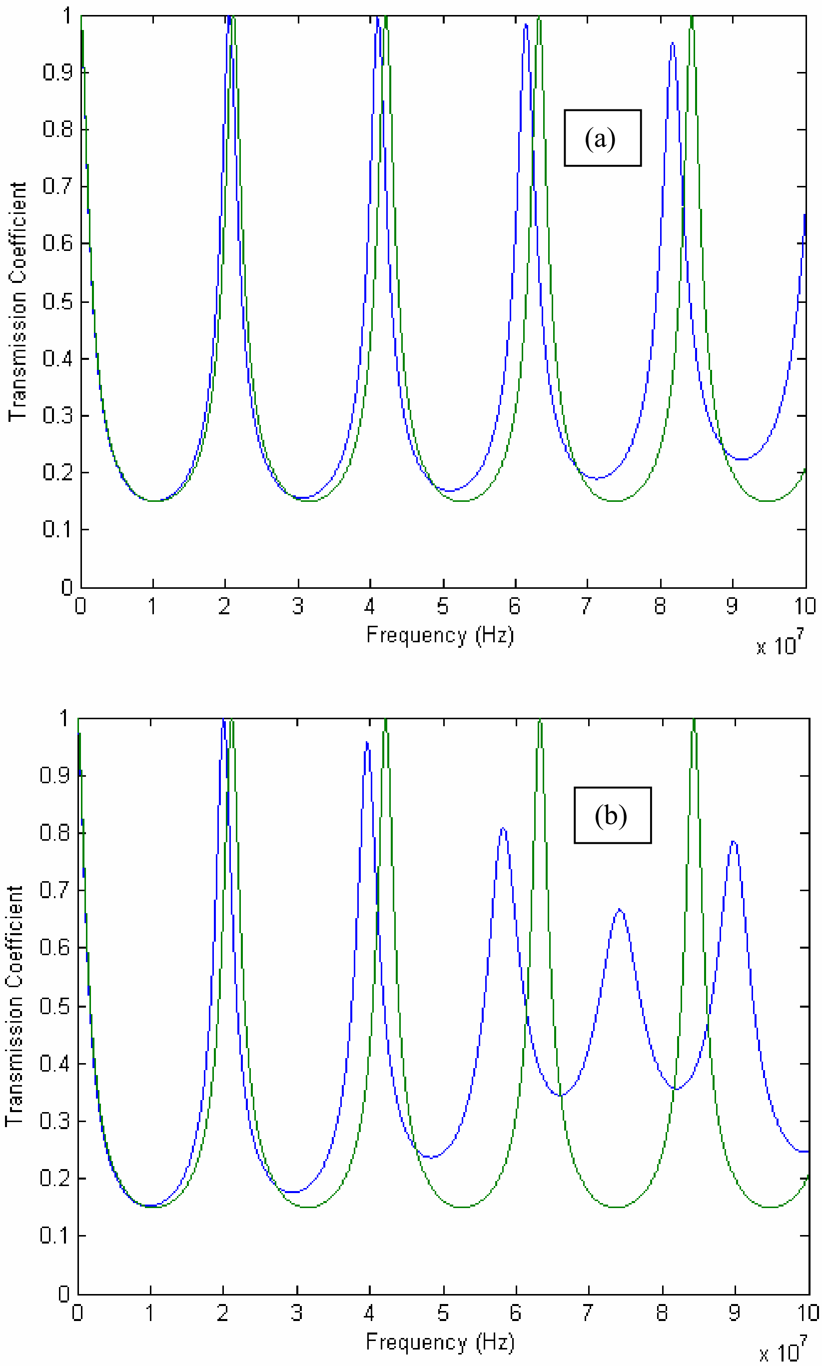

Fig. 4-14: Transmission coefficients of waves through 0.1mm thick silicon substrate with 5 (a) and 10 (b) microns thick thin film. Green lines denote signal spectrums through substrate only, blue lines show signal spectrums through substrate with thin coating.

$$\frac{A_4}{A_1} = \frac{1}{T_{11}} \quad \text{(Eq 4-17)}$$

From our calculation results shown in Fig. 4-14, the substrate effects usually dominate the receiving signal when it is much thicker than the thin film. The thin film layer only causes some perturbations, which becomes more significant as the film is getting thicker or the substrate is getting thinner. Therefore, the T-matrix method can be used when the thickness of the film is comparable to that of the substrate.

4.4 Experiments and Results

4.4.1 Experimental Setup

In order to precisely measure the sound speed of the new nano structured TiO_2 thin films, through-transmission ultrasonic spectroscopy technique based on quarter wavelength matching principle has been used. The schematic of system setup is shown in Fig. 4-15. One pair of 100 MHz immersion type ultrasonic transducers (Valpey–Fisher E9934) are carefully put into a water tank filled with deionized water and as shown in Fig. 4-16 aligned by a customized 3-D automatic rotor slider system.

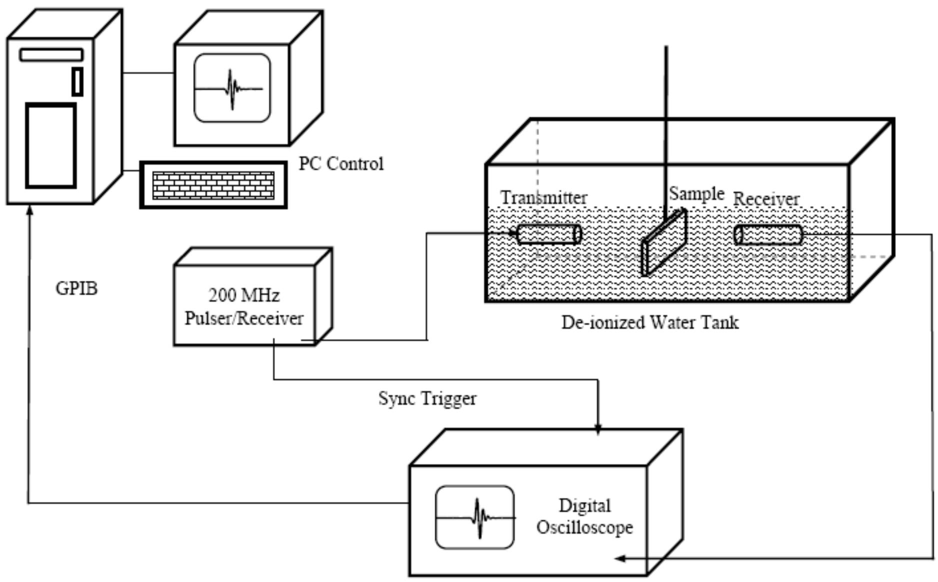

Fig. 4-15: Illustration of experiment system.

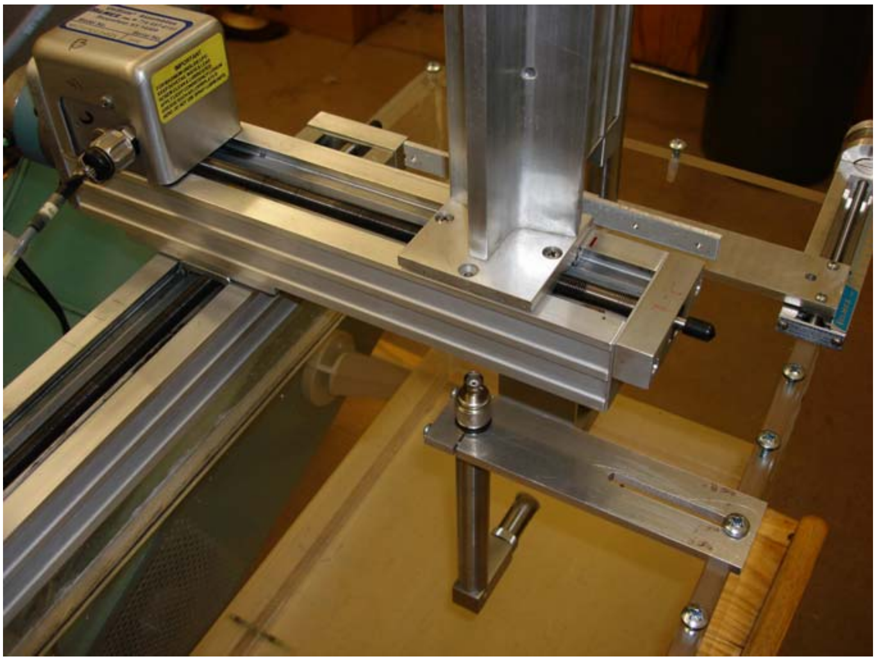

Fig. 4-16: Aligned ultrasonic transducers with rotor motor.

A Panametrics 5052PR 200 MHz pulser/receiver was used to drive the transducers and amplify the received signals for later analysis. After being averaged for 64 times, the received signals become steady and are acquired by a Tektronix TDS 430 digital oscilloscope, sampling window was set at 2500 points. Data were then downloaded to a personal computer via GPIB interface by a C++ programmed application. Fast Fourier transforms (FFTs) were performed using MATLAB®. The frequency resolution of the final results is 0.2 MHz.

The density of TiO_2 material is measured simply by the Archimedes' Principle: "any body partially or completely submerged in a fluid is buoyed up by a force equal to the weight of the fluid displaced by the body." To decrease the influence of surface tension, xylene has been used instead of water.

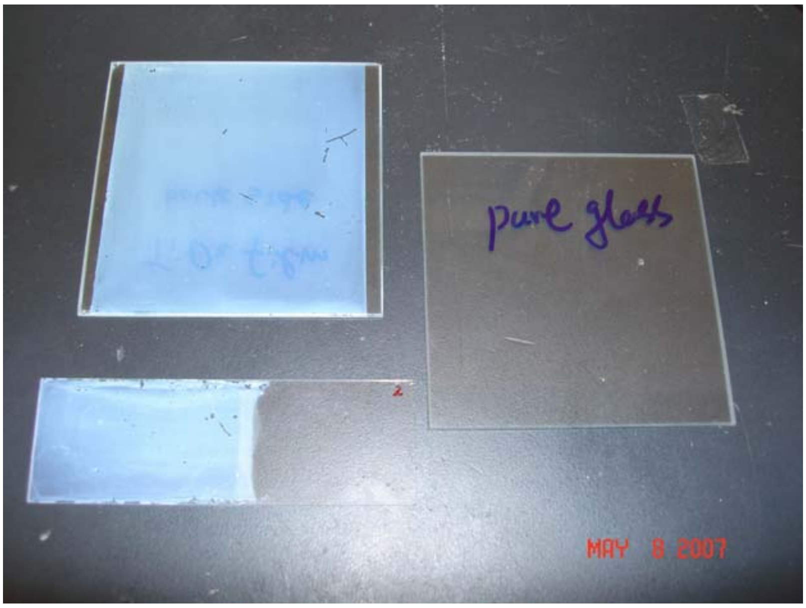

Fig. 4-17: Samples used in experiments.

Several samples were prepared with each one has about 8 micron thick nano-structured TiO_2 nano-structured material thin layer deposited on fluorine doped SnO_2 coated conductive glass (Asahi FTO/glass, 10Ω/□). Glass plates without coating are also prepared. Some of them are shown in Fig. 4-177.

4.4.2 Experiments Results and Analysis

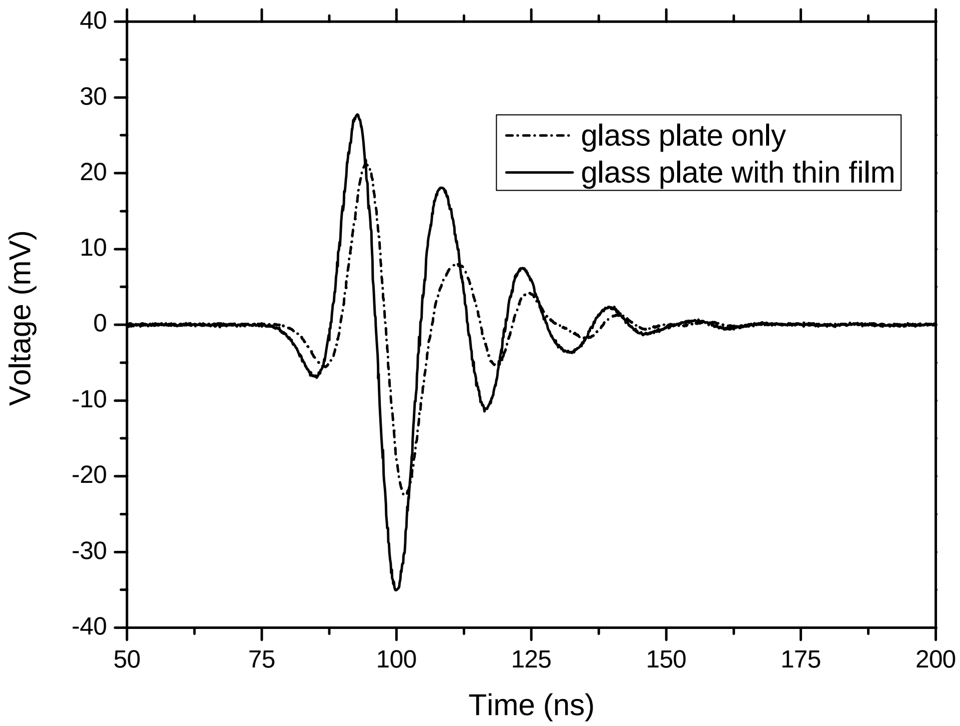

Fig. 4-18: Received signals through samples with and without thin nano-structured TiO_2 material film.

Fig. 4-18 presents the received signals through same glass plate with and without thin TiO_2 nano-structured film. This sample has been cured at room temperature. The total propagation time of the signal through substrate with thin film coating is less than the one without coating, which is due to the fact that TiO2 film has larger wave speed compared to that of water. Because of the multiple reflections inside the thin layer, signal strength also increased from 20-25mV to 30-35mV.

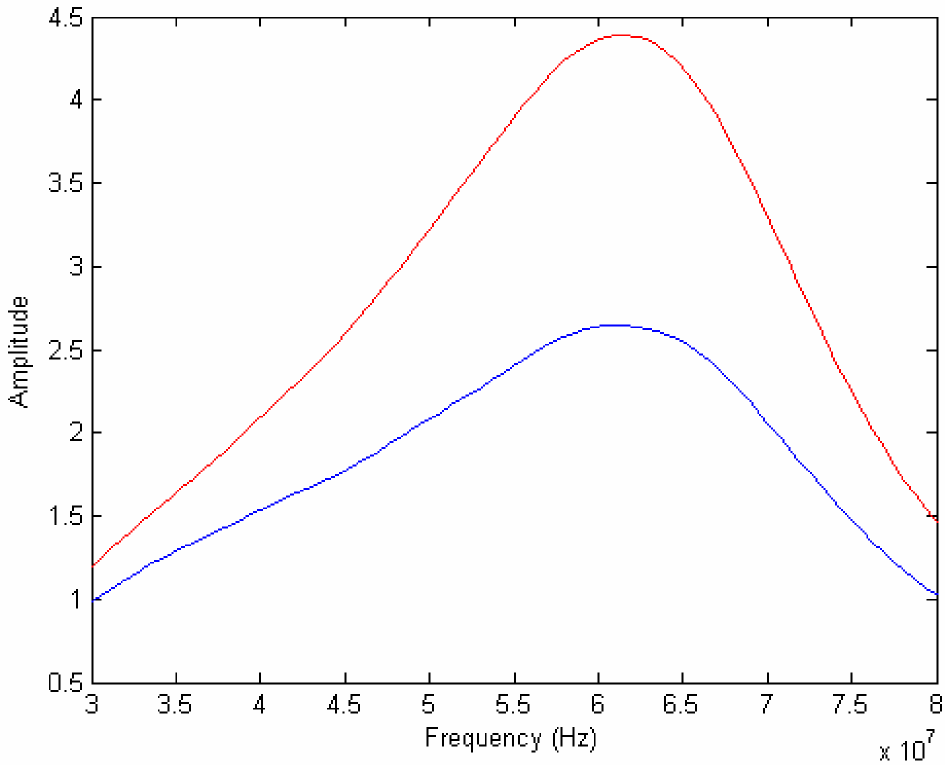

Fig. 4-19: Received signals through glass plate (blue), glass plate with thin film (red) (cured at room temperature).

The frequency spectrums of those two signals in Fig. **4-18** after FFTs are shown in Fig. **4-19**, the differences between the two signals are very clear. From the calculation results, the signal ratio peak is located at 61MHz. From Eq **4-18**, the sound velocity of the thin film material is 1953m/s. The density is also measured as $2715\,\mathrm{kg/m^3}$, so that the acoustic impedance of new TiO_2 nano-structured material is 5.30MRayls.

In order to further strengthening the bonding between the TiO_2 nano particles and increase the material's density, the samples were annealed in an oven progressively at 20 ^{o}C, 50 ^{o}C, 80 ^{o}C, 110 ^{o}C and 140 ^{o}C, for about one hour at each temperature. The corresponding FFT results of signals from substrate only: $G(f)$, and results of signals from substrate with thin film: $H(f)$ are obtained and shown in Fig. **4-20**. These data are further used to calculate the spectra ratio and sound speed.

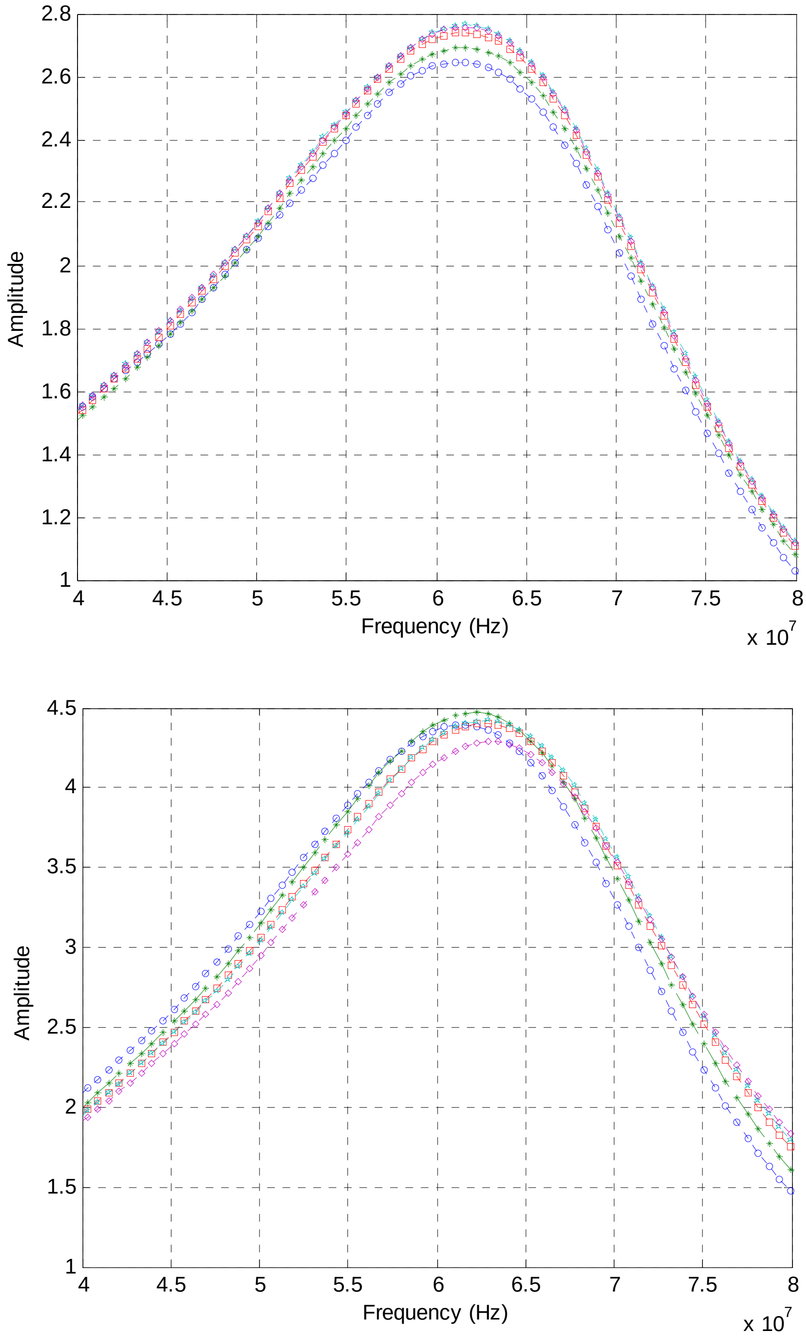

Fig. **4-20**: Received signals through glass plate (a), glass plate with thin film (b) (Blue: $20^{\circ}C$; Green: $50^{\circ}C$; Red: $80^{\circ}C$; Light Blue: $110^{\circ}C$; Purple:$140^{\circ}C$)).

Fig. 4-21 presents the shift of the ratio $\left|\frac{G(f)}{H(f)}\right|$ vs frequency curve after different temperature treatments. From the results it is obvious that the peak frequency increases with the annealing temperature, which means that higher temperature heat treatment will lead to an increase of the sound velocity for the final product.

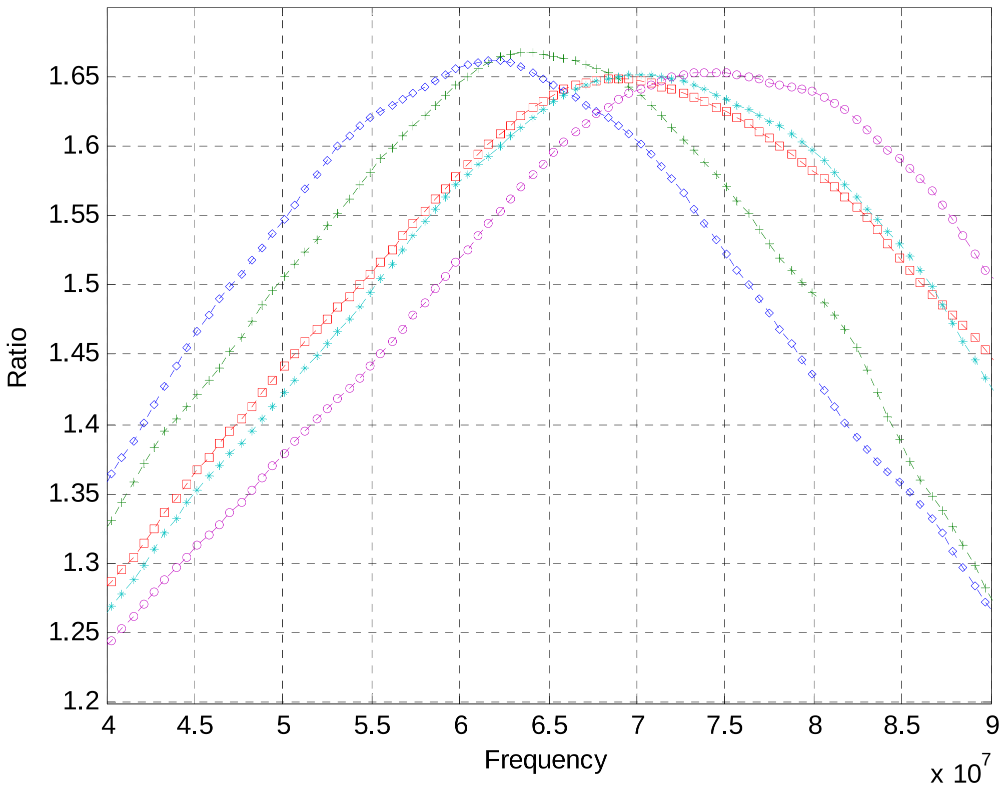

Fig. 4-21: Received signals ratio $\left|\frac{G(f)}{H(f)}\right|$ through substrate with and without thin film peak at different frequencies. (Blue: 20 °C; Green: 50 °C; Red: 80 °C; Light Blue: 110 °C; Purple:140 °C)

The final calculated acoustic properties are listed in Table 4-1. For the film fabricated and cured at room temperature, the ultrasonic velocity is 1953 m/s. This speed increases almost linearly when the annealing temperature increases, it goes up nearly 20% to 2344m/s after the final annealing at 140 ^{o}C.

Density measurements also show the tendency of steady increase with increasing curing temperature. Compared to the theoretical density of 3950 kg/m^3, the density of the porous structure is about 67.4% after the 20 ^{o}C annealing and 77.3 % after the final annealing at 140 ^{o}C.

Table 4-1: Measured acoustic characteristic of TiO_2 nano-structured film after annealing 1 hour at different temperatures.

	Velocity (m/s)	Density (kg/m^3)	Acoustic Impedance (MRayls)
20 ^{o}C	~1953	~2715	5.30
50 ^{o}C	~2031	~2892	5.87
80 ^{o}C	~2207	~2965	6.54
110 ^{o}C	~2221	~3032	6.73
140 ^{o}C	~2344	~3068	7.19

From experimental results, it is found that this new nano-structured TiO_2 material provides adequate acoustic characteristics for matching layer applications. After thermal treatment at elevated temperatures, ethanol is totally evaporated. The whole material achieves higher density and stiffer bonding between the nano-particles. The acoustic impedance of the final product can reach as high as 7.19 MRayls, which is a solid improvement compared to that of the SiO_2 nano-composites, whose maximum acoustic impedance is only 5.7 MRayls.

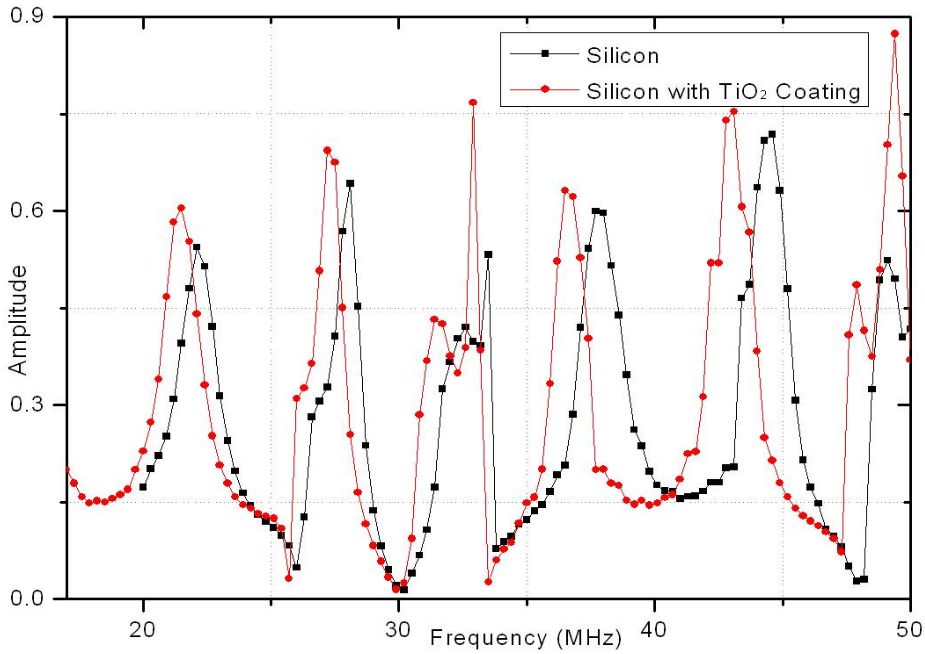

Fig. 4-22: Received through signal spectrum calculated using T-Matrix method.

The obtained signals from experiments using the T-matrix method are presented in Fig. 4-22. We can see a clear phase shift in the spectrum curve in Fig. 4-22 when the thin film is deposited onto the silicon substrate. However, the ability to catch this phase shift and then calculate the acoustic properties largely depends on the precision of the experimental devices.

4.4.3 Simulation and Comparison.

In order to demonstrate the effectiveness of the matching layer made of the new TiO_2 nano-porous film, we have simulated the performance of a 100MHz Lithium Niobate ultrasonic transducer using PiezoCAD, which is a piezoelectric transducer modeling software (Sonic Concepts).

The PiezoCAD software has the ability to calculate multiple input, output and transfer parameters. Those parameters are very useful in designing a wide range of piezoelectric transducers. PiezoCAD uses chain circuit matrix technique to calculate all system characteristics from the front acoustic port to the electric terminals. User can select piezoelectric material from ceramic, crystalline, polymer, and composite materials. Acoustic matching and backing layers parameters, as well as load medium characteristics, can be adjusted by the user. Thickness, velocity, attenuation, and cross-sectional geometry data can be entered for each layer in the transducer structure. PiezoCAD can provide outputs such as acoustic and electric input admittance functions; transmit and receive power conversion efficiencies; transmit, receive, and pulse-echo transfer functions and time domain waveforms, therefore, it is a convenient tool for rapid iterative transducer design optimization.

In our performance comparison simulations, centre frequency of the transducer are set at 100 MHz. Time step is 4096. Transmitter output electrical impedance is 50.0Ohms. All other input parameters are shown in Table 4-2.

Table 4-2: Transducer parameter used in PiezoCAD simulation

	Parameters
Piezoelectric Material	Lithium Niobate Shape: 1.9 mm diameter disk Thickness: 0.033 mm Acoustic Impedance: 34.058 MRayls
New TiO_2 Material	Thickness: 0.00586 mm Acoustic Impedance: 7.19 MRayls
Desilets Model Material	Thickness: 0.0045 mm. Acoustic Impedance: 4.14 MRayls
Parylene	Thickness: 0.00587 mm. Acoustic Impedance: 2.585 MRayls
Backing Material	E-Solder 3022. Acoustic Impedance: 5.9 Mrayls Damping: 110dB/cm

The simulation results are presented in Fig. 4-23. Compared with parylene and SiO_2 nano-composite matching layer design, the power transmit efficiency (output acoustic power/ electrical input power) can be increased by more 100%. There is more than 10 % increase in sensitivity compared with SiO_2 nano-composite matching layer design. The 3 dB bandwidth is almost the same for all cases. Therefore, for a single matching layer design with lossy backing, better matching layer mainly increases the sensitivity

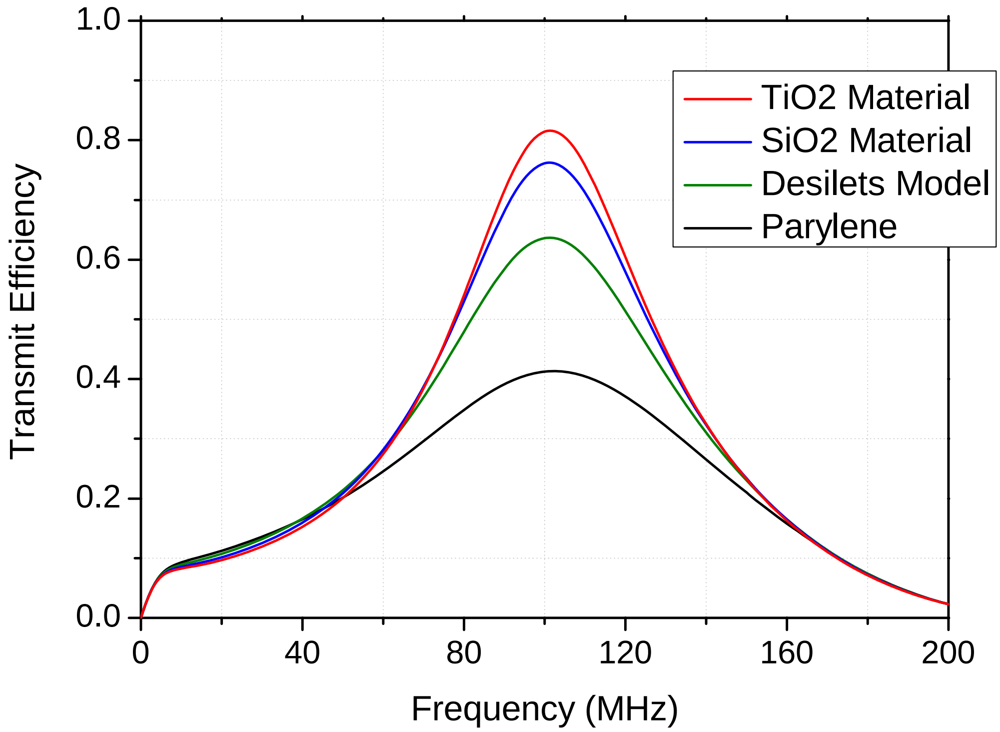

Fig. **4-23**: Power transmission efficiency spectra of a 100 MHz transducer with single matching layer using different materials. The DFK model curve was generated using the acoustic impedance of $Z = Z_c^{1/3} Z_m^{2/3}$.

The paper of DeSilets/Fraser gaves a better value of the acoustic impedance of the matching layer for air backed transducers. If the backing has similar acoustic impedance as the piezoelectric and is very lossy, the geometric mean still gives the best result. From our simulation design using PiezoCAD, a good matching layer mainly improves the sensitivity not the bandwidth. Broader bandwidth needs two or more matching layers. For two matching layers, the acoustic impedance of the first matching layer requires the acoustic impedance is than the geometric mean (~ 8.9 MRayls for air baked PZT transducer based on the calculation of DeSilets/Fraser, it is even higher for lossy backing transducers). Therefore, our new high acoustic impedance material can play a critical role for making such matching layers of ultra-high frequency transducers.

Chapter 5

FINITE DIFFERENCE TIME DOMAIN METHOD

5.1 Introduction

5.1.1 Finite-Difference Concept

The Finite Difference Time Domain method is a numerical technique based on the finite difference concept. This finite difference concept is extremely important in solving Maxwell's equation for the electric and magnetic field distributions in both time and spatial domains. The basic concept of FDTD methods is described briefly below. The increment of a function f(x) from the change of Δx at the point x can be written as:

$$\Delta f(x) = f(x + \Delta x) - f(x) \qquad \text{(Eq 5-1)}$$

and the derivative of the function f(x) with respect to x at x is:

$$f'(x) = \lim_{\Delta x \to 0} \frac{\Delta f(x)}{\Delta x} = \lim_{\Delta x \to 0} \frac{f(x + \Delta x) - f(x)}{\Delta x} \qquad \text{(Eq 5-2)}$$

When the increment Δx is small enough, the derivative of the function f(x) with respect to x can be approximately replaced by its difference quotient:

$$\frac{\partial f}{\partial x} \approx \frac{\Delta f(x)}{\Delta x} \qquad \text{(Eq 5-3)}$$

There are three different ways to express the derivative of f(x), i.e., the forward difference, backward difference and central difference schemes. The definitions of these three differences are:

Forward difference:

$$\left.\frac{\Delta f(x)}{\Delta x}\right|_{x} = \frac{f(x+\Delta x) - f(x)}{\Delta x} \qquad \text{(Eq 5-4)}$$

Backward difference:

$$\left.\frac{\Delta f(x)}{\Delta x}\right|_{x} = \frac{f(x) - f(x-\Delta x)}{\Delta x} \qquad \text{(Eq 5-5)}$$

Central difference:

$$\left.\frac{\Delta f(x)}{\Delta x}\right|_{x} = \frac{f(x+\frac{\Delta x}{2}) - f(x-\frac{\Delta x}{2})}{\Delta x} \qquad \text{(Eq 5-6)}$$

If the $f(x+\Delta x)$ and $f(x-\Delta x)$ are expanded into Taylor series at the x point:

$$f(x+\Delta x) = f(x) + \Delta x\frac{\partial f(x)}{\partial x} + \frac{1}{2!}\Delta x^2\frac{\partial^2 f(x)}{\partial^2 x} + \frac{1}{3!}\Delta x^3\frac{\partial^3 f(x)}{\partial^3 x} \qquad \text{(Eq 5-7)}$$

$$f(x-\Delta x) = f(x) - \Delta x\frac{\partial f(x)}{\partial x} + \frac{1}{2!}\Delta x^2\frac{\partial^2 f(x)}{\partial^2 x} - \frac{1}{3!}\Delta x^3\frac{\partial^3 f(x)}{\partial^3 x} \qquad \text{(Eq 5-8)}$$

Substituting Eq 5-8 and Eq 5-9 into Eq 5-5, Eq 5-6 and Eq 5-7, the three differences will be expressed in the forms below:

Forward difference:

$$\left.\frac{\Delta f(x)}{\Delta x}\right|_{x} = \frac{\partial f(x)}{\partial x} + \frac{1}{2!}\Delta x\frac{\partial^2 f(x)}{\partial^2 x} + \frac{1}{3!}\Delta x^2\frac{\partial^3 f(x)}{\partial^3 x} \qquad \text{(Eq 5-9)}$$

Backward difference:

$$\left.\frac{\Delta f(x)}{\Delta x}\right|_x = \frac{\partial f(x)}{\partial x} - \frac{1}{2!}\Delta x \frac{\partial^2 f(x)}{\partial^2 x} + \frac{1}{3!}\Delta x^2 \frac{\partial^3 f(x)}{\partial^3 x} \qquad \text{(Eq 5-10)}$$

Central difference:

$$\left.\frac{\Delta f(x)}{\Delta x}\right|_x = \frac{\partial f(x)}{\partial x} + \frac{1}{4}\frac{1}{3!}\Delta x^2 \frac{\partial^3 f(x)}{\partial^3 x} \qquad \text{(Eq 5-11)}$$

From the derivation results, it is conclusive that the forward difference and the backward difference are first-order accurate while the central difference is second-order accurate. When deciding on which difference should be used, the choice will need to be made based on the requirements of the practical applications. The difference approximation formulas for the first and second Derivatives have been introduced in Table **5-1**.

Table **5-1**: The Difference Approximation Formulas for the First and Second Derivatives.

Table **5-1**

Forward difference approximation for the first derivative: $$D_{f1}(x,t)=\frac{f_1-f_0}{t}$$
More accurate forward difference approximation for the first derivative: $$D_{f2}(x,t)=\frac{2D_{f1}(x,t)-D_{f1}(x,2t)}{2-1}=\frac{-f_2+4f_1-3f_0}{2t}$$
Backward difference approximation for the first derivative: $$D_{b1}(x,t)=\frac{f_0-f_{-1}}{t}$$
More accurate backward difference approximation for the first derivative: $$D_{b2}(x,t)=\frac{2D_{b1}(x,t)-D_{b1}(x,2t)}{2-1}=\frac{-f_0+4f_{-1}-3f_{-2}}{2t}$$
Central difference approximation for the first derivative: $$D_{c2}(x,t)=\frac{f_1-f_{-1}}{2t}$$
More accurate central difference approximation for the first derivative: $$D_{c4}(x,t)=\frac{4D_{c2}(x,t)-D_{c2}(x,2t)}{4-1}=\frac{-f_2+8f_1-8f_{-1}+f_{-2}}{12t}$$
Central difference approximation for the second derivative: $$D_{c2}^{(2)}(x,t)=\frac{f_1-2f_0+f_{-1}}{t^2}$$
More accurate central difference approximation for the second derivative: $$D_{c4}^{(2)}(x,t)=\frac{4D_{c2}^{(2)}(x,t)-D_{c2}^{(2)}(x,2t)}{4-1}=\frac{-f_2+16f_1-30f_0+16f_{-1}-f_{-2}}{12t^2}$$

5.1.2 Principle of FDTD

As an important subject in the study of electromagnetic fields and microwave propagations, computational electromagnetic has played an important role in many scientific research and engineering applications. There are several commonly used methods in computational electromagnetic, such as the finite element method (FEM), finite difference time domain (FDTD) method, and the method of moments (MoM). All these methods have their strongpoint and shortcoming, which approach is better depends on the problem at hand.

In a seminal paper published on the 1966 IEEE Transactions on Antennas and Propagation, Dr. Kane Yee first provided the original FDTD space grid and time-stepping algorithm [Yee 1966]. In 1980, Dr. Allen Taflove proposed the term "Finite-difference time-domain" and corresponding "FDTD" in an IEEE Transactions on Electromagnetic Compatibility paper. [Taflove 1080]

Since 1990, the finite-difference time-domain (FDTD) technique has become one of the most popular computational electrodynamics modeling technique dealing with many scientific and engineering problems of electromagnetic wave interactions with material structures, which in part was triggered by the rapid development of computer technology [Abd-El-Raouf 2006]. Current applications employing FDTD modeling technique include:

- Low frequency geophysics involving the entire Earth-ionosphere waveguide [Cummer 2000].

- Microwaves: radar and antennas technology, wireless communications, digital interconnects, biomedical imaging and devices [Andrew, et al. 1994].
- Phonics: photonic crystals, nano-plasmatic and bio-photonics [Zhou, et al. 2006].

Software programming of the FDTD method can be implemented without difficulties. Because the solution is in time-domain, we can get the solutions of a wide frequency range in a single simulation execution via FFT.

The FDTD technique belongs to grid-based differential time-domain modeling. In solving the Maxwell equations, it utilizes the finite difference technique to discretize the Faraday's law and Ampere's law of Maxwell's curl equations in time and space domains.

Faraday's Law

$$\nabla \mathrm{x}\,\vec{E} = -\mu \frac{\partial \vec{H}}{\partial t} - \sigma_M \vec{H} \qquad \text{(Eq 5-12)}$$

Ampere's Law

$$\nabla \mathrm{x}\,\vec{H} = \varepsilon \frac{\partial \vec{E}}{\partial t} + \sigma \vec{E} \qquad \text{(Eq 5-13)}$$

The resulting equations are then solved numerically by programs using a explicit leapfrog scheme in a volume of space: the electric field vector components are solved at a given time t; then the magnetic field vector components will be solved at $t + \Delta t$. This process will be repeated over and over again until the final steady state is fully achieved. The schematic of Yee's scheme is shown in Fig. **5-1:**

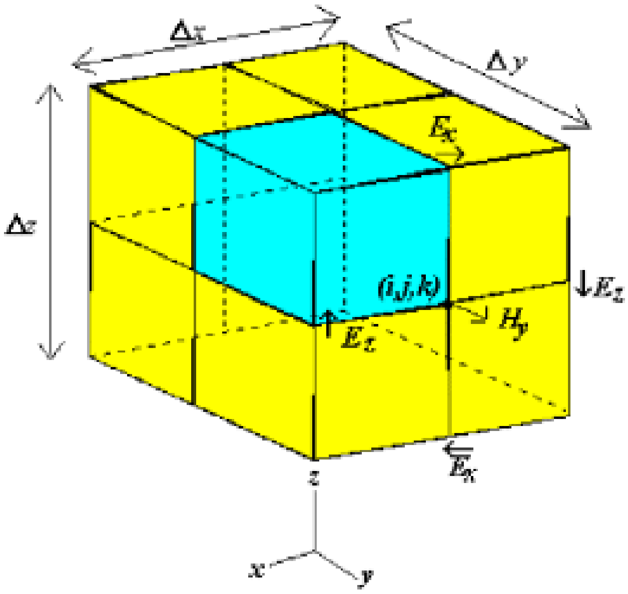

Fig. 5-1: Schematic of Yee's scheme [Yee 1966].

We now rewrite Eq 5-13 and Eq 5-14 in a Cartesian coordinate system:

$$\frac{\partial H_x}{\partial t} = \frac{1}{\mu_x}\left(\frac{\partial E_y}{\partial z} - \frac{\partial E_z}{\partial y} - \sigma_{Mx} H_x\right) \qquad \text{(Eq 5-14)}$$

$$\frac{\partial H_y}{\partial t} = \frac{1}{\mu_y}\left(\frac{\partial E_z}{\partial x} - \frac{\partial E_x}{\partial z} - \sigma_{My} H_y\right) \qquad \text{(Eq 5-15)}$$

$$\frac{\partial H_z}{\partial t} = \frac{1}{\mu_z}\left(\frac{\partial E_z}{\partial y} - \frac{\partial E_y}{\partial x} - \sigma_{Mz} H_z\right) \qquad \text{(Eq 5-16)}$$

$$\frac{\partial E_x}{\partial t} = \frac{1}{\varepsilon_x}\left(\frac{\partial H_z}{\partial y} - \frac{\partial H_y}{\partial z} - \sigma_x E_x\right) \qquad \text{(Eq 5-17)}$$

$$\frac{\partial E_y}{\partial t} = \frac{1}{\varepsilon_y}\left(\frac{\partial H_x}{\partial z} - \frac{\partial H_z}{\partial x} - \sigma_y E_y\right) \qquad \text{(Eq 5-18)}$$

$$\frac{\partial E_z}{\partial t} = \frac{1}{\varepsilon_z}\left(\frac{\partial H_y}{\partial x} - \frac{\partial H_x}{\partial y} - \sigma_z E_z\right) \qquad \text{(Eq 5-19)}$$

ε, σ and μ are the material's electric and magnetic properties. It is known that electric and magnetic fields in time and space domains can also be denoted in conventional notations:

$$E_x^n(i+\frac{1}{2}, j, k) = E_x((i+\frac{1}{2})\Delta x, j\Delta y, k\Delta z, n\Delta t) \qquad \text{(Eq 5-20)}$$

$$E_y^n(i, j+\frac{1}{2}, k) = E_x(i\Delta x, (j+\frac{1}{2})\Delta y, k\Delta z, n\Delta t) \qquad \text{(Eq 5-21)}$$

$$E_z^n(i, j, k+\frac{1}{2}) = E_z(i\Delta x, j\Delta y, (k+\frac{1}{2})\Delta z, n\Delta t) \qquad \text{(Eq 5-22)}$$

$$H_x^{n+\frac{1}{2}}(i, j+\frac{1}{2}, k+\frac{1}{2}) = H_x(i\Delta x, (j+\frac{1}{2})\Delta y, (k+\frac{1}{2})\Delta z, (n+\frac{1}{2})\Delta t) \qquad \text{(Eq 5-23)}$$

$$H_y^{n+\frac{1}{2}}(i+\frac{1}{2}, j, k+\frac{1}{2}) = H_y((i+\frac{1}{2})\Delta x, j\Delta y, (k+\frac{1}{2})\Delta z, (n+\frac{1}{2})\Delta t) \qquad \text{(Eq 5-24)}$$

$$H_z^{n+\frac{1}{2}}(i+\frac{1}{2},j+\frac{1}{2},k)=H_z((i+\frac{1}{2})\Delta x,(j+\frac{1}{2})\Delta y,k\Delta z,(n+\frac{1}{2})\Delta t) \qquad \text{(Eq 5-25)}$$

By these notations, Eq **5-12** to Eq **5-19** can be finally represented by:

$$H_x^{n+\frac{1}{2}}(i,j+\frac{1}{2},k+\frac{1}{2})=\frac{\mu_x-\frac{1}{2}\Delta t\sigma_{Mx}}{\mu_x+\frac{1}{2}\Delta t\sigma_{Mx}}H_x^{n-\frac{1}{2}}(i,j+\frac{1}{2},k+\frac{1}{2})$$
$$+\frac{\Delta t}{\mu_x+\frac{1}{2}\Delta t\sigma_{Mx}}\left(\begin{array}{c}\dfrac{E_y^n(i,j+\frac{1}{2},k+1)-E_y^n(i,j+\frac{1}{2},k)}{\Delta z}-\\ \dfrac{E_z^n(i,j+1,k+\frac{1}{2})-E_z^n(i,j,k+\frac{1}{2})}{\Delta y}\end{array}\right) \qquad \text{(Eq 5-26)}$$

$$H_y^{n+\frac{1}{2}}(i+\frac{1}{2},j,k+\frac{1}{2})=\frac{\mu_y-\frac{1}{2}\Delta t\sigma_{My}}{\mu_y+\frac{1}{2}\Delta t\sigma_{My}}H_y^{n-\frac{1}{2}}(i+\frac{1}{2},j,k+\frac{1}{2})$$
$$+\frac{\Delta t}{\mu_y+\frac{1}{2}\Delta t\sigma_{My}}\left(\begin{array}{c}\dfrac{E_z^n(i+1,j,k+\frac{1}{2})-E_z^n(i,j,k+\frac{1}{2})}{\Delta x}-\\ \dfrac{E_x^n(i+\frac{1}{2},j,k+1)-E_x^n(i+\frac{1}{2},j,k)}{\Delta z}\end{array}\right) \qquad \text{(Eq 5-27)}$$

$$H_z^{n+\frac{1}{2}}(i+\frac{1}{2},j+\frac{1}{2},k)=\frac{\mu_z-\frac{1}{2}\Delta t\sigma_{Mz}}{\mu_z+\frac{1}{2}\Delta t\sigma_{Mz}}H_z^{n-\frac{1}{2}}(i+\frac{1}{2},j+\frac{1}{2},k)+\frac{\Delta t}{\mu_z+\frac{1}{2}\Delta t\sigma_{Mz}}\left(\frac{E_x^n(i+\frac{1}{2},j+1,k)-E_x^n(i+\frac{1}{2},j,k)}{\Delta y}-\frac{E_y^n(i+1,j+\frac{1}{2},k)-E_y^n(i,j+\frac{1}{2},k)}{\Delta x}\right)$$ (Eq 5-28)

$$E_x^{n+1}(i+\frac{1}{2},j,k)=\frac{\varepsilon_x-\frac{1}{2}\Delta t\sigma_x}{\varepsilon_x+\frac{1}{2}\Delta t\sigma_x}E_x^n(i+\frac{1}{2},j,k)+\frac{\Delta t}{\varepsilon_x+\frac{1}{2}\Delta t\sigma_x}\left(\frac{H_z^{n+\frac{1}{2}}(i+\frac{1}{2},j+\frac{1}{2},k)-H_z^{n+\frac{1}{2}}(i+\frac{1}{2},j-\frac{1}{2},k)}{\Delta y}-\frac{H_y^{n+\frac{1}{2}}(i+\frac{1}{2},j,k+\frac{1}{2})-H_y^{n+\frac{1}{2}}(i+\frac{1}{2},j,k-\frac{1}{2})}{\Delta z}\right)$$ (Eq 5-29)

$$E_y^{n+1}(i,j+\frac{1}{2},k)=\frac{\varepsilon_y-\frac{1}{2}\Delta t\sigma_y}{\varepsilon_y+\frac{1}{2}\Delta t\sigma_y}E_y^n(i,j+\frac{1}{2},k)+\frac{\Delta t}{\varepsilon_y+\frac{1}{2}\Delta t\sigma_y}\left(\frac{H_x^{n+\frac{1}{2}}(i,j+\frac{1}{2},k+\frac{1}{2})-H_x^{n+\frac{1}{2}}(i,j+\frac{1}{2},k-\frac{1}{2})}{\Delta z}-\frac{H_z^{n+\frac{1}{2}}(i+\frac{1}{2},j+\frac{1}{2},k)-H_z^{n+\frac{1}{2}}(i-\frac{1}{2},j+\frac{1}{2},k)}{\Delta x}\right)$$ (Eq 5-30)

$$E_z^{n+1}(i,j,k+\frac{1}{2}) = \frac{\varepsilon_z - \frac{1}{2}\Delta t\sigma_z}{\varepsilon_z + \frac{1}{2}\Delta t\sigma_z} E_z^{n}(i,j,k+\frac{1}{2})$$

$$+\frac{\Delta t}{\varepsilon_y + \frac{1}{2}\Delta t\sigma_y}\left(\frac{H_y^{n+\frac{1}{2}}(i+\frac{1}{2},j,k+\frac{1}{2}) - H_y^{n+\frac{1}{2}}(i-\frac{1}{2},j,k+\frac{1}{2})}{\Delta x} - \frac{H_x^{n+\frac{1}{2}}(i,j+\frac{1}{2},k+\frac{1}{2}) - H_x^{n+\frac{1}{2}}(i,j-\frac{1}{2},k+\frac{1}{2})}{\Delta y} \right) \quad \text{(Eq 5-31)}$$

5.1.3 Advantage and Disadvantage

Same as every other technique in computational electromagnetic field, FDTD method has its own strongpoints and drawbacks.The FDTD method is an intuitionistic and versatile technique. People should have no difficulties in understanding the basic principle and using it in practical scenarios to get satisfying results. FDTD is good at analyzing problems related to Maxwell's equations and similar partial differential equations with complex geometrical characteristics and arbitrarily inhomogeneous properties. Users can specify and change the material properties at any computational domain point to create and modify a great variety of linear and nonlinear piezoelectric and magnetic material models [Shlager, Schneider 1995].

FDTD method directly uses output parameters in the calculation so that no data conversion process is needed to get the final results [Taflove, et al. 2000]. Unlike MoM and FEM, There is no requirement of the derivation of a Green's function of the matrix equation solution in FDTD method. Therefore, the effects of apertures and shielding of a lot of electromgnetic problems are allowed to be solved directly.

As a time-domain technique, a single FDTD method simulation can solve the equation with several different frequencies and provide the frequency response simultaneously. So users can use a broadband pulse containing multiple frequency components as the exciting source, which is very helpful when users encounter application problems invovling complex pulse signal processing.

However, when applying the FDTD technique, the entire computational domain should be meshed, not just the target area. The temporal discretization grid should be small enough so that the recurrent leap frog equation is solvable, the spatial discretization grid must be subtle enough to deal with both the smallest electromagnetic wavelength and geometrical shape change in the domain. All those requirements place a relatively heavy burden on computer hardware resources when simulating a very complex problem that includes very large computational domain or frequent property change. For example, a simulation involving spatial dimensions on the order of 10 wavelengths will require GHz level central processing unit with 2 or more gigabytes memory. A very long processing time should also be anticipated in the FDTD simulation. Parallel processing may speed up the calculation process but it is still time-consuming. Also needs to be mentioned is that long and thin geometry models may be difficult to be anlyzed using FDTD method because of the requirement of excessively large computational domain.

5.2 Using FDTD to Solve Acoustic Wave Propagation

5.2.1 Derivation of One Dimensional Wave Equation

The one dimensional wave equation can be derived by Newton's equations of motion and the Hooke's law.

Fig. 5-2

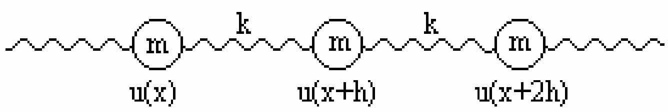

Fig. 5-2: Mass arrays linked with springs

In a system shown in Fig. 5-2, several masses are connected with long springs of length h, the spring stiffness is k. Based on Newton's equations of motion and the Hooke's law::

$$F_N = ma = m \cdot \frac{\partial^2}{\partial t^2} u(x+h,t) \qquad \text{(Eq 5-32)}$$

$$\begin{aligned} F_H &= F_{(x+2h)} + F_x \\ &= k(u(x+2h,t) - u(x+h,t)) + k(u(x,t) - u(x+h,t)) \end{aligned} \qquad \text{(Eq 5-33)}$$

The values of these two forces at x+h lead to:

$$\begin{aligned} & m \cdot \frac{\partial^2}{\partial t^2} u(x+h,t) = \\ & k(u(x+2h,t) - u(x+h,t) + u(x,t) - u(x+h,t)) \end{aligned} \qquad \text{(Eq 5-34)}$$

If the array consists of N masses, then the length of the array L is Nh, the weight M is Nm, and the total stiffness K is k/N, so that Eq 5-34 will be expressed as:

$$\frac{\partial^2}{\partial t^2}u(x+h,t)=\frac{KL^2}{M}(u(x+2h,t)-2u(x+h,t)+u(x,t)) \qquad \text{(Eq 5-35)}$$

When N approaches infinity and h approaches 0, Eq 5-35 changes to:

$$\frac{\partial^2}{\partial t^2}u(x,t)=\frac{KL^2}{M}\frac{\partial^2}{\partial x^2}u(x,t)=c^2\frac{\partial^2}{\partial x^2}u(x,t) \qquad \text{(Eq 5-36)}$$

Where c denotes the material's sound speed:

$$c=\sqrt{\frac{K}{\rho}} \qquad \text{(Eq 5-37)}$$

K is the stiffness coefficient and ρ is material density.

5.2.2 FDTD Numerical Method for Elastic Wave Equations

Assume that we have a sound wave represented by $u = A\cos(\omega t - kx + \phi_0)$, where ϕ_0 is the phase at t=0 and x=0. Now we apply the FDTD method:

$$\begin{aligned}\frac{\partial^2}{\partial t^2}u(x,t)&=\frac{\frac{\partial}{\partial t}u(x_i,t_{j+1})-\frac{\partial}{\partial t}u(x_i,t_j)}{\Delta t}\\&=\frac{\frac{u(x_i,t_{j+1})-u(x_i,t_j)}{\Delta t}-\frac{u(x_i,t_j)-u(x_i,t_{j-1})}{\Delta t}}{\Delta t}\\&=\frac{u(x_i,t_{j+1})-2u(x_i,t_j)+u(x_i,t_{j-1})}{(\Delta t)^2}\end{aligned} \qquad \text{(Eq 5-38)}$$

$$\frac{\partial^2}{\partial x^2}u(x,t) = \frac{\frac{\partial}{\partial t}u(x_{i+1},t_j) - \frac{\partial}{\partial t}u(x_i,t_j)}{\Delta x}$$

$$= \frac{\frac{u(x_{i+1},t_j) - u(x_i,t_j)}{\Delta x} - \frac{u(x_i,t_j) - u(x_{i-1},t_j)}{\Delta x}}{\Delta x} \qquad \text{(Eq 5-39)}$$

$$= \frac{u(x_{i+1},t_j) - 2u(x_i,t_j) + u(x_{i-1},t_j)}{(\Delta x)^2}$$

Substitute Eq 5-38 and Eq 5-39 into one dimensional wave equation and we get the equation for leapfrog process:

$$\frac{u(x_i,t_{j+1}) - 2u(x_i,t_j) + u(x_i,t_{j-1})}{(\Delta t)^2} =$$

$$c^2 \frac{u(x_{i+1},t_j) - 2u(x_i,t_j) + u(x_{i-1},t_j)}{(\Delta x)^2}$$

$$\Rightarrow$$

$$u(x_i,t_{j+1}) - 2u(x_i,t_j) + u(x_i,t_{j-1}) =$$

$$(\frac{c\Delta t}{\Delta x})^2 (u(x_{i+1},t_j) - 2u(x_i,t_j) + u(x_{i-1},t_j)) \qquad \text{(Eq 5-40)}$$

$$\Rightarrow$$

$$u(x_i,t_{j+1}) =$$

$$2(1 - (\frac{c\Delta t}{\Delta x})^2)u(x_i,t_j) + (\frac{c\Delta t}{\Delta x})^2 (u(x_{i+1},t_j) + u(x_{i-1},t_j)) - u(x_i,t_{j-1})$$

In acoustic wave propagation problems, there may be more than just one medium in the simulation domain. When wave travels from one medium to another medium, transmission and reflection happen at the interface. To deal with this situation, Eq 5-41 needs to be adjusted to reflect the material properties change.

Suppose point x_i is within medium 1 and x_{i+1} is within medium 2, then after similar analysis in last section, we can get the equation of $u(x_i, t_{i+1})$ and $u(x_{i+1}, t_{i+1})$:

$$\begin{aligned}&u(x_i, t_{j+1}) = \\ &2(1-(\frac{\rho_1 c_1 \Delta t}{\Delta x})^2)u(x_i, t_j) + (\frac{\rho_2 c_2 \Delta t}{\Delta x})^2 u(x_{i+1}, t_j) \\ &+(\frac{\rho_1 c_1 \Delta t}{\Delta x})^2 u(x_{i-1}, t_j) - u(x_i, t_{j-1})\end{aligned} \quad \text{(Eq 5-41)}$$

$$\begin{aligned}&u(x_{i+1}, t_{j+1}) = \\ &2(1-(\frac{\rho_2 c_2 \Delta t}{\Delta x})^2)u(x_{i+1}, t_j) + (\frac{\rho_1 c_1 \Delta t}{\Delta x})^2 u(x_{i+2}, t_j) \\ &+(\frac{\rho_2 c_2 \Delta t}{\Delta x})^2 u(x_i, t_j) - u(x_{i+1}, t_{j-1})\end{aligned} \quad \text{(Eq 5-42)}$$

To increase the accuracy of the calculation, we can also involve more points in this process by setting:

$$D_{c4}{}^{(2)}(x,t) = \frac{-f_2 + 16f_1 - 30f_0 + 16f_{-1} - f_{-2}}{12t^2} \quad \text{(Eq 5-43)}$$

Now we can get the more accurate FDTD equation for simulation:

$$\frac{u(x_i,t_{j+1})-2u(x_i,t_j)+u(x_i,t_{j-1})}{(\Delta t)^2}=$$
$$c^2\frac{-u(x_{i+2},t_j)+16u(x_{i+1},t_j)-30u(x_i,t_j)+16u(x_{i-1},t_j)-u(x_{i-2},t_j)}{12(\Delta x)^2}$$
$$\Rightarrow$$
$$u(x_i,t_{j+1})-2u(x_i,t_j)+u(x_i,t_{j-1})=$$
$$\frac{1}{12}(\frac{c\Delta t}{\Delta x})^2(-u(x_{i+2},t_j)+16u(x_{i+1},t_j)-30u(x_i,t_j)$$
$$+16u(x_{i-1},t_j)-u(x_{i-2},t_j))$$

$$\Rightarrow \qquad \text{(Eq 5-44)}$$
$$u(x_i,t_{j+1})=2u(x_i,t_j)-u(x_i,t_{j-1})+$$
$$\frac{1}{12}(\frac{c\Delta t}{\Delta x})^2(-u(x_{i+2},t_j)+16u(x_{i+1},t_j)-30u(x_i,t_j)$$
$$+16u(x_{i-1},t_j)-u(x_{i-2},t_j))$$

$$\Rightarrow$$
$$u(x_i,t_{j+1})=2(1-\frac{5}{4}(\frac{c\Delta t}{\Delta x})^2)u(x_i,t_j)-u(x_i,t_{j-1})+$$
$$\frac{1}{12}(\frac{c\Delta t}{\Delta x})^2(-u(x_{i+2},t_j)+16u(x_{i+1},t_j)+16u(x_{i-1},t_j)-u(x_{i-2},t_j))$$

If damping is considered in the wave propagation, the wave equation will need to be expressed as:

$$\frac{\partial^2 u}{\partial t^2}+c^2\gamma\frac{\partial u}{\partial t}-c^2\frac{\partial^2 u}{\partial x^2}=0 \qquad \text{(Eq 5-45)}$$

γ is the damping coefficient. This equation can be solved analytically for an homogeneous medium to get $u(x,t)=A_0e^{-\frac{\gamma}{2}t}\cos(\omega_0 t-kx+\phi_0)$. By using the similar technique above, we can also get the FDTD equation for damped wave, which can handle the case of inhomogeneous medium.

$$\frac{u(x_i,t_{j+1})-2u(x_i,t_j)+u(x_i,t_{j-1})}{(\Delta t)^2}+c^2\gamma\frac{u(x_i,t_{j+1})-u(x_i,t_{j-1})}{2*\Delta t}$$

$$-c^2\frac{u(x_{i+1},t_j)-2u(x_i,t_j)+u(x_{i-1},t_j)}{(\Delta x)^2}=0$$

$$\Rightarrow$$

$$2u(x_i,t_{j+1})-4u(x_i,t_j)+2u(x_i,t_{j-1})+c^2\gamma\Delta t u(x_i,t_{j+1})$$

$$-c^2\gamma\Delta t u(x_i,t_{j-1})-2(\frac{c\Delta t}{\Delta x})^2(u(x_{i+1},t_j)-2u(x_i,t_j)+u(x_{i-1},t_j))$$

$$=0$$

$$\Rightarrow$$

$$(2+c^2\gamma\Delta t)u(x_i,t_{j+1})=4(1-(\frac{c\Delta t}{\Delta x})^2)u(x_i,t_j)+$$

$$2(\frac{c\Delta t}{\Delta x})^2(u(x_{i+1},t_j)+u(x_{i-1},t_j))-(2-c^2\gamma\Delta t)u(x_i,t_{j-1})$$

(Eq **5-46**)

$$\Rightarrow$$

$$u(x_i,t_{j+1})=$$

$$\frac{4(1-(\frac{c\Delta t}{\Delta x})^2)u(x_i,t_j)+2(\frac{c\Delta t}{\Delta x})^2(u(x_{i+1},t_j)}{(2+c^2\gamma\Delta t)}+$$

$$\frac{u(x_{i-1},t_j))-(2-c^2\gamma\Delta t)u(x_i,t_{j-1})}{(2+c^2\gamma\Delta t)}$$

If there is a driving force with several different frequency components, we can solve the problem for each component and then use superposition principle to get all the solutions for a linear system. The wave equation with a sinusoidal driving force is:

$$\frac{\partial^2 u}{\partial t^2}+c^2\gamma\frac{\partial u}{\partial t}-c^2\frac{\partial^2 u}{\partial x^2}=A\cos(\omega t+\phi)f(x) \qquad \text{(Eq 5-47)}$$

And the FDTD solution equation is:

$$\frac{u(x_i,t_{j+1})-2u(x_i,t_j)+u(x_i,t_{j-1})}{(\Delta t)^2}+c^2\gamma\frac{u(x_i,t_{j+1})-u(x_i,t_{j-1})}{2*\Delta t}$$
$$-c^2\frac{u(x_{i+1},t_j)-2u(x_i,t_j)+u(x_{i-1},t_j)}{(\Delta x)^2}=f(x)\cos(\omega t+\phi)$$
$$\Rightarrow \qquad \text{(Eq 5-48)}$$
$$u(x_i,t_{j+1})=2u(x_i,t_j)-u(x_i,t_{j-1})-c^2\gamma\Delta t(u(x_i,t_j)-u(x_i,t_{j-1}))$$
$$+(\frac{c\Delta t}{\Delta x})^2(u(x_{i+1},t_j)-2u(x_i,t_j)+u(x_{i-1},t_j))+f(x)\cos(\omega t+\phi)$$

5.2.3 Initial Value Problem.

FDTD method is a time-domain technique, all the results at time step t_{i+1}, $u(t_{i+1})$ are derived from the calculations on the information at $u(t_i)$ and $u(t_{i-1})$ and eventually traced back to $u(t_1)$ and $u(t_0)$. Therefore it is extremely important for us to get the correct initial conditions and then start the simulation. Any tiny mistake at the initial value may cause huge deviation from the correct answer.

To get the initial conditions of acoustic wave propagation at $t=0$, we assume that the x_i components of the displacement and velocity of an unbound elastic material are expressed as:

$$u(x_i,t_0)=f_1(x_i) \qquad \text{(Eq 5-49)}$$

$$\frac{\partial u(x_i, t_0)}{\partial t} = f_2(x_i) \qquad \text{(Eq 5-50)}$$

From Eq 5-50, the relation between $u(t_{-1})$ and $u(t_1)$ can be derived as:

$$\begin{aligned}
&\frac{\partial u(x_i, t_0)}{\partial t} = f_2(x_i) \\
&\Rightarrow \frac{u(x_i, t_1) - u(x_i, t_{-1})}{2\Delta t} = f_2(x_i) \\
&\Rightarrow u(x_i, t_{-1}) = u(x_i, t_1) - 2\Delta t f_2(x_i)
\end{aligned} \qquad \text{(Eq 5-51)}$$

Substitute Eq 5-51 Eq 5-40, $u(x_i, t_1)$ can be derived:

$$\begin{aligned}
&u(x_i, t_1) = 2(1 - (\frac{c\Delta t}{\Delta x})^2)u(x_i, t_0) + \\
&(\frac{c\Delta t}{\Delta x})^2 (u(x_{i+1}, t_0) + u(x_{i-1}, t_0)) - u(x_i, t_1) + 2\Delta t f_2(x) \\
&\Rightarrow \\
&u(x_i, t_1) = (1 - (\frac{c\Delta t}{\Delta x})^2)u(x_i, t_0) + \\
&\frac{1}{2}(\frac{c\Delta t}{\Delta x})^2 (u(x_{i+1}, t_0) + u(x_{i-1}, t_0)) + \Delta t f_2(x) \\
&\Rightarrow \\
&u(x_i, t_1) = (1 - (\frac{c\Delta t}{\Delta x})^2) f_1(x_i) + \\
&\frac{1}{2}(\frac{c\Delta t}{\Delta x})^2 (f_1(x_{i+1}) + f_1(x_{i-1})) + \Delta t f_2(x_i)
\end{aligned} \qquad \text{(Eq 5-52)}$$

After inputting $u(x_i, t_0)$ and $u(x_i, t_1)$, leapfrog Eq 5-41 or Eq 5-45 is utilized for further calculations in time and spatial domains.

5.2.4 Mur's Boundary Condition.

The boundary conditions also play a critical role in FDTD simulations. There are two kinds of boundary conditions presented in the FDTD modeling. The first is between two different media, which has been talked about in the previous section. The other is the outer boundary condition for the whole simulation domain. When a model is built for problem solving, those boundary conditions are used to truncate the computational domain. So without setting the boundary conditions, FDTD method can not be really used to solve practical problems. As shown in Fig. 5-3, the algorithm will keep on running without reaching an end if a boundary isn't set for x_i.

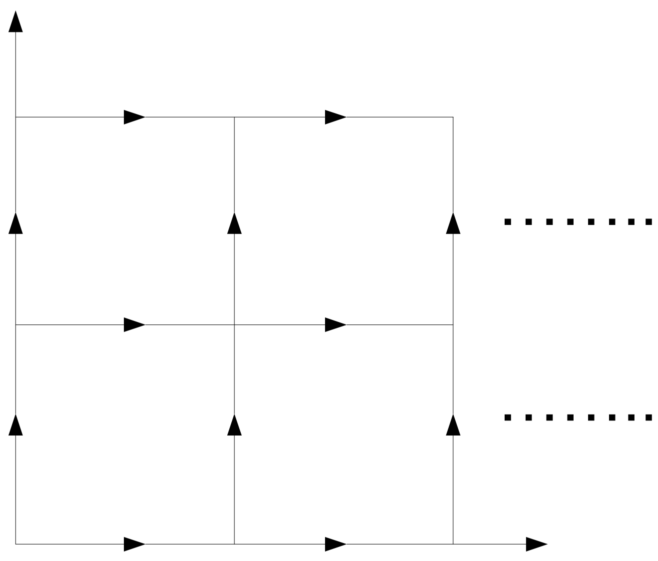

Fig. 5-3: FDTD method keeps on running without setting boundary for x_i.

Boundary condtion has direct influence on final results. For acoustic wave transmission, setting improper boudary condtions may cause extra reflection wave to disturb the normal wave form. So users must take great care to minimize errors introduced by those boundaries. There has been several very effective absorbing boundary conditions (ABCs) available for infinite unbounded computational domain simulation [Luk, et al. 2003]. In our simulation, we have chosen Mur's absorbing boudary condtion in pratical application [Mur 1981].

Mur's absorbing boudary condtion is an effective method with several advantages, acheieving a good result without paying heavy price of simulation time and memory consumption. It can be regarded as an approximation of the Engquist Majda conditon [Engquist, Majda 1977] and is perfectly matched for the wave guides FDTD analysis.

Suppose that there is a plane wave traveling along the x dimension as shown in Fig. 5-4. The displacement $u(x,t)$ at x point and time t satisfies the wave equation $\frac{\partial^2}{\partial t^2}u(x,t) - c^2\frac{\partial^2}{\partial x^2}u(x,t) = 0$.

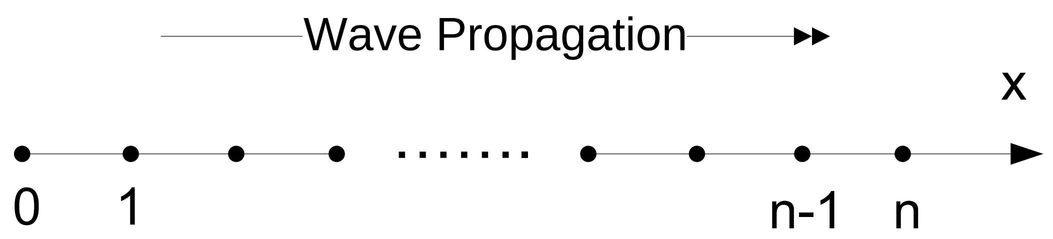

Fig. 5-4: Wave Propagation through x dimension.

Displacement $u(x_i, t)$ at a point x_i inside the domain can be calculated by Eq 5-40 or Eq 5-43. However, $u(x, t)$ at the boundary point x_n can not be solved by those equations because there is no point x_{n+1}. Therefore, forward difference approach is used under such situation to estimate $u(x, t)$ in the time and space dimension. If time is set at $t = (m+1)\Delta t$, the space point is set at x_n, then the displacement $u(x_n, t)$ can be expressed as:

$$u(x_n, (m+1)\Delta t) = (1 - (\frac{c\Delta t}{\Delta x})^2 u(x_n, m\Delta t)) + (\frac{c\Delta t}{\Delta x})^2 u(x_{n-1}, m\Delta t) \qquad \text{(Eq 5-53)}$$

With Eq 5-53, the displacement at a boundary point can be decided by the values of the boundary point and its neighbor point at the previous time step. If we use central difference approach, the FDTD equation can be written as:

$$\begin{aligned}&(\frac{1}{\Delta x})^2 (u(x_{n-1}, (m+\frac{1}{2})\Delta t) - u(x_n, (m+\frac{1}{2})\Delta t) \\ &= (\frac{1}{c\Delta t})^2 (u(x_{n-\frac{1}{2}}, (m+1)\Delta t) - u(x_{n-\frac{1}{2}}, m\Delta t))\end{aligned} \qquad \text{(Eq 5-54)}$$

This equation is second-order accurate. Then we calculate the $u(x_{n-\frac{1}{2}}, t)$ and $u(x, (m+\frac{1}{2})\Delta t)$ by averaging the displacement values of the two adjacent points in the time and space domains:

$$u(x_n, (m+\frac{1}{2})\Delta t) = \frac{1}{2}(u(x_n, (m+1)\Delta t) + u(x_n, m\Delta t)) \qquad \text{(Eq 5-55)}$$

$$u(x_{n-\frac{1}{2}}, m\Delta t) = \frac{1}{2}(u(x_{n-1}, m\Delta t) + u(x_n, m\Delta t)) \qquad \text{(Eq 5-56)}$$

Substituting those two equations into Eq **5-54**, we can get the equation to calculate the displacement of boundary points:

$$u(x_n,(m+1)\Delta t) = u(x_{n-1}, m\Delta t) + \frac{(c\Delta t)^2 - \Delta x^2}{(c\Delta t)^2 + \Delta x^2}(u(x_{n-1},(m+1)\Delta t) - u(x_n, m\Delta t)) \quad \text{(Eq 5-57)}$$

The simulation results with and without absorbing boundaries are shown in Fig. **5-5** and Fig. **5-6**.

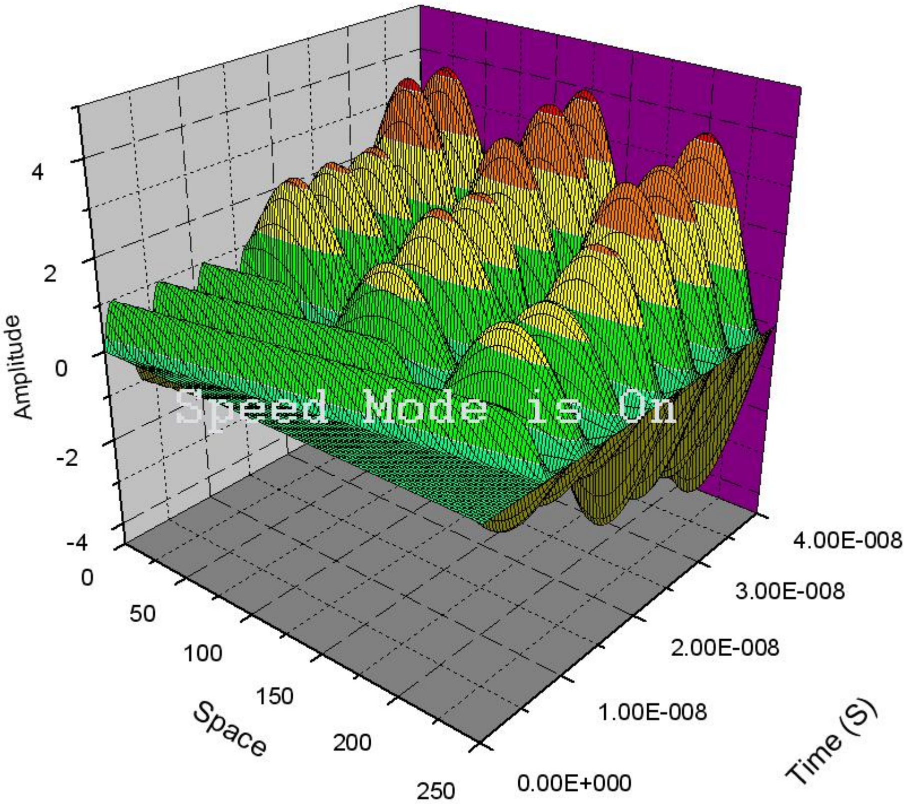

Fig. **5-5**: Simulation results of appling fixed boundary.conditions.

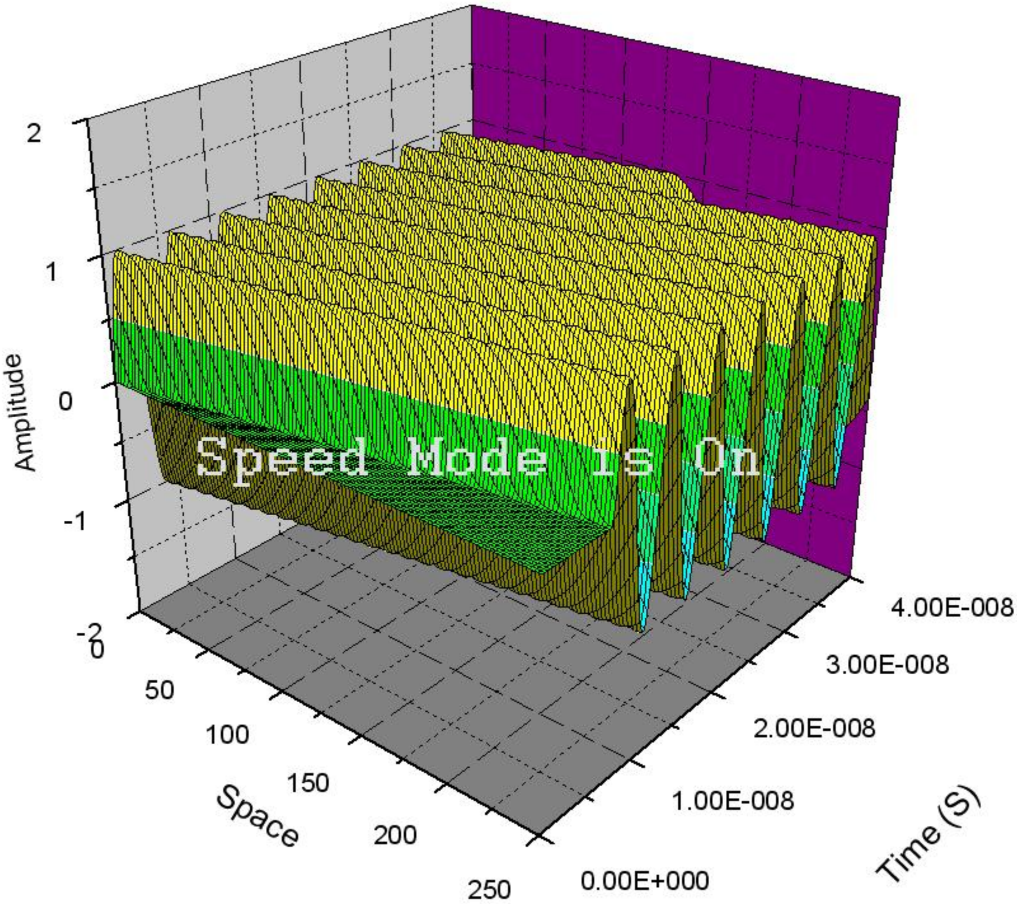

Fig. **5-6**: Simulation results of applyng absorbing boundary condtion at the right side of space dimension.

The simulation results clearly show that without absorbing boundary conditon, the propagating acoustic wave will reflect from the right end of the simulated structure. Those reflected wave will mess up the continuous wave form and make the final data collection almost impoosible. By replacing the fixed boudary condition with the absorbing boundary condition, the results improve greatly. There is no more boundary reflection influence.

Chapter 6

MATCHING LAYER DESIGN WITH GRADIENT ACOUSTIC IMPEDANCE

6.1 Matching Layer with Gradient Acoustic Impedance

6.1.1 Introduction

As discussed in previous chapters, the matching layer provides the required acoustic impedance transition so that the acoustic energy from the piezoelectric resonator can be efficiently sent into the human body tissue and the reflected signal can be return to the transducer for detection without too much loss.

Quarter wavelength matching layer has played its important role in this regard. However, quarter wavelength matching layer has a critical shortcoming of limited bandwidth. Simply improving the acoustic impedance of matching layer material doesn't solve this problem. The scheme of integrating two to four quarter wavelength matching layers has been discussed by some researchers [Collin 1955] [Goll and Auld 1975] [Inoue Ohta and Takahashi 1987], but the slightly increased bandwidth can not compensate the decrease of ultrasound intensity and performance caused by the increase of total matching layer thickness.

The rapidly growing new imaging techniques, such as harmonic imaging, in medical ultrasonography field and recently developed single crystal piezoelectric materials for ultrasonic transducers demand new matching layer designs to fully utilize the much broader bandwidth nature of the new piezoelectric materials [Shen, Li, 2001]. In traditional ultrasound imaging method, a fundamental frequency beam is sent out and then the reflected echoes at interfaces are received essentially at the same frequency the reflected echoes at interfaces. Sometimes, the noise signals reflected from the adjacent area of targeted tissues may distort the useful signals.

Under certain circumstance, ultrasound wave may be distorted because the target tissues may expand and contract under the influence of the incident wave [Li, Zagzebski, 2000]. When the incident wave's energy reaches a certain level, the distortion will generate additional higher harmonic waves (generally two or several times of the fundamental frequency) due to the nonlinearity of the tissues. The harmonic waves will travel back to the transducer together with the fundamental frequency beam [Wojcik, et al. 1998]. In second harmonic imaging, the wave having 2 times of the fundamental frequency are detected and utilized to form image, which can have higher resolution. Obviously, the harmonic signals are weaker than the fundamental wave, but it only has to travel half of the distance, therefore, the attenuation is reduced by a factor of 2, which makes the second harmonic waves detectable. The most advanced ultrasonic imaging machines can perform both fundamental frequency imaging and second harmonic imaging [Chen, Panda 2005].

The transducers used in harmonic imaging must have very broad bandwidth, because they not only need to send out fundamental frequency beam, but also have to have the ability to receive second harmonic waves with twice of the fundamental frequency [Hackenberger, et al. 2003]. New piezoelectric single crystals PZN-PT and PMN-PT have electromechanical coupling coefficient more than 95%, which is capable to produce transducers having over 100% bandwidth [Rehrig, et al. 2003] [Vos, et al. 2003]. However, the quarter wavelength matching layer has limited bandwidth (<50%) which may prevent the final transducer to realize better than 80% bandwidth. Because second harmonic imaging is conducted at higher frequencies, it can obtain better resolution images [Bouakaz, De Jong 2003]. But at the same time, higher attenuation of higher frequency waves causes the reduction in penetration depth. Therefore, good matching layer design can help resolve this issue. The new matching layer designs should provide small energy loss and wider bandwidth. In addition, the fabrication process should be convenient and low-cost.

A matching layer structure with a gradient of acoustic impedance through its thickness direction isn't a totally new idea. Some theoretical works had been done [Haller, Khuri-Yakub 1993] and there are also limited efforts in fabricating such matching layers [Sato, Katsura and Kobayashi 2002]. However, those investigators only discussed simple calculations based on the KLM circuit model. The material selection also did not consider the restriction of high attenuation coefficient. The LKM model is limited in dealing with different types of gradient design and cannot treat different boundary conditions.

In this chapter, we will use numerical FDTD method to simulate the ultrasonic signal transmission in a three layers structure: piezoelectric layer, matching layer with gradient acoustic impedance and body tissue layer. Simulations are conducted with three different impedance gradient designs: The first one has linear form, the second one has exponential form and the third one has power form. All results will be analyzed and compared to provide an optimized gradient matching design.

6.1.2 Three Gradients of Acoustic Impedance

In order to bridge the acoustic impedance gap between the piezoelectric material and body tissue, a stepwise decrease impedance distribution may be used. The thickness of ultra high frequency ultrasonic transducer matching layer is in the scale of just several microns, therefore it's not practical to apply complex impedance distribution in such a thin structure. Therefore, we only conducted analyses on three simple gradients. There are now experimental techniques to deposit porous thin films with controlled porosity, which may be used to implement such continuous acoustic impedance distributions.

Type 1: Assume x>0, the value density function of a linear distribution has the form:

$$f(x_i) = f(x_1) + \frac{i}{n}(f(x_n) - f(x_1)) \quad (i=1\ldots n) \qquad \text{(Eq 6-1)}$$

If the highest and lowest acoustic impedances are respectively 30Mrayls and 1.5MRayls, the impedance curve for linear distribution is shown in Fig. 6-1:

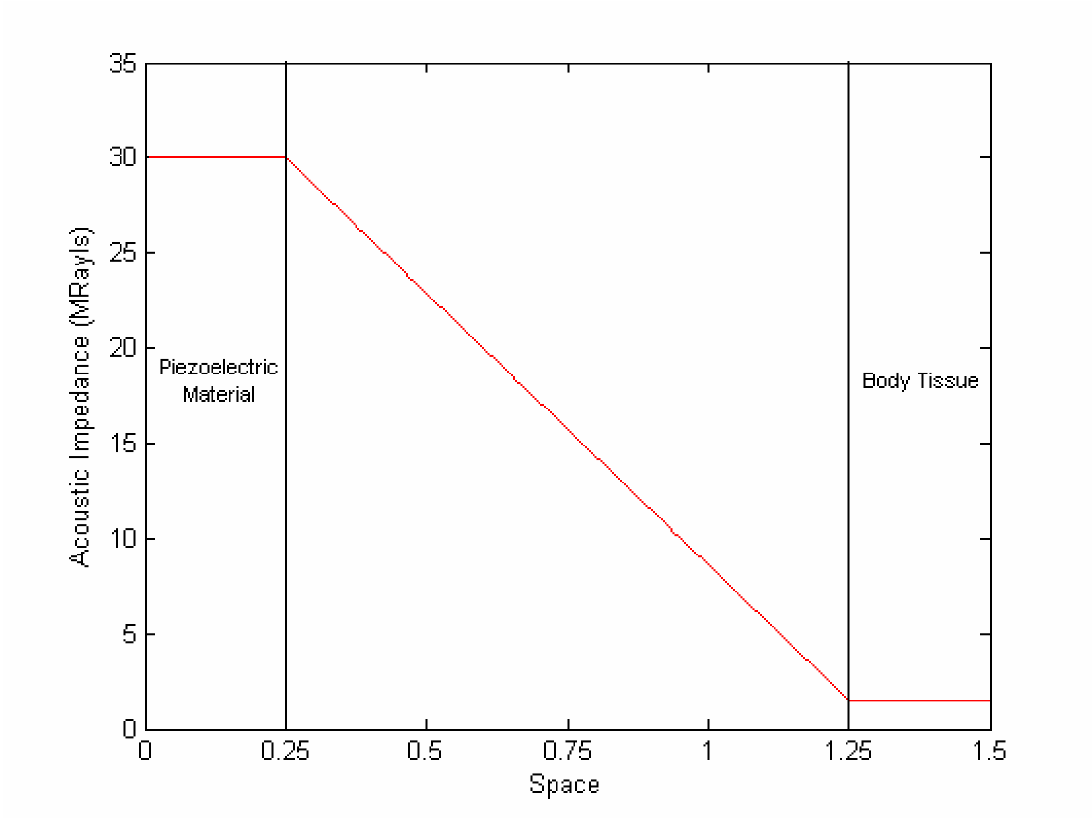

Fig. **6-1**: Linear acoustic impedance distribution in matching layer.

Type 2: The second gradient we explored is exponential distribution. Its acoustic impedance variation has the following form:

$$f(x_i, \lambda) = f(x_1) + e^{\frac{-\lambda x_i}{x_n}} (f(x_n) - f(x_1)) \qquad \text{(Eq 6-2)}$$

where λ > 0 is the rate parameter of the distribution. The curves of exponential distributions with different λ are shown in Fig. **6-2**.

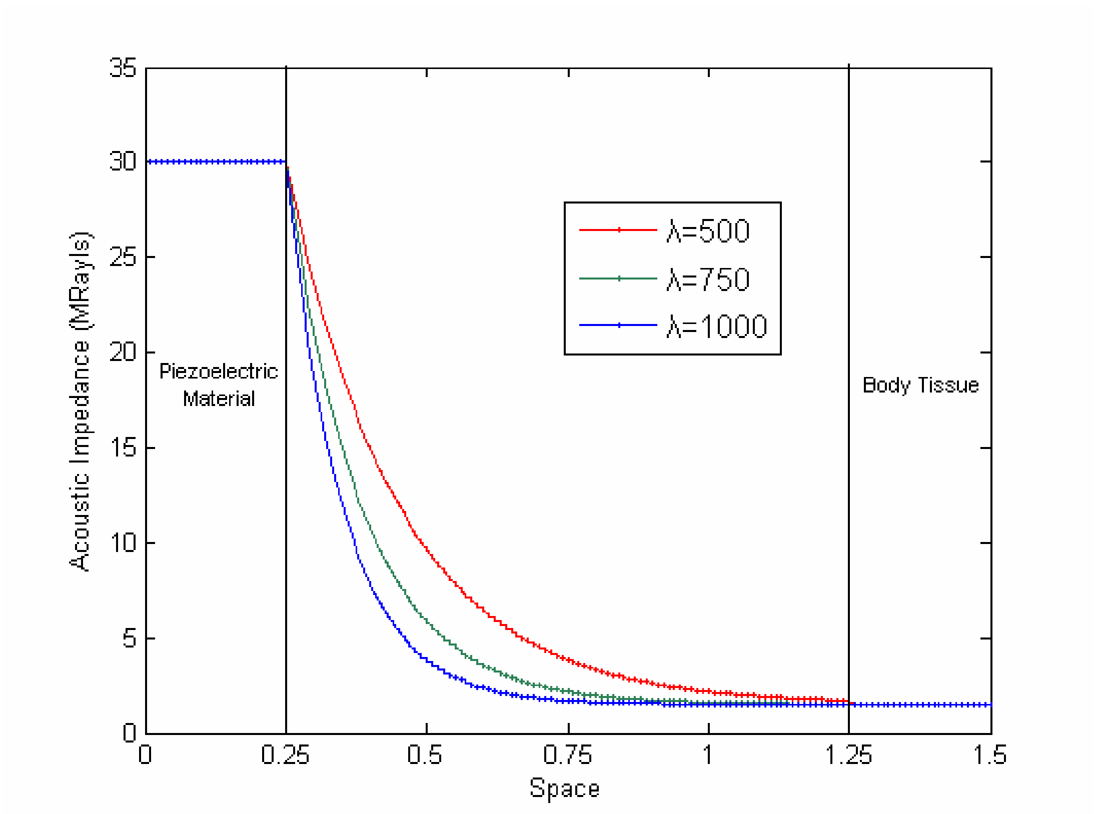

Fig. 6-2: Exponential acoustic impedance distribution in a matching layer.

The corresponding symmetrical curves of Fig. 6-2 along the diagonal are shown in Fig. 6-3. For exponential distribution, the steep drop of acoustic impedance happens near the interface of piezoelectric section and matching layer, while for their symmetrical ones, the steep drop of impedance happens near the interface of matching layer and tissue. Both exponential distribution and its symmetrical one will be simulated to study their performance.

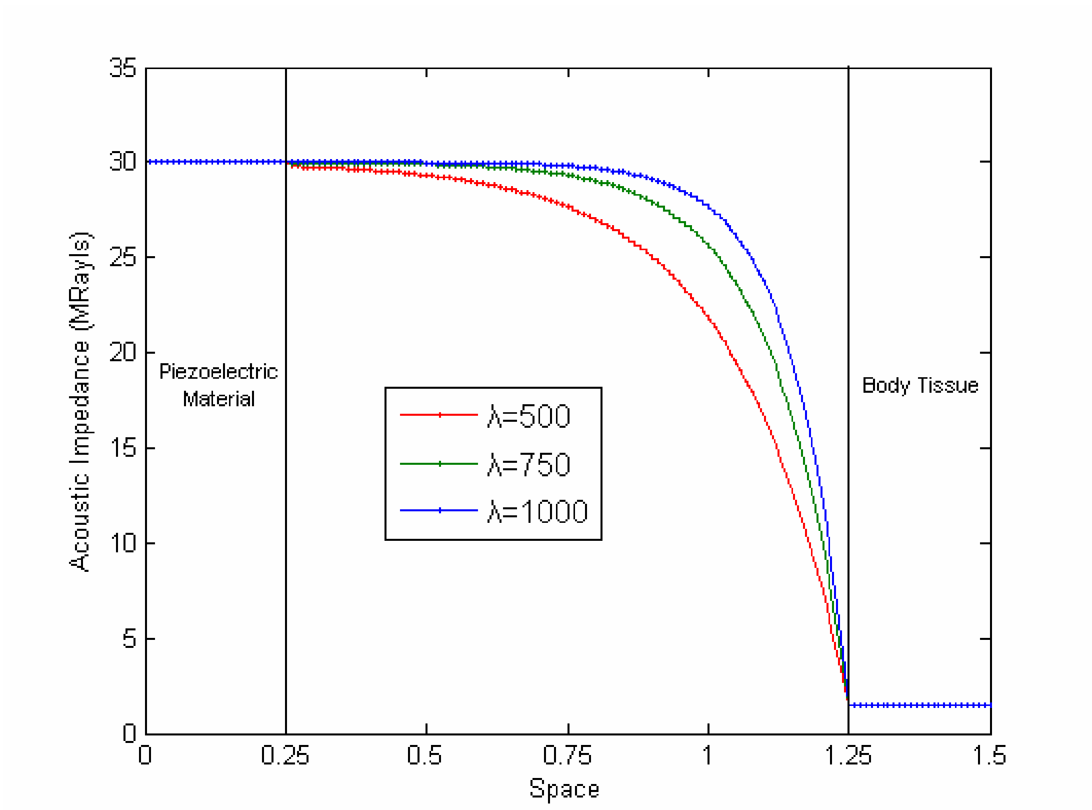

Fig. **6-3**: Symmetrical curve for exponential acoustic impedance distribution of Fig. **6-2** in a matching layer.

Type 3. Finally, we consider a distribution where the logarithm of the function shows a linear distribution as shown in Eq **6-3**,

$$\log(f(x_i)) = \frac{i \cdot (\log(f(x_n)) - \log(f(x_1)))}{n}$$
$$\Rightarrow \quad f(x_i) = f(x_0)\left(\frac{f(x_n)}{f(x_0)}\right)^{\frac{i}{n}} \qquad \text{(Eq 6-3)}$$

The curve of the third distribution and its corresponding symmetrical along the diagonal are shown in Fig. **6-4**:

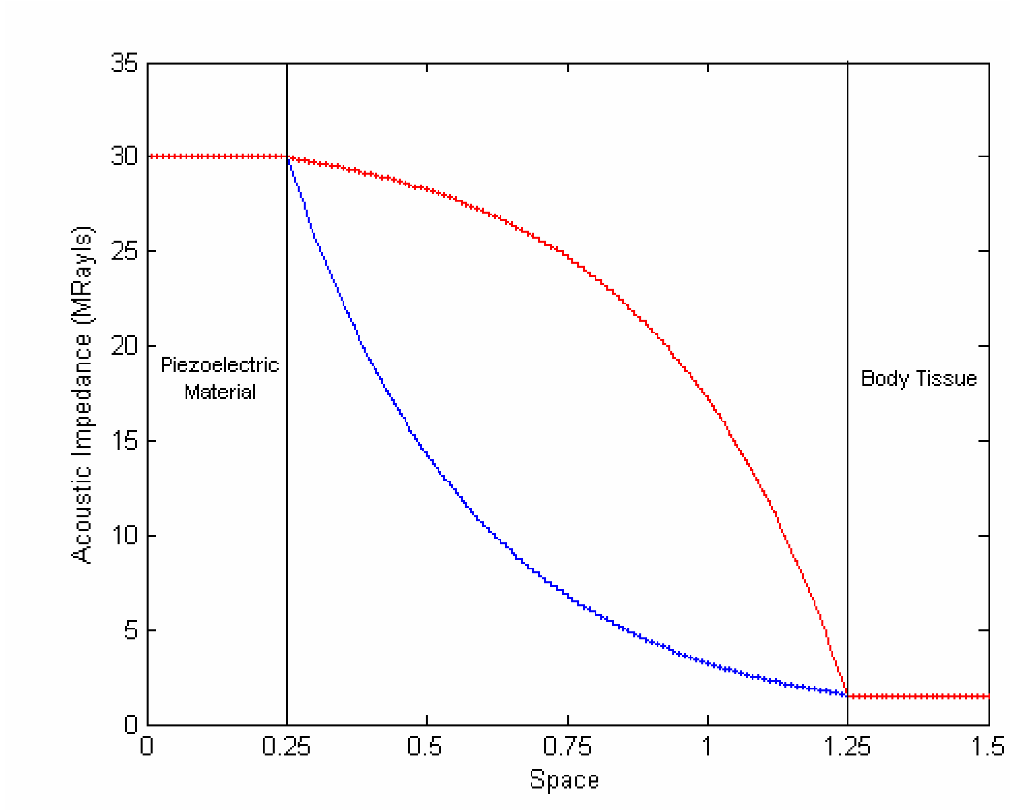

Fig. 6-4: The third and its symmetrical distribution curves.

6.2 Application for FDTD Simulation and Data Analysis.

6.2.1 Visual C++ Simulator

The application for FDTD simulation is programmed with Microsoft Visual C++ 6.0. C++ is a general-purpose Object-oriented programming (OOP) language. As a mid-level language, it comprises a lot of features you can find both in high-level and low-level languages. The type checking is performed during compiling-time instead of running-time. The positioning of characters position in program is not that significant, users don't need to place their scripts in specific columns. C++ supports multiple programming paradigms. However, the most important thing about C++: it is a compiled language.

In general any language can either be implemented by a compiler or by an interpreter. For a compiler language, the implementation is established by translating the source codes into machine codes through the compiling procedure. While for an interpreter language such Matlab, the source codes are executed step-by-step without any translation or compiling.

Normally, to execute the same application, a compiler language program needs a lot less running time, sometimes 5-10 times less than an interpreter language program. For our simulations, the execution of application involves a great amount of floating-point calculations and leapfrog processes. Therefore despite its shortcomings of implementation complexity and long edit-run cycles, we choose C++ instead of Matlab as programming language based on the runtime concerns. Although in the future, it may be useful to consider a hybrid method of combing the compiler language with interpreter language to increase the efficiency. Microsoft visual C++ is a commercial integrated development environment (IDE) C++ programming. It has tools for designing the graphic user interface, writing and debugging C++ code. As powerful software, it provides enough tools for our simulator programming.

The sketch map of our simulation program's principle is shown in Fig. **6-5**. All points in the x-axis will be initially set as zero so there is no existing wave propagation to begin with. An exciting source is added at the point A from the first slot in time domain. Wave form then start to transmit along the x axis with time passing by. Points B and C are the boundary points. The Mur's absorbing boundary condition will be applied at point D so that no wave will be reflected. After the multiple reflected waves make a steady wave form in tissue layer, the wave amplitude will be sampled.

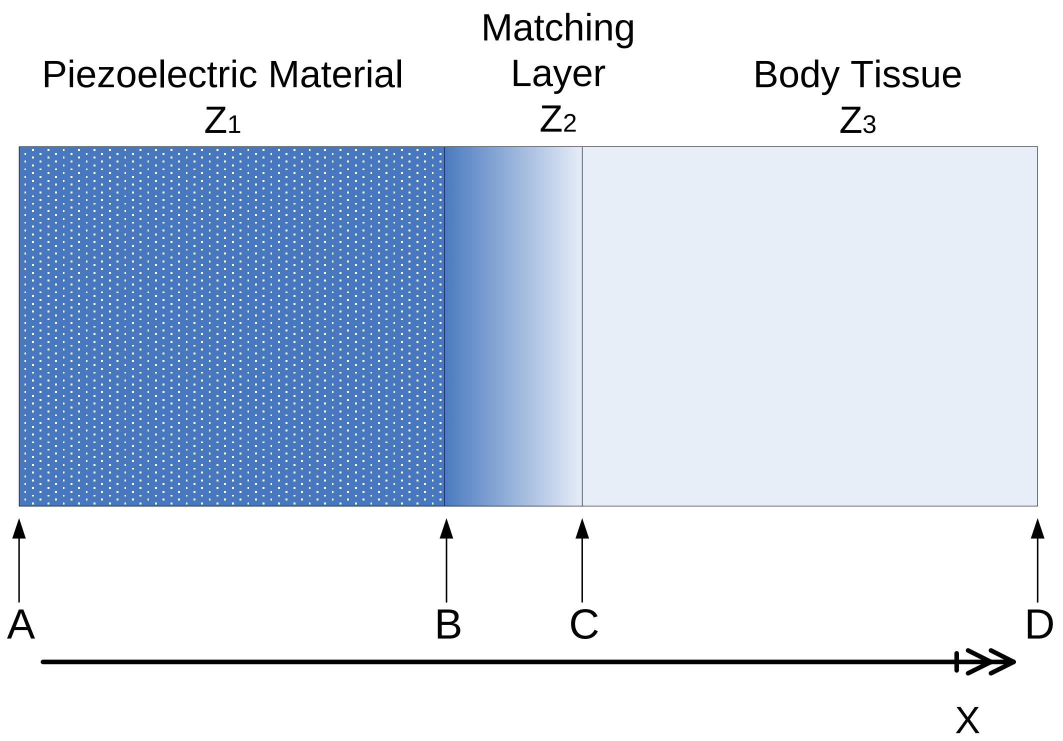

Fig. 6-5: Schematic of simulation object.

The density, sound speed and the length of the body tissue layer are set. The parameters need to be input by user are:

- The density, sound speed and thickness of the piezoelectric material layer
- The thickness of piezoelectric material and matching layer.

- The highest acoustic impedance in matching layer. The lowest is set the same as the acoustic impedance of body tissue.
- Choice of linear impedance distribution or exponential distribution. If exponential distribution is chosen, the rate parameter λ needs to be provided. By inputting a negative λ, user asks the program to apply the positive λ's symmetrical distribution along the diagonal.

The graphical user interface of the program is shown in Fig. **6-6:**

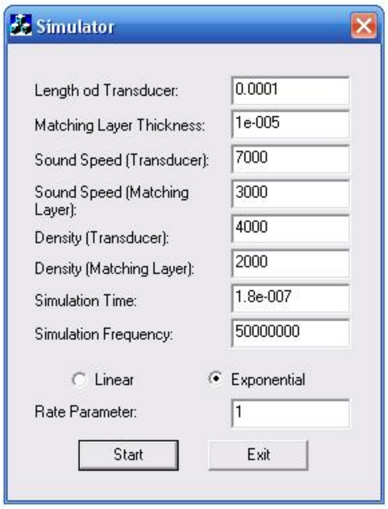

Fig. **6-6**: GUI of the simulation program.

Although it may increase the burden of program and computer resource, the thickness of piezoelectric material and body tissue layer need to be relatively large, but for different reasons. The piezoelectric material layer should be long so the reflected wave from point B in Fig. 6-5 will take sufficient long time to travel and reflect from exciting point A, thus no interference with the waves inside the matching layer. Thickness of tissue layer ought to be at least 3 to 4 times of the wavelength, so that ample amount points of signal can be sampled to increase the accuracy.

6.2.2 Data Collection and Demonstration

The collected data was not processed and displayed by C++ program. There are mature commercial softwares available for this purpose. Thus all the signals sampled are written into a single file using american standard code for information interchange (ASCII). The space, time and displacement information are all saved simultaneously after they are calculated. To save program running time, the target data collection area can be set in the simulation program.

Files containing simulation results are imported into the worksheets by OriginPro 7.5 scientific graphing and data analysis software package from OriginLab. Those data are then explored and processed either in worksheets or graphically. OriginPro has its own C++ compiler for matrix conversion. It can build 2D, 3D, surface images and contour graphics of the worksheets data. Its mathematic tools can help signal processing, curve fitting and peak analysis. Fig. 6-7 shows a 3-D sample graph of a single wave's transmission and reflection in a three layer structure. X is the space dimension, Y and Z denote time and amplitude respectively.

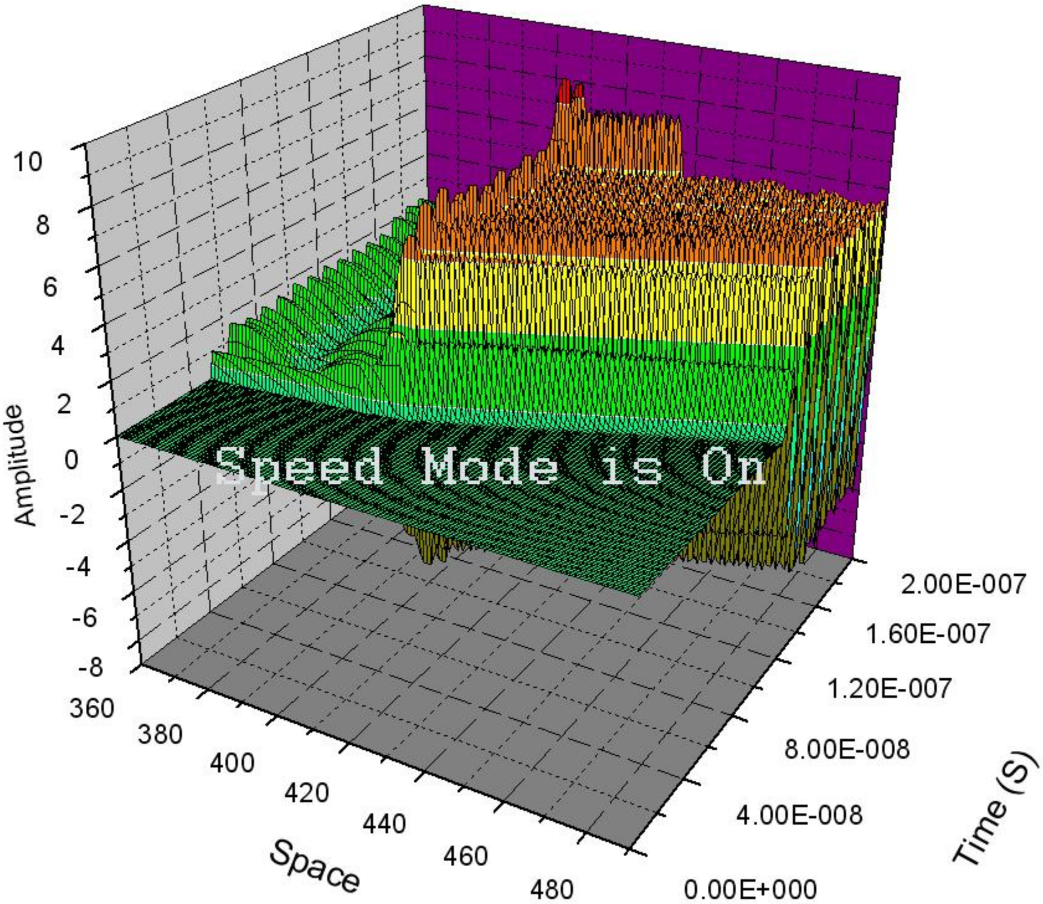

Fig. 6-7: 3-D sample graph using OriginPro.

6.3 Simulation Results

Some parameters in the wave propagation simulations are fixed. The sound velocity of piezoelectric material is set at 4200m/s, while the density is $7500\,kg/m^3$. Body tissue's sound speed and density are set at 1482m/s and $998\,kg/m^3$, respectively. We will adjust the matching layer thickness, matching layer acoustic impedance distribution, the highest and lowest acoustic impedance values to understand the matching layer influence on transmission coefficient.

The first simulation is to use the most popular high frequency transducer matching layer material: parylene. The thickness of the matching layer is set at 40 microns. The normalized transmission coefficient spectrum of using the quarter-wavelength parylene matching layer is presented in Fig. 6-8.

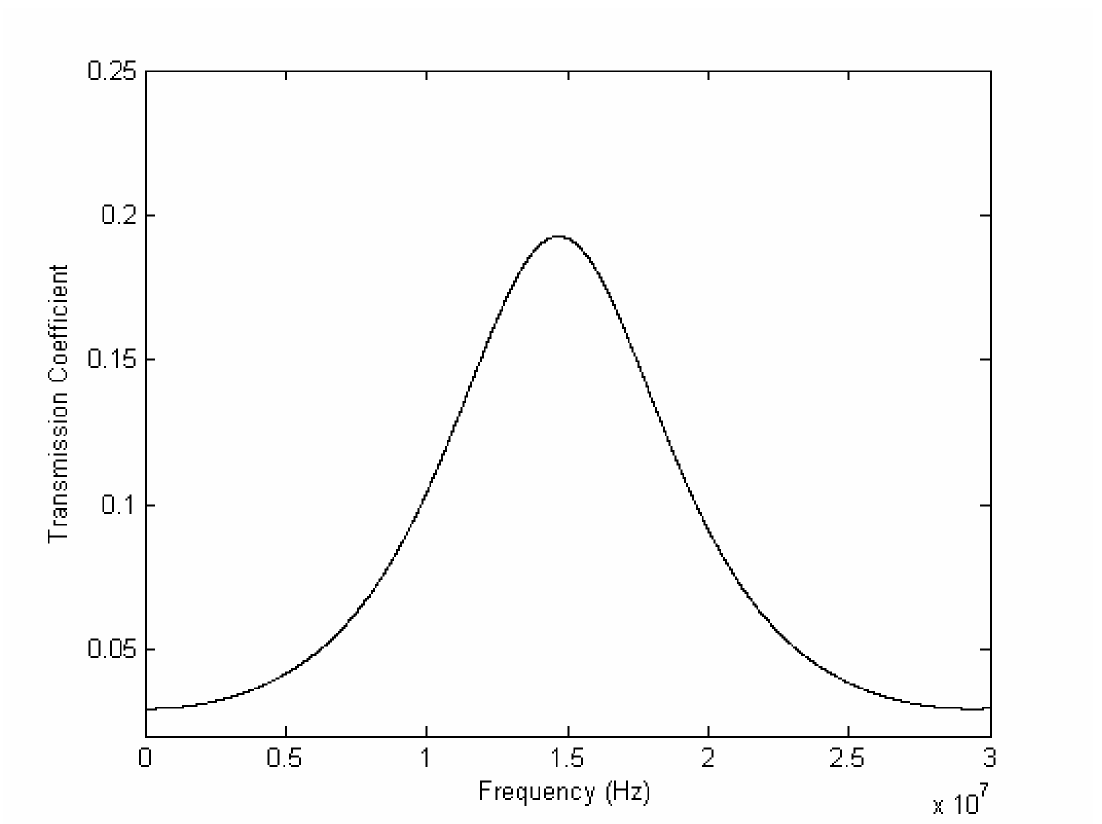

Fig. 6-8: Spectrum of transmitted wave through quarter-wavelength Parylene matching layer.

From the simulation results, quarter-wavelength parylene matching layer provides poor transmission coefficient although it is better than non-matching situation. The best transmission coefficient can be achieved is only about 20%, which means most energy can not be transmitted into the imaging medium even at the transducer's central frequency.

Now we replace parylene with the new nano-structured TiO_2 material developed in this thesis work, the simulation results are presented in Fig. 6-9:

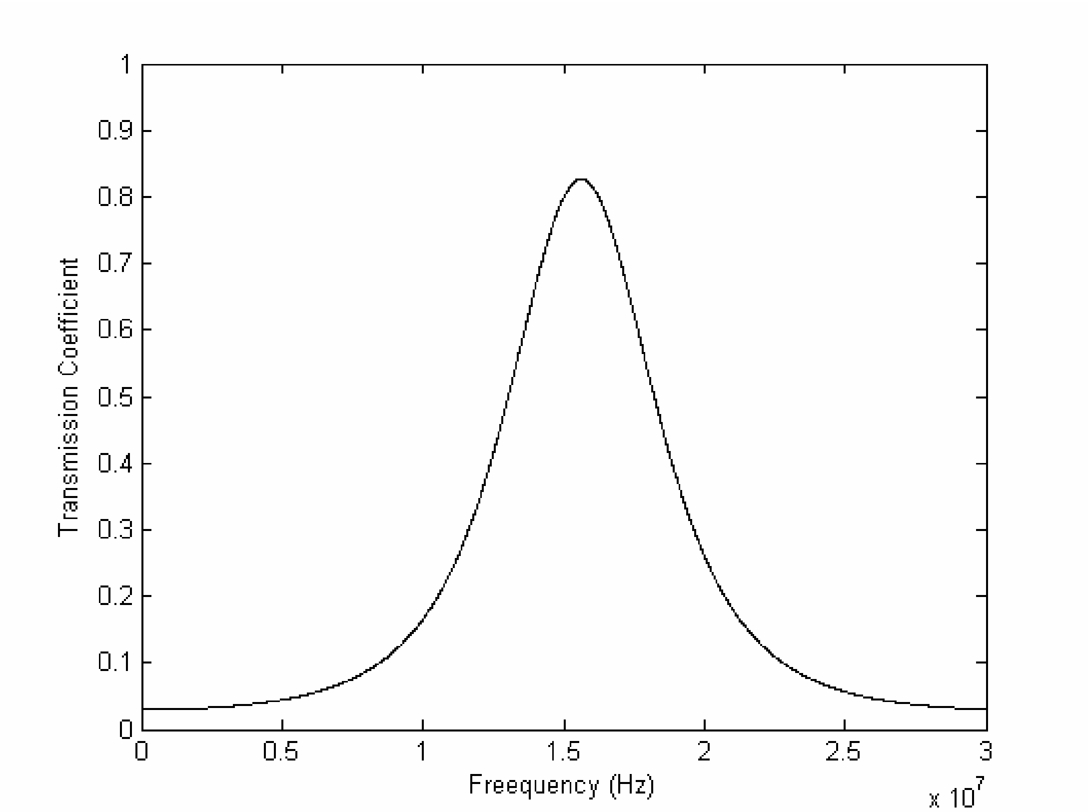

Fig. 6-9: Spectrum of transmission coefficient for wave through quarter-wavelength new TiO_2 nan-structured material matching layer.

The new nano-structured TiO_2 material provides a great improvement compared to the old parylene matching layer, the peak transmission coefficient can reach as high as 90%. However, the bandwidth is still at a very low level. These simulation results matched well with the output of PiezoCAD calculations which further verified out FDTD method.

Matching layers with gradient impedance are then put into the simulation model. Results from the first type gradient of Fig. **6-1** are displayed in Fig. **6-10**:

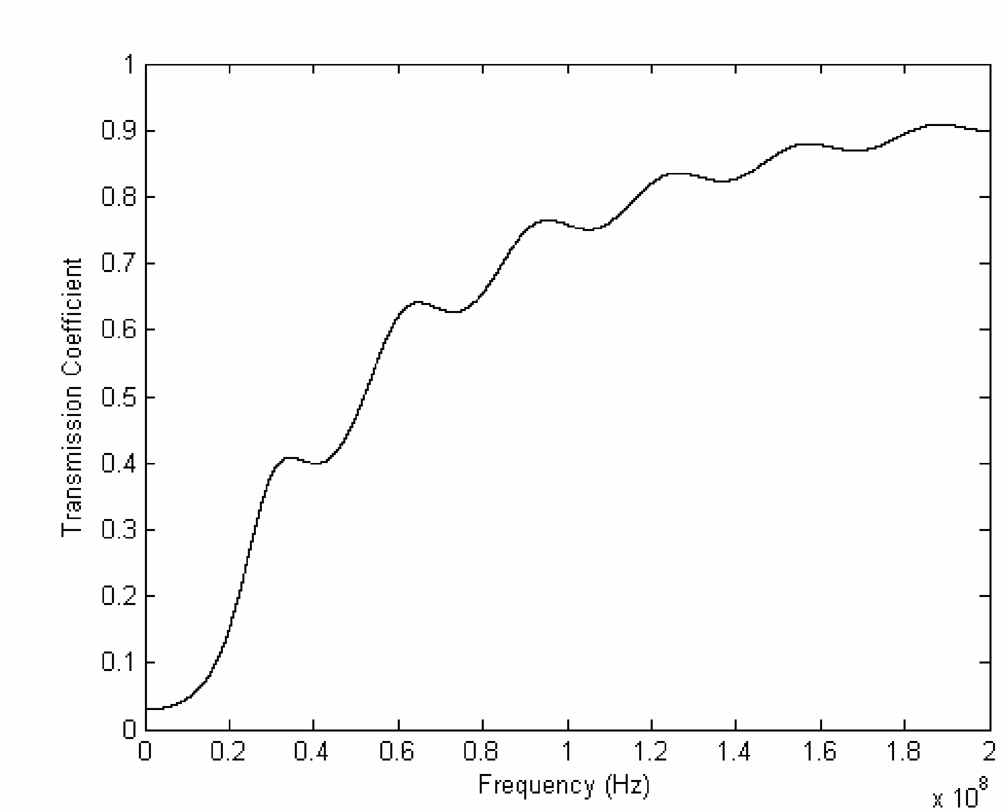

Fig. **6-10**: Spectrum of transmission coefficient for wave through matching layer with first type gradient acoustic impedance.

The simulation supplies a very interesting result. The transmission coefficients are at a relatively low level at low frequencies, increases with frequency and reaches 90% near 200MHz. This design has provided some improvements in terms of transmission coefficient and bandwidth. But the transmission coefficient increase is very slow and most low frequency region still suffer from low transmission.

The next simulation design is changing acoustic impedance gradient from type 1 to type 2 shown in Fig. 6-2. Three rate parameters λ are used in the simulation and the outcome are presented in Fig. 6-11:

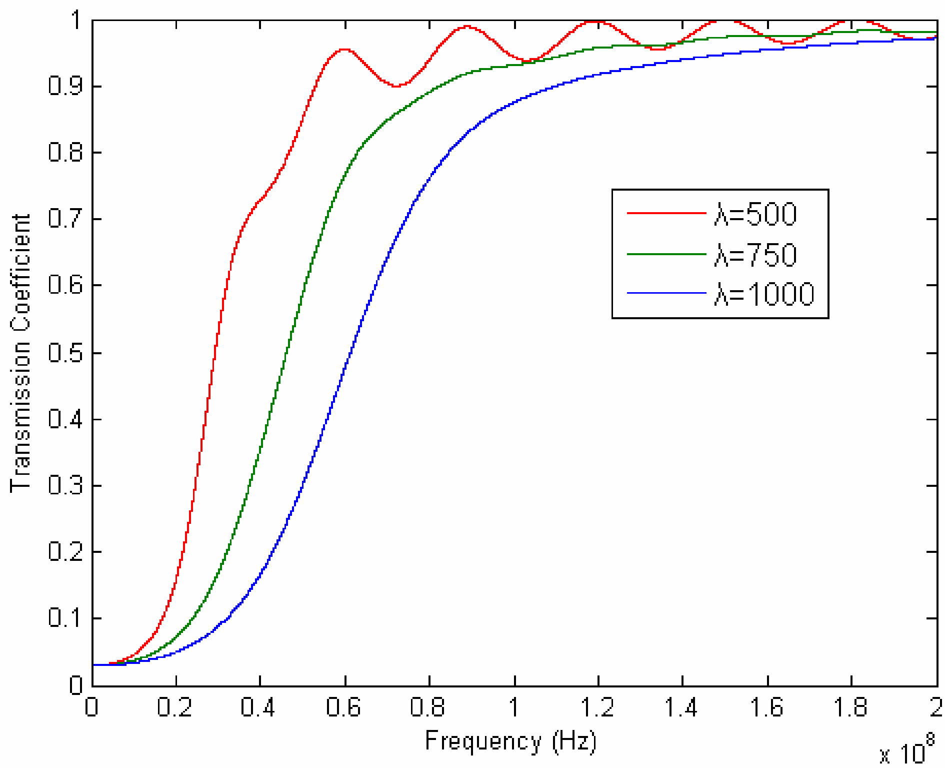

Fig. 6-11: Spectrum of transmission coefficient for wave through matching layer with type 2 gradient acoustic impedance.

Apparently the variation of exponential rate parameter leads to some difference of final transmission coefficient spectra. All the transmission coefficient curves steadily increase and near 100% at ultra high frequencies. However, if we decrease the exponential rate parameter, the matching layer's bandwidth at low frequency will increase. When the rate parameter λ/n is set at 2, the transmission coefficient reaches 80% at about 80MHz. When we change λ/n to 1, the frequency at which transmission coefficient correspondingly reaches 80% moves to about 40MHz, which is better than the results from higher rate parameters.

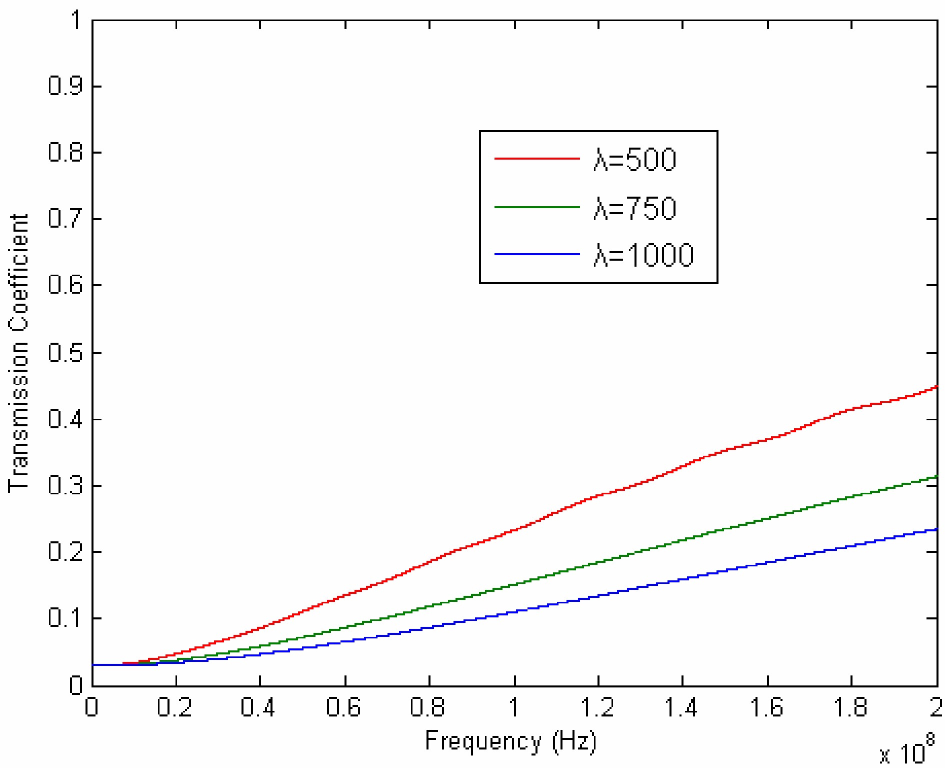

Fig. **6-12**: Spectrum of transmission coefficient for wave through matching layer with symmetrical acoustic impedance distributions of type 2 gradient.

The type 2 gradient's symmetrical counterpart along the diagonal are also simulated. The final results are presented in Fig. 6-12. Compared with the curves in Fig. 6-11, the change is dramatic. By moving the steep drop of acoustic impedance from near the piezoelectric-matching layer interface to the matching layer-tissue interface, the increase rate of transmission coefficient with frequency becomes totally unacceptable for matching layer applications. Obviously we can not apply this kind of acoustic impedance distribution in matching layer design.

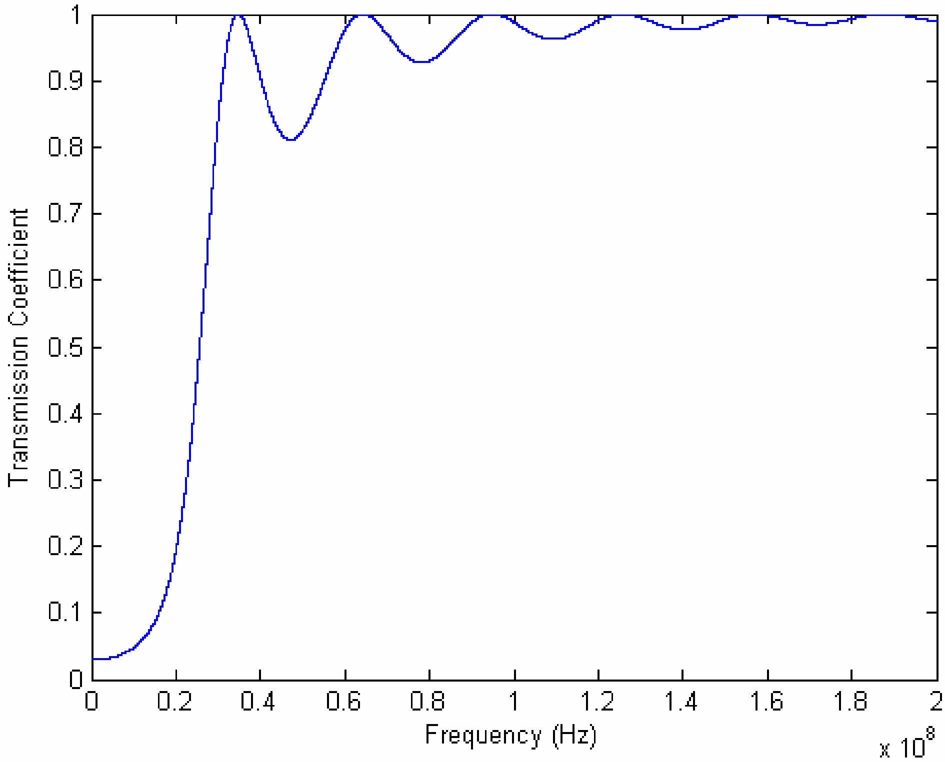

Fig. 6-13: Spectrum of transmission coefficient for wave through matching layer with type 3 acoustic impedance distribution shown in Fig. 6-4.

The simulation results of applying the final acoustic impedance gradients are shown in Fig. **6-13**. This is the best result we can get after applying several different scenarios into the simulations. At low frequencies, the transmission coefficient increases very quickly to reach 100% and stays between 80-100% for a very broad frequency range. But there is an obvious fluctuation which may be a drawback to the overall performance of transducers.

Transmission coefficient of the corresponding symmetric distribution of above situation is shown in Fig. **6-14**. Similar as the results in Fig. **6-12**, this kind of distribution should be avoided in matching layer designs.

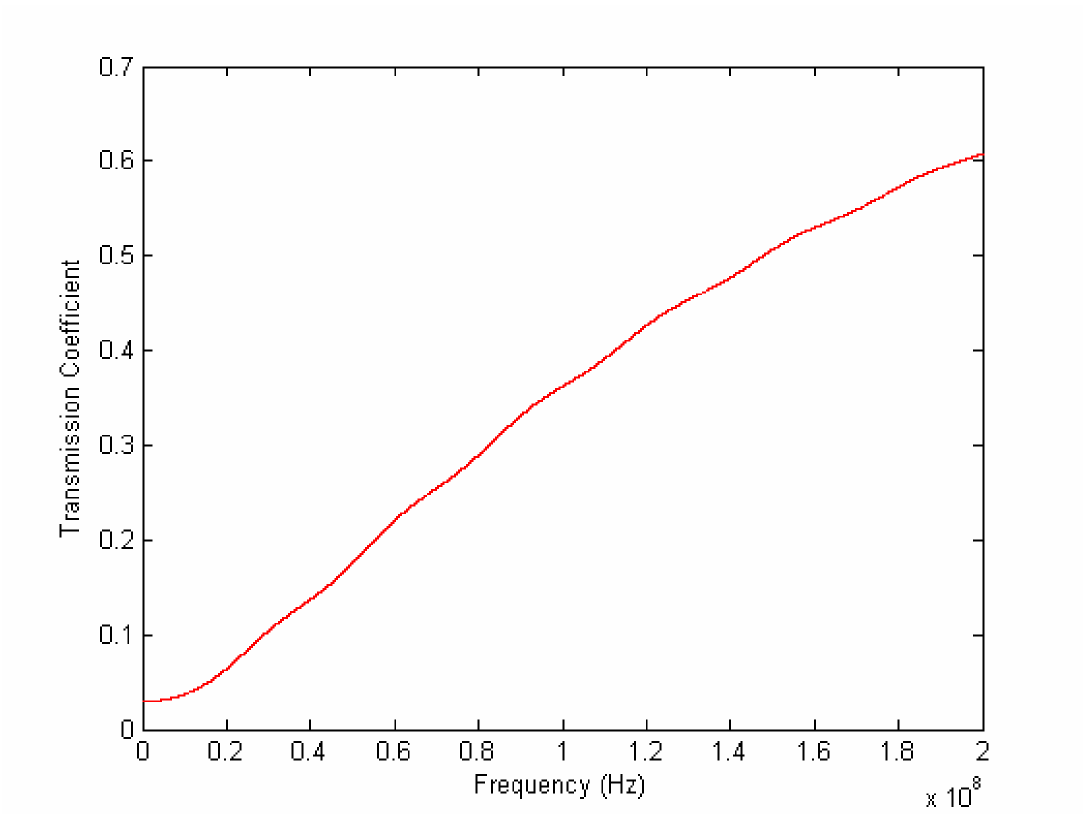

Fig. **6-14**: Spectrum of transmission coefficient for wave through matching layer with symmetrical acoustic impedance distribution of type 3 shown in Fig. **6-4**.

From the simulation results, it is clearly shown that the third distribution provides the best transmission coefficient window for broadband transducer applications. But it is still necessary to discover what will happen if part of this 1.5-30MRayls continuous variation is missing. We chose three scenarios, they all used the third type gradient but with different start and finish acoustic impedance values. The first one is from 16-30MRayls, the second is from 9-23MRayls and the third is from 1.5-16MRayls. The acoustic impedance distribution curve is shown in Fig. **6-15**:

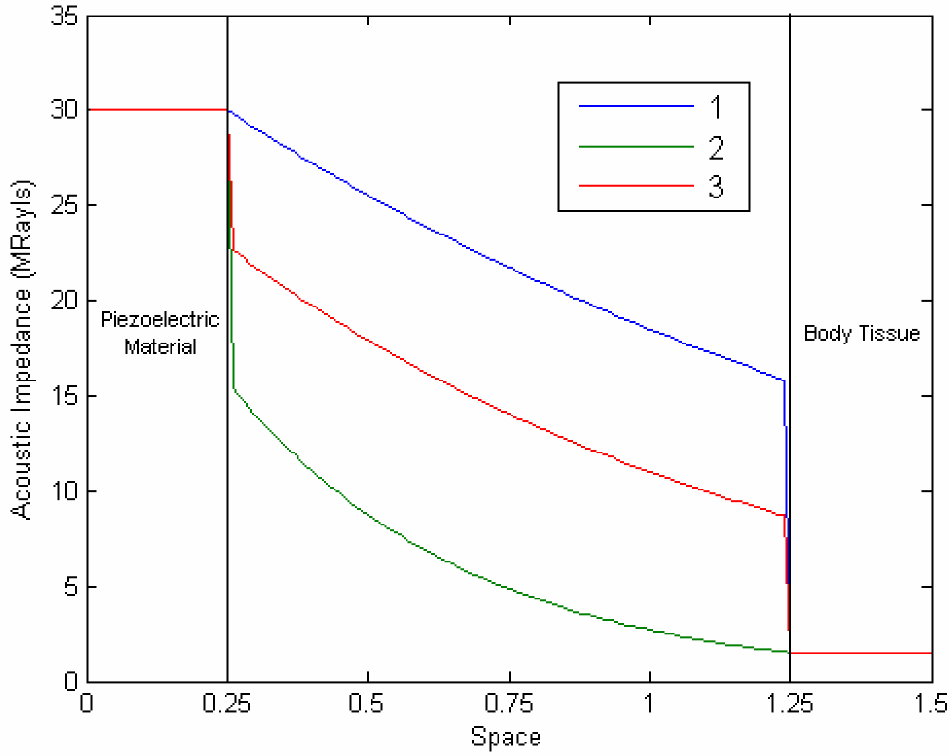

Fig. **6-15**: The third type acoustic impedance distribution with start and finish acoustic impedances having a jump with the piezoelectric and tissue materials.

The three transmission coefficient curves in Fig. 6-16 look totally different although they have the same distribution function. Transmission coefficient curve from 16-30MRayls distribution is flat, but even the peak value can't surpass 10%. When the acoustic impedance values of the distribution zone decrease, the corresponding transmission coefficients begin to increase and vary between 60-90% when the 1.5-16MRayls distribution is applied, and oscillating fluctuations are formed. But none of the results can compare to the one shown in Fig. 6-12.

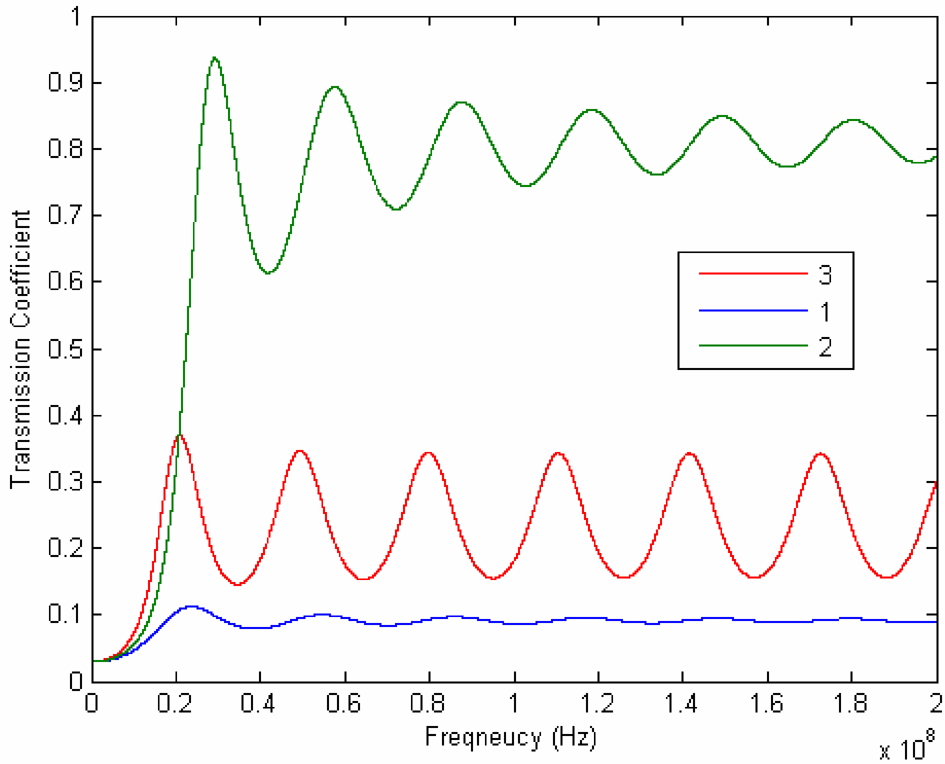

Fig. 6-16: Spectrum of transmission coefficient for wave through matching layer with acoustic impedance distributions shown in Fig. 6-15.

Fig. 6-16 tells us that if we want a good matching layer design with gradient acoustic impedance distribution, we should have different materials whose acoustic impedances can cover the full range from tissue to piezoelectric materials.

Finally, we double the thickness of matching layer to 0.08mm in order to provide a good matching design for lower frequencies. We still use the third type distribution shown in Fig. 6-4. The initial transmission coefficient curve at low frequencies in Fig. 6-17 becomes steeper and the first total transmission peak appears at 18MHz, which further broadens the matching layer's performance to lower frequencies.

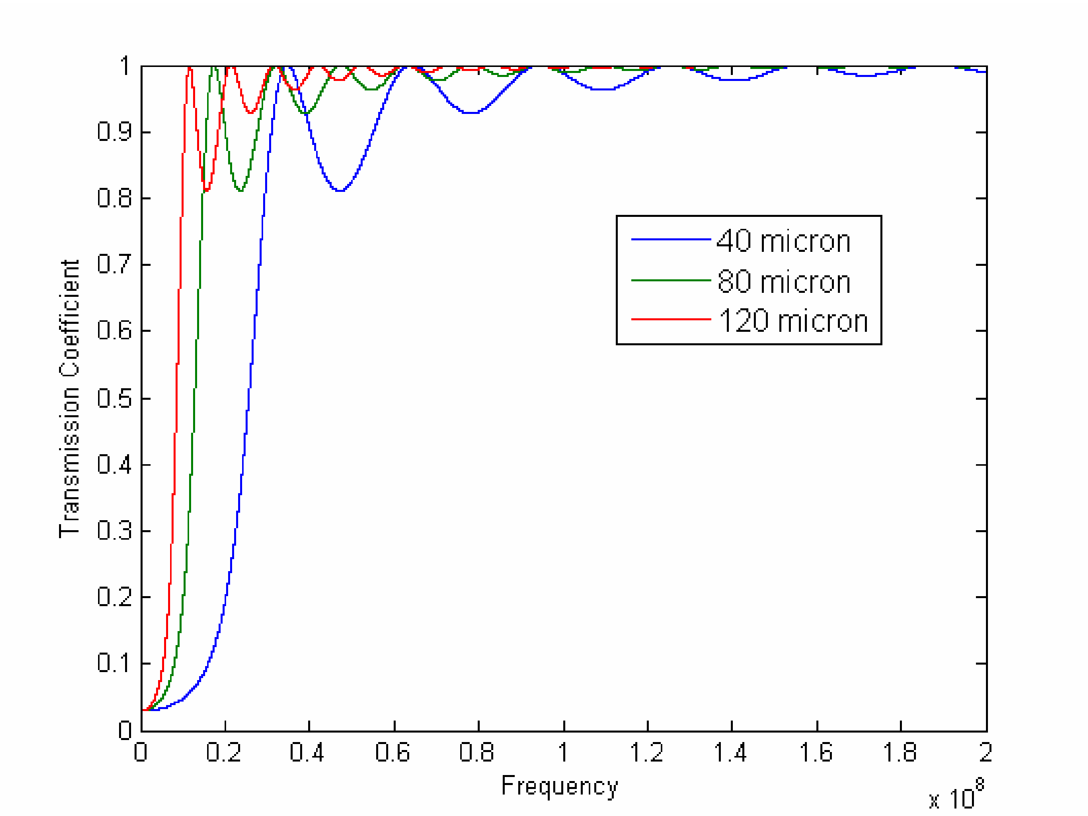

Fig. 6-17: Spectrum of transmission coefficient for wave through matching layer with the acoustic impedance distribution shown in Fig. 6-4.

6.4 Design and Fabrication of Matching Layer with Gradient Acoustic Impedance

Fabrication of high frequency ultrasonic transducer matching layers with gradient acoustic impedance is a very challenging work because of the thickness limitation.

The ideal structure is shown in Fig. 6-18. To fabricate such a single layer material with different acoustic impedance distributions, we must first deposit a single layer material on substrate, and then use some technique to modify the acoustic impedance in the adjacent layer, such as controlling the porosity. Currently, it is impossible to manufacture such accurately controlled film. In order to get a wide distribution of the acoustic impedance from 1.5-30MRayls, two or three different type of materials may be used. Although there are already reported porous film processing technique, but there is still a long way to go before one can accurately control the amount of porosity in the film. Based on this fact, we propose some other practical geometry designs as described below.

Fig. 6-18: Ideal matching layer design with gradient acoustic impedance distribution.

One possible solution is the pyramid-like structure as shown Fig. 6-19 and Fig. 6-20. Material with high acoustic impedance such as tungsten and PZT are grinded into powder and molded as multiple small square tapers. The bottoms of the tapers are attached with the piezoelectric material plate and the top is pointed to the tissue area. Low impedance material like epoxy is filled into the vacancies.

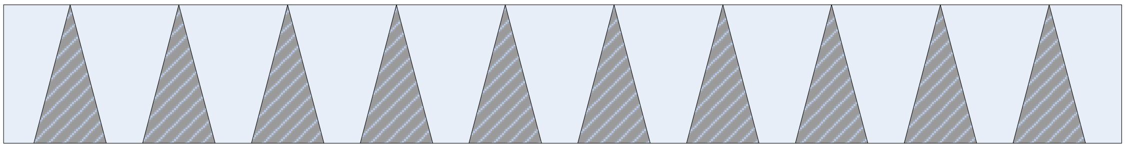

Fig. 6-19: Pyramid-like matching layer design with gradient acoustic impedance distribution.

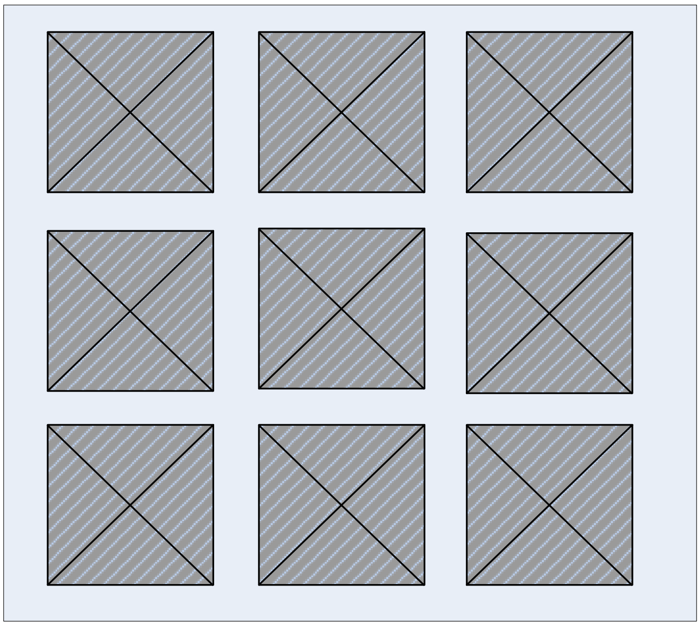

Fig. 6-20: Top view of pyramid-like matching layer design with gradient acoustic impedance distribution.

This pyramid structure requires only simple and quick fabrication procedure so it is appropriate for volume-production. For this design, we only need to change the shape of the tapers to get different acoustic impedance distribution. However, there are two major disadvantages of this design. In this structure, the high acoustic impedance material is distributed through the whole layer in the direction of wave propagation. Those materials normally have very high attenuation coefficients [Vogel 1985], so this structure may degrade the sensitivity of the transducer. As shown in Fig. 6-21, the boundaries of the tapers are not parallel with the wave travel path. Therefore scattering will take place at those boundaries, and part of the wave will deviate from its path and go to different directions. The transducer's performance may have lower penetration depth, and the scattered waves may turn into noises, which will interfere with the receiving signal.

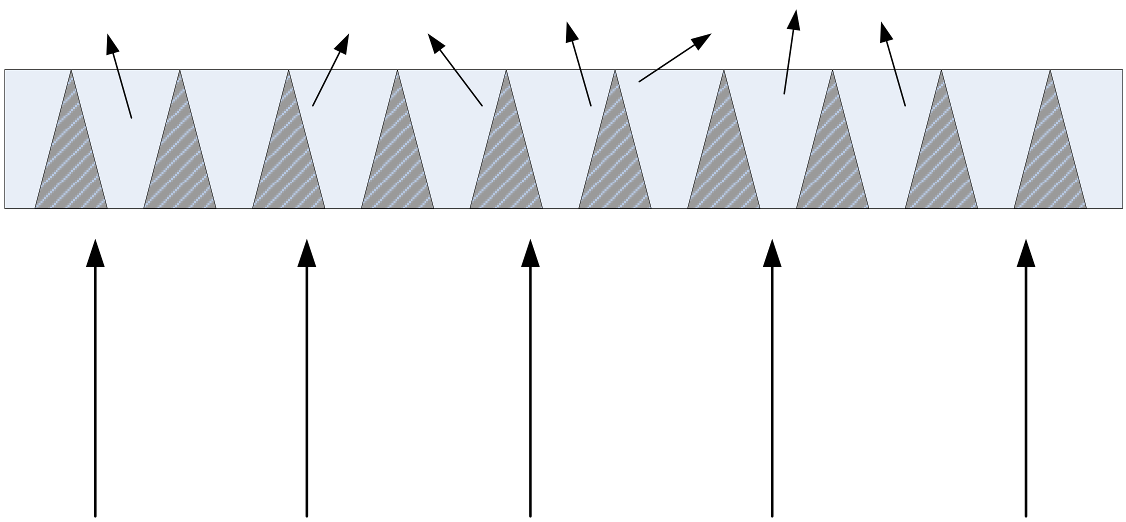

Fig. 6-21: Possible wave scattering caused by pyramid-like matching layer design with gradient acoustic impedance distribution.

Another possible design is shown in Fig. 6-22. The whole structure has many sub-layers and those sub-layers are deposited one after another. The acoustic impedance value of each sub-layer decrease stepwise from that of the piezoelectric material to that of the body tissue and satisfies the value density function of the chosen distribution. The total thickness of the whole matching layer should be set at one-quarter wavelength of the central active frequency at which the transducer is excited. Increasing the thickness of the total matching layer will improve the low frequency performance.

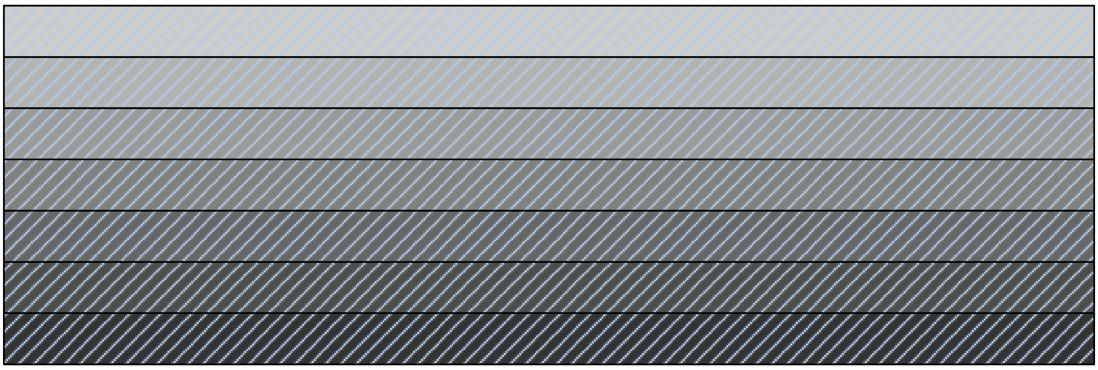

Fig. 6-22: Multi-Sublayers matching layer design with gradient acoustic impedance distribution.

During the fabrication, the first sub-layer which has the highest acoustic impedance is deposited on the piezoelectric plate. After sintering, the second sub-layer having slightly lower acoustic impedance is put onto the first sub-layer. Other sub-layers are deposited successively one layer on the top of another. All the depositions will be accomplished with the doctor-blade technique to strictly control the thickness of each sub-layer and the deposition material should have different amount of micro air-bubbles so that the film will have different amount of void in order to control the total acoustic impedance of each layer.

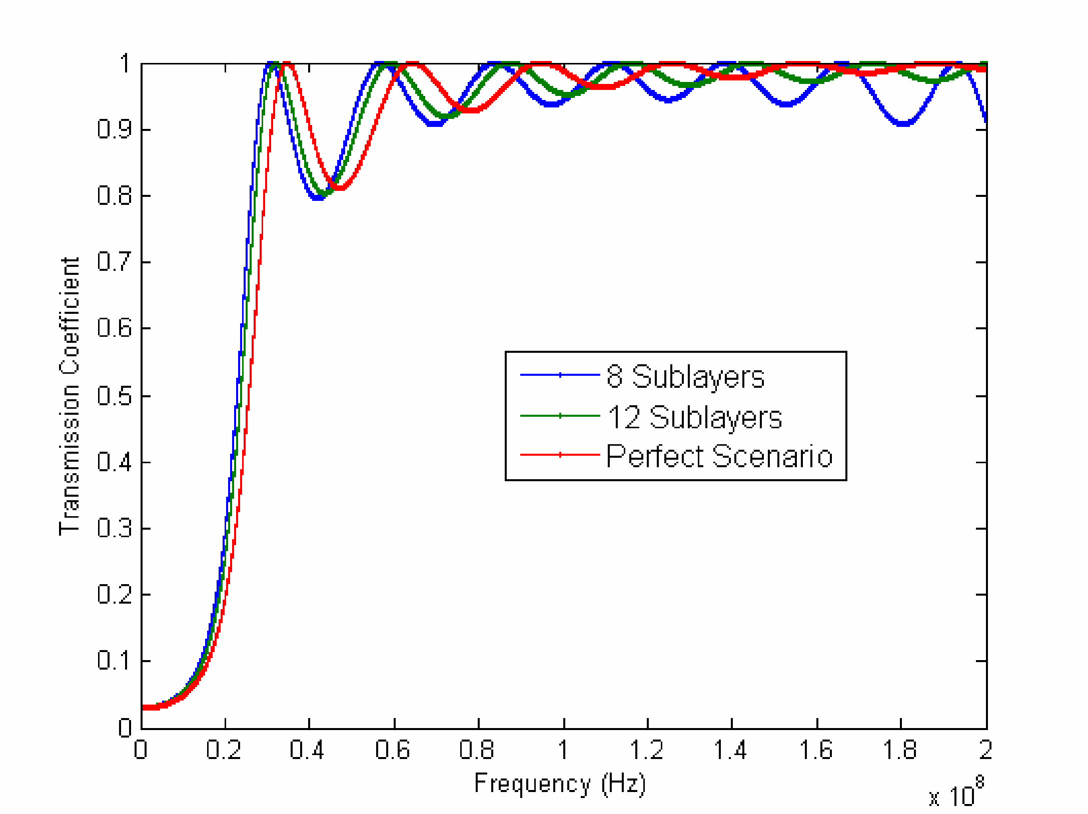

Fig. 6-23: Spectrum of transmission coefficient for wave through matching layer with acoustic impedance distributions shown in Fig. 6-4.

The number of sub-layers depends on the specific application requirements to achieve the balance between better transmission coefficient and fabrication complexity as well as manufacture cost. More sub-layers will bring better final result but more cost. Based on the simulation results in Fig. 6-23, 8-12 sub-layers already can provide satisfactory results, and the thickness of each sub-layer will be about several microns.

From our previous experiment experiences, doctor-blade technique can accomplish the film deposit work accurately at this thickness scale.

6.5 Summary.

Based on the simulation results, gradient matching layer design with proper acoustic impedance distribution make it possible to fully take advantage of the great potentials offered by PMN-PT single crystals in making ultra-wide broadband transducers. In most frequency range, the transmission coefficient varies between 90-100%, which means that most acoustic energy can be transmitted into the body tissue. For the best design, the matching layer bandwidth can be way above 100%. In fact, for the third type design, a continuous passband window is formed. Such design is particularly well suited for transducers made of the PMN-PT single crystals for which the electromechanical coupling coefficient is over 90% and the total transducer bandwidth can be over 100%. Our new matching layer designs here resolved the problem of narrow passband window from the conventional matching layers. Within the exciting frequency band, single crystal transducers now can send out different frequencies tone-burst or continuous wave with the same high transmission coefficient so that the imaging resolution and penetration depth can be adjusted without changing the transducer. It will also be a great help in the second harmonic imaging technology. This gradient impedance design also provides a universal matching layer, which may be used on ultrasonic transducers of different frequencies. One does not have to always use the quarter wavelength designs, which will greatly increase the fabrication efficiency and reduce the manufacture cost.

Chapter 7

CONCLUSION AND RECOMMENDED FUTURE WORK

7.1 Summary and Conclusions

Medical Ultrasonography is one the most important diagnostic techniques in today's clinical diagnosis. It has been widely used in numerous fields. However, this technique is still in the stage of being developed and optimized. Only some diseases now can be diagnosed by ultrasonic imaging due to the resolution limit. There is a rising demand for higher resolution ultrahigh frequency ultrasonography.

Ultrasonic transducer is the most important component in medical ultrasonic imaging system. One trend in medical ultrasonic transducer design is that transducer operating frequency keeps increasing from commonly used 1–5 MHz to 50 MHz or more. Some recently developed new applications even use transducers of over 100MHz for skin imaging and imaging of eyes. Therefore, designing new high efficiency, low cost high frequency medical ultrasonic transducer has become a pressing task.

An ultrasonic transducer consists of a piezoelectric resonator, backing and matching layer(s). Piezoelectric material is the engine of ultrasonic transducers, it converts electrical energy into mechanical energy and vice versa. The recently discovered PMN-PT or PZT-PT single crystals raised the hope of much better performance transducers because these crystals have very large piezoelectric coefficient and ultra-high electromechanical coupling coefficient.

The backing is used to solve the ringdown problem by absorbing the backward waves, therefore, it is made of materials with very high acoustic impedance and very high damping coefficient.

Matching layer is put in front of the transducer in order to increase the energy transmission efficiency into the imaging medium. The best acoustic impedance matching can be achieved when the thickness of matching layer is a quarter of the wavelength of the central operating frequency and there are defined requirements for the acoustic impedance of the matching layer. The matching layers are usually made of composite materials, whose fabrication becomes harder and harder as the frequency goes up because fine powders can easily trap air bubbles, making it impossible to fabricate high particle loading composites. At present, most of the transducers with center operating frequency higher than 40 MHz are not properly matched due to the lack of matching layer material. One of the main objectives of this thesis is to find new matching layer materials as well as making innovative matching layer designs so that the wide bandwidth nature of transducers made of the new PMN-PT single crystals can be fully exploited.

A new nano-structured TiO_2 material has been developed and characterized in this thesis work. The TiO_2 nano-particles were made into porous nano-structured film at room temperature by adding small amount of Ti^{iV} tetraisopropoxide (TTIP) and diluted using ethanol solution. This new nano-material has higher acoustic impedance than SiO_2 nano-composite and much simplified processing procedure. The material has porous nano-structure with the volume fraction of voids being controlled by the amount of bonding amorphous phase in the material. Its acoustic impedance can be further tuned by heat treatment at elevated temperatures.

In order to precisely measure the acoustic impedance and attenuation information of the new nano-structures thin film material, through-transmission ultrasonic spectroscopy technique based on quarter wavelength matching layer principle has been used. The reflection and transmission pulses within the thin film layer are separated from the successive pulses reflected from the substrate/water interface. From the ratio of spectra obtained from film on substrate and pure substrate only, a peak can be found at the quarter-wavelength frequency, which in turn gives us the sound velocity. The measured results show that this new TiO_2 nano-structured material's acoustic impedance can reach as high as 7.19 MRayls, which is a solid improvement compared to that of the SiO_2 nano-composites developed before.

New matching layer designs with gradient acoustic impedance are also investigated in this thesis work. Finite difference time domain method was used to analyze the wave propagation in the gradient structure. Mur's boundary condition is applied to eliminate the influence of reflections from boundaries to the transmitted waves. We programmed a C++ code based on the principle of numerical FDTD method to simulate the ultrasonic signal transmission in a three region structure: piezoelectric layer, matching layer with gradient acoustic impedance and body tissue. Simulations are conducted with three different acoustic impedance gradients. All results were analyzed in detail and compared. The third gradient type is found to be able to provide the best results in terms of transmission coefficient and bandwidth. An ideal ultra-broadband matching design has been obtained, which can be used for almost all frequencies beyond 20 MHz. Such matching layer with ultra-broadband will make it possible to fully exploit the high electromechanical coupling coefficient of the new piezoelectric PMN-PT single crystals so that transducers with bandwidth over 100% can be produced. Because such matching layer practically has no upper frequency cut-off, it is a universal matching layer that can be used for transducers of any frequency, which can increase the transducer fabrication efficiency and further reduce the manufacture cost. Ultra-broadband transducers can be used in second harmonic imaging which has much better resolution, and one could also generate different frequency waves to image different depth without changing the transducer.

The geometry design and fabrication of such new matching layers were also proposed, but practical fabrication of these matching layers is currently limited by available processing techniques.

7.2 Recommendation for Future Work

There are still many challenges in the field of high frequency medical ultrasonography. With the operating frequency of medical ultrasonic transducer going into ultrahigh frequency band (> 100 MHz), more and more problems emerged. We have tackled one of the important issues, i.e., the matching layer problem, both in terms of innovative designs and new materials development. A nano-structured TiO_2 film have been developed that can have adequate acoustic impedance for making matching layers. A new design using gradient acoustic impedance in the matching produced an excellent super large band matching. However, experimental implementation of the gradient matching design is very challenging with the current thin film processing techniques. Therefore, there are still much work to be done in this field.

For example, in material development, new nano-composite materials with even higher acoustic impedance and low attenuation are still unavailable. Fabricating desired gradient matching layer is another challenge. We have proposed some practical ways but to realize such designs still need extensive experimental research. The most promising may is using porous film with each layer having different degree of porosity. One may also need to use two or more materials, for example PZT porous film plus tungsten-nano-composite, to make the acoustic impedance change from 2-30 MRayls.

Two characterization methods to measure the acoustic properties of thin film materials have been investigated in this thesis. The first one used quarter-wave principle to test thin film on thick substrate, which can separate the reflection and transmission pulses within the thin layer from the successive pulse reflected from the substrate. The measurement provided good results but it is limited to film thickness > 8 microns. For thin films deposited on relatively thin substrates, the signals generated within the film no longer can be separated from reflections within the substrate, for this case, we have developed the second method to measure the acoustic properties of thin film by using phase shift in tone-burst mode. Current experiment results showed that the reliability of this method largely depends on the accuracy of the noise level. Better isolation is needed in order to get reliable results.

We have also explored the possibility of developing attenuation based NDE using ultrasound. To this end, we have derived the attenuation changes caused by delaminations and cracks in multilayer capacitors and actuators. Theoretical calculations indicated that the method is plausible for delaminations but not sensitive to cracks parallel to the wave propagation direction. Such attenuation based ultrasonic NDE method can provide information on delaminations much smaller than the wavelength, hence can be very useful for elevation of small size multilayer capacitors and actuators. There are a lot of works to be done in this direction in order to implement this technique.

Bibliography

Abd-El-Raouf, H. E. (2006). "A Class of Finite Difference Time Domain (FDTD) Techniques for Solving Large Electromagnetic Structures." Internationa RF and Microwave Conference 301-305.

Alvarez-Arenas, T. E. G. (2004). "Acoustic Impedance Matching of Piezoelectric Transducers to the Air." IEEE Transactions on Ultrasonics, Ferroelectrics, and Frequency Control **51**(5): 624-633.

Andrew, W. V., et al. (1994). " Finite-Difference Ttime-Domain of HF Antennas." IEEE Antennas and Propagation Society International Symposium Proceedings **3**: 1418–1421.

Angelsen, A. J. (2000). Ultrasound Imaging: Waves, Signals, and Signal Processing. Trondhejm, Emantec.

Barbé, C. J., F. Arendse, et al. (1997). "Nanocrystalline Titanium Oxide Electrodes for Photovoltaic Applications." Journal of the American Ceramic Society **80**: 3157-3171.

Bouakaz, A., N. De Jong (2003). "Native Tissue Imaging at Superharmonic Frequencies." IEEE Transactions on Ultrasonics, Ferroelectrics, and Frequency Control **50**(5): 496-506.

Brown, L. F., et al. (1997). "Investigation of the Dielectric and Piezoelectric Properties of PMN and PMN-PT Materials for Ultrasonic Transducer Applications." Ultrasonics Symposium Proceedings **1**:561-564.

Brown, L. F. (2000). "The Effects of Material Selection for Backing and Wear Protection/Quarter-wave Matching of Piezoelectric Polymer Ultrasound Transducers." Ultrasonics Symposium Proceedings **2**:1029-1032.

Campbell, S. A., D. C. Gilmer, et al. (1997). "MOSFET Transistors Fabricated with High Permitivity TiO2 dielectrics." IEEE Transactions on Electron Devices **44**(1): 104-109.

Cannata, J. M., T. A. Ritter, et al. (2003). "Design of Efficient, Broadband Single Element Ultrasonic Transducers for Medical Imaging Applications," IEEE Transactions on Ultrasonics, Ferroelectrics, and Frequency Control **50**(11): 1548-1556.

Carotta, M. C., M. Ferroni, et al. (1999). “Preparation and Characterization of Nanostructured Titania Thick Films.” Advanced Materials **11**: 943-946.

Chan, Y. C., et al. (1995). “Nondestructive Detection of Defects in Miniaturized Multilayer Ceramic Capacitors using Digital Speckle Correlation Techniques”, IEEE Transactions on Components, Hybrids, and Manufacturing Technology **18**(3): 677-684.

Chen, J., R. Panda. (2005). “Review: commercialization of piezoelectric single crystals for medical imaging applications.” Ultrasonics Symposium Proceedings **1**:235-240.

Collin, R. E. (1955). “Theory and Design of Wide-Band Multisection Quarter-Wave Transformers.” Proceedings of the IRE **43**(2): 179-185.

Cozzolino, M. J., et al. (1978). “Nondestructive Examination of Multiplayer Capacitors by Neutron Radiography.” Proceedings of IEEE Electronnics & Compupter Technology Conference :327-375.

Cummer, S. A. (2000). “Modeling Electromagnetic Propagation in the Earth-ionosphere Waveguide.” IEEE Transaction on Antennas and Propagation **48**(9): 1420-1429.

Dalapati, G. K., S. Chatterjee, et al. (“Electrical Properties of TiO/sub 2/ Films Deposited on Strained Si/sub 1-y/C/sub y/ Layers.” Electronics Letters **39**(3): 323-324.

De Ana, F. J., M. O'Donnell, (2002). “Ringdown Reduction for An Intraluminal Ultrasound Array Using Depth-dependent Azimuthal Filters.” Ultrasonics Symposium Proceedings **2**:1773-1776.

DeSilets, C. S., J. Fraser and G. S. Kino (1978). “The Design of Efficient Broad-Band Piezoelectric Transducers.” IEEE Transactions on. Sonics and Ultrasonics **25**(3): 115-125.

Draheim, M. R. (1997) “Finite Element Modeling and Experimental Study of Ultrasonic Impedance Matching Layer for Medical Transducers.” The Penn State University.

Engquist, B. and A. Majda (1977). “Absorbing Boundary Conditions for the Numerical Simulation of Waves.” Mathematics of Computation **31**: 629-651.

Foldy, L. L. (1945). “Multiple Scattering Theory of Waves.” Physics Revision **31**: 107-119.

Goll, J. H. and B. A. Auld (1975). “Multilayer Impedance Matching Schemes for Broadbanding of Water Loaded Piezoelectric Transducers and High Q Electric Resonators.” IEEE Transactions on. Sonics and Ultrasonics **22**(1): 52-53.

Grätzel, M. (2001) “Photoelectrochemical Cells.” Nature **414**: 338-344.

Grewe, M. G. (1989). “Acoustic Matching and Backing Layers for Medical Ultrasonic Transducers.” The Penn State University.

Gururaja, T. R. (1994). “Piezoelectrics For Medical Ultrasonic Imaging.” American Ceramic Society Bulletin **73**(5):50-55.

Gururaja, T. R., et al. (1999). “Single Crystal Transducers for Medical Imaging Applications.” Ultrasonics Symposium Proceedings **2**:969-972.

Hackenberger, W., et al. (2003). “Broad Band Single Crystal Transducer for Contrast Agent Harmonic Imaging.” Ultrasonics Symposium Proceedings **1**:778-781.

Hadimioglu, B., B. T. Khuri-Yakub (). “Polymer Films as Acoustic Matching Layers.” Ultrasonics Symposium Proceedings **3**:1337-1340.

Haller, M. I., B. T. Khuri-Yakub (1993). “Tapered acoustic matching layers.” IEEE Ultrasonics Symposium Proceedings : 505-508

Hoskins, P. R., A. Thrush, et al. (2003). Diagnostic Ultrsound. London, Greenwich Medical Media Limited.

Inoue, T., M. Ohta and S. Takahashi (1987). “Design of Ultrasonic Transducers with Multiple Acoustic Matching Layers for Medical Application.” IEEE Transactions on Ultrasonics, Ferroelectrics and Frequency Control **34**(1):8-16.

Kahn, S. R., R. W. Checkaneck (1983). “Acoustic Emission Testing of Multilayer Ceramic Capacitors.” IEEE Transactions on Components, Hybrids, and Manufacturing Technology **4**: 517-526.

Kinsler, L. E. (1982). Fundamentals of Acoustics. New York, John Wiley & Sons.

Krimholtz, R., D. A. Leedom and D. L. Mathaei (1971). “New Equivalent Circuits for Elementary Piezoelectric Transducers.” Electrical Letters **6**: 398-399

Leedom, D. A., R. Krimholtz and D. L. Mathaei (1971). “Equivalent Circuits for Transducers Having Arbitrary Even-or-Odd-Symmetry Piezoelectric Excitation.” IEEE Transactions on. Sonics and Ultrasonics **18**: 128-141

Li, Y., J. A. Zagzebski (2000). “Computer Model for Harmonic Ultrasound Imaging.” IEEE Transactions on Ultrasonics, Ferroelectrics, and Frequency Control **47**(4): 1000-1013.

Lockwood, G. R., D. H. Turnball, et al. (1996). “Beyond 30 MHz [Applications of High-frequency Ultrasound Imaging].” IEEE Engineering in Medicine and Biology Magazine **15**(6): 60-71.

Love, G. R., G. J. Ewell (1978). “Acoustic Microscopy of Ceramic Capacitors.” IEEE Transactions on Components, Hybrids, and Manufacturing Technology **3**: 251-257.

Lu, X. M., T. L. Rhyne, et al. (1998). “Transducer Material Characterization by Transmission Coefficient Measurements.” Ultrasonics Symposium Proceedings **2**:1061-1064.

Luk, K. M., et al. (2003). “The Absorbing Boundary Algorithm in General FDTD Method.” IEEE Antennas and Propagation Society International Symposium Proceedings **1**:345-348.

Mason, W. P. (1964). Physical Acoustics. New York, Academic Press.

Mur, G. (1981). “Absorbing Boundary Conditions for the Finite Difference Approximation of the Time-Domain Electromagnetic-Field Equations,” IEEE Transactions on Electromagnetic Compatibility **23**:377-382.

Pavlin, C. J. and F. S. Foster (1995). Ultrasound Biomicroscopy of the Eye. Berlin, Springer-Verlag.

Rehrig, P. W., et al. (2003). “Status of Piezoelectric Single Crystal Growth for Medical Transducer Applications.” Ultrasonics Symposium Proceedings **1**:766-769.

Ritter, T., et al. (2000). “Single Crystal PZN/PT-Polymer Composites for Ultrasound Transducer Applications.” IEEE Transactions on Ultrasonics, Ferroelectrics, and Frequency Control **47**(4): 792-800.

Roy, A. (1987). “Diffraction of Elastic Waves by an Elliptic Crack-II.” International Journal in Engineering and Science **25**: 155-160.

Sato, S., H. Katsura and K. Kobayashi (2002). “Experimental investigation of phased array using tapered matching layers.” IEEE Ultrasonics Symposium Proceedings : 1235-1238.

Shen, C. C., P. C. Li (2001). “Tissue harmonic image analysis based on spatial covariance.” IEEE Transactions on Ultrasonics, Ferroelectrics, and Frequency Control **48**(6): 1648-1656.

Shlager, K. L., J. B. Schneider (1995). “A Selective Survey of the Finite-Difference Time-Domain Literature.” IEEE Antennas and Propagation Magazine **37**(4):39-57.

Shung, K. K., M. B. Smith, et al. (1992). Principles of Medical Imaging. San Diego, Academic Press.

Shung, K. K. and M. Zipparo (1996). “Ultrasonic Transducers and Arrays.” IEEE Engineering in Medicine and Biology Magazine **15**: 20.

Sotiropoulos, D. A., J. D. Achenbach (1988). “Reflection of Elastic Waves by A Distribution of Coplanar Cracks.” Journal of Acoustic Society of America **84**: 752-759.

Spiiggs, R. S., A. H. Cronshagen (1976). “Nondestructive X-Ray Inspection of Ceramic-Chip Capacitors for Delaminations.” Reliability Physics Symposium Proceedings :157-163.

Stumpf, F. B. (1980). Analytical Acoustics. Ann Arbor, Ann Arbor Science.

Sung, M. R., H. Jung (2007). “Piezoelectric Single Crystal for Medical Ultrasound Transducer.” Ultrasonics Symposium Proceedings :300-304.

Sung, M. R., et al. (2004). “Multilayer PMN-PT Single Crystal Transducer for Medical Application.” Ultrasonics Symposium Proceedings **12**:1021-1024.

Taflove, A. (1980). "Application of the Finite-difference Time-domain Method to Sinusoidal Steady State Electromagnetic Penetration Problems." IEEE Transactions on Electromagnetic Compatibility **22**: 191–202.

Taflove, A., et al. (2000). "FDTD-How Complex A Problem Can We Solve?." IEEE Antennas and Propagation Society International Symposium Proceedings **3**: 1641–1642.

Vogel, R. F. (1985). “Transducers with Screen Printed Matching Layers.” IEEE Ultrasonics Symposium Proceedings: 704-709.

Vos, H. J., et al. (2003). “Transducer for Harmonic Intravascular Ultrasound Imaging.” IEEE Transactions on Ultrasonics, Ferroelectrics, and Frequency Control **52**(12): 2418-2422.

Wang, H., W. Cao, et al. (2001). “High Frequency Properties of Passive Materials for Ultrasound Transducers.” IEEE Transactions on Ultrasonics, Ferroelectrics, and Frequency Control **48**(1): 78-84.

Wang, H., W. Cao, et al. (2003). “Characterization of Ultra-thin Quarter-wavelength Matching Layers of High Frequency Ultrasonic Transducers.” IEEE Ultrasonics Symposium Proceedings: 1048-1051.

Wang, H., W. Cao (2004). “Characterizing Ultra-thin Matching Layers of High-frequency Ultrasonic Transducer Based On Impedance Matching Principle.” IEEE Transactions on Ultrasonics, Ferroelectrics, and Frequency Control **51**(2): 211-215.

Wang, H., W. Cao, et al. (2004). “Silicon Oxide Colloidal/Polymer Nano-Composite for Matching Layer of High Frequency Medical Ultrasonic Transducers.” Applied Physics Letters **85**(24): 5998-6000.

Wojcik, G., et al. (1998). “A Study of Second Harmonic Generation by Focused Medical Transducer Pulses.” Ultrasonics Symposium Proceedings **2**:1583-1588.

Wright, D. A., D. A. Williams (1968) “The Crystal and Molecular Structure of Titanium Tetramethoxide.” Acta Crystallographica. **B24**: 1107-1114.

Xiang, S. H., Y. T. Zhang (). “Matching Layer Optimization Between Ultrasound Transducer and Human Tissues.” IEEE 17th Engineering in Medicine and Biology Society Proceedings **1**: 623.

Yee, K. S. (1966). “Numerical Solution of Initial Boundary Value Problems Involving Maxwell’s Equations in Isotropic Media.” IEEE Transaction on Antennas and Propagation **14**(5): 302-307.

Yu, W. (2006). Parallel Finite-Difference Time-Domain Method. Norwood, Artech House.

Zagzebski, J. A. (1996). Essentials of Ultrasound Physics. St. Louis, Mosby.

Zhang, C., J. D. Achenbach (1991). “Effective Wave Velocity and Attenuation in a Material with Distributed Penny-Shaped Cracks.” International Journal of Solids Structures **27**(6): 751-767.

Zhang, D., J. Dowing, et al. (2006). “Room-Temperature Preparation of Nanocrystalline TiO2 Films and the Influence of Surface Properties on Dye-Sensitized Solar Energy Conversion” Journal of Physical Chemistry B **110**: 21890-21898.

Zhang, D., T. Yoshida, et al. (2006). “Room-Temperature Synthesis of Porous Nanoparticulate TiO2 Films for Flexible Dye-Sensitized Solar Cells” Advanced Functional Materials **16**: 1228-1234.

Zhou, Q .F., J. H. Cha, et al. (2006). “P3Q-4 Nanocomposite Matching Layers for High Frequency Ultrasound Transducers.” IEEE Ultrasonics Symposium Proceedings : 2365-2368.

Zhou, H., et al. (2006). "Two-mode-interference Switching in Photonic Crystal Waveguides." IEEE Biophotonics, Nanophotonics and Metamaterials International Symposium Proceedings: 332–334.

Zhu, J., W. Cao (2006). “Ultrasonic Attenuation and Velocity Changes in Multilayer Structures Containing Multiple Delaminations.” Materials Evaluation **64**(4): 417-422.

Zhu, J., W. Cao (2007). "Ultrasonic Wave Propagation In Multilayer Ceramic Capacitors Structure Containing Cracks." Materials Evaluation **65**(11): 1135-1138.

Zhu, J., W. Cao (2007). "Fabrication and Characterization of Nanocrystalline TiO2-polymer Composite Matching Layers." IEEE Ultrasonics Symposium Proceedings : 1917-1920.

Zipparo, M. J. (1996) "Very High Frequency (50-100MHz) Ultrasonic Transducers For Medical Imaging Applications." The Penn State University.

Appendix

C++ Code for FDTD Simulation

```
int temp, temp2, temp3;
int i,j,m;
double Axis_T;
double ZZ[5000];
int freqloop, freqnumber;
boolean MaxN, MinN;


freqloop=5000000;
freqnumber=(Freq-freqloop)/100000;


for (m = 0; m <= freqnumber; m++)
{
        MaxN=false;
        MinN=false;
        freqloop=5000000+m*100000;
        Wavelength_T=S_T/freqloop;
        Wavelength_M=S_M/freqloop;
        Wavelength_W=S_W/freqloop;
        Wavelength_T_P=Wavelength_T/DeltaX;
```

```
        Wavelength_M_P=Wavelength_M/DeltaX;
        Wavelength_W_P=Wavelength_W/DeltaX;

        for (i = 0; i <= 5000; i++) {
         ZZ[i]=0;
        }

        for (i = 1; i <= i_M; i++) {
         ZZ[i]=Impedance_T-i*(Impedance_T-Impedance_W)/(i_M+1);
        }
// initialization of u (the initial displacement of the string)
        Axis_T=0;
 for (i = 0; i <= (i_T+i_M+i_W); i++) {
         U_0[i]=0;
 }
 temp=floor(Wavelength_T_P);
 Axis_T=DeltaT;
// initialization of u1
for (i = 0; i <= (i_T+i_M+i_W); i++) {
         U_1[i]=0;
 }
U_1[0]=sin(2*Ppi*freqloop*DeltaT);
```

```
// the loop of ui
for (i = 2; i <= i_Time; i++)
{
        Axis_T=i*DeltaT;
        U_2[0]=sin(2*Ppi*freqloop*Axis_T);
        U_2[0]=0;
        U_2[i_T+i_M+i_W]=0;
        U_2[1]=2*(1-
(DeltaT*S_T/DeltaX)*(DeltaT*S_T/DeltaX))*U_1[1]+(DeltaT*S_T/DeltaX)*(DeltaT*S
_T/DeltaX)*(U_1[2]+U_1[0])-U_0[1];
        for (j = 1; j < i_T; j++)
        {
                U_2[j]=2*(1-
(DeltaT*S_T/DeltaX)*(DeltaT*S_T/DeltaX))*U_1[j]+(DeltaT*S_T/DeltaX)*(DeltaT*S
_T/DeltaX)*(U_1[j+1]+U_1[j-1])-U_0[j];
        }
        U_2[i_T]=(2-
(DeltaT*Impedance_T/DeltaX)*(DeltaT*Impedance_T/DeltaX)-
(DeltaT*ZZ[1]/DeltaX)*(DeltaT*ZZ[1]/DeltaX))*U_1[i_T]+(DeltaT*ZZ[1]/DeltaX)*(D
eltaT*ZZ[1]/DeltaX)*U_1[i_T+1]+(DeltaT*Impedance_T/DeltaX)*(DeltaT*Impedance_
T/DeltaX)*U_1[i_T-1]-U_0[i_T];      for (j = (i_T+1); j < (i_T+i_M); j++)
    {
```

```
            U_2[j]=(2-(DeltaT*ZZ[j-i_T]/DeltaX)*(DeltaT*ZZ[j-i_T]/DeltaX)-(DeltaT*ZZ[j-i_T+1]/DeltaX)*(DeltaT*ZZ[j-i_T+1]/DeltaX))*U_1[j]+(DeltaT*ZZ[j-i_T+1]/DeltaX)*(DeltaT*ZZ[j-i_T+1]/DeltaX)*U_1[j+1]+(DeltaT*ZZ[j-i_T]/DeltaX)*(DeltaT*ZZ[j-i_T]/DeltaX)*U_1[j-1]-U_0[j];
        }
        U_2[i_T+i_M]=(2-(DeltaT*Impedance_W/DeltaX)*(DeltaT*Impedance_W/DeltaX)-(DeltaT*ZZ[i_M]/DeltaX)*(DeltaT*ZZ[i_M]/DeltaX))*U_1[i_T+i_M]+(DeltaT*Impedance_W/DeltaX)*(DeltaT*Impedance_W/DeltaX)*U_1[i_T+i_M+1]+(DeltaT*ZZ[i_M]/DeltaX)*(DeltaT*ZZ[i_M]/DeltaX)*U_1[i_T+i_M-1]-U_0[i_T+i_M];
        for (j = (i_T+i_M+1); j < (i_T+i_M+i_W); j++)
        {
            U_2[j]=2*(1-(DeltaT*S_W/DeltaX)*(DeltaT*S_W/DeltaX))*U_1[j]+(DeltaT*S_W/DeltaX)*(DeltaT*S_W/DeltaX)*(U_1[j+1]+U_1[j-1])-U_0[j];
            U_2[i_T+i_M+i_W]=U_1[i_T+i_M+i_W-1]+(S_W*DeltaT-DeltaX)*(U_2[i_T+i_M+i_W-1]-U_1[i_T+i_M+i_W])/(S_W*DeltaT+DeltaX);

            if (i==(i_Time*17/18))
            {
             j = i_T+i_M+10;
             CString szWriteData;
             _itoa(freqloop, chTemp1, 10);
```

```
szWriteData += CString(chTemp1)+" ";
while ((j < (i_T+i_M+i_W)) && (MaxN==false))
{
        if ((U_2[j]>0) && (U_2[j]>U_2[j+1]) && (U_2[j-1]<U_2[j])
&& (U_2[j+1]>U_2[j+2]) && (U_2[j-1]>U_2[j-2]))
        {
                _gcvt(U_2[j], 15, buffer2);
                szWriteData += CString(buffer2)+" ";
                MaxN=true;
        }
        j++;
}
j = i_T+i_M+2;
while ((j < (i_T+i_M+i_W)) && (MinN==false))
{
        if ((U_2[j]<0) && (U_2[j]<U_2[j+1]) && (U_2[j-1]>U_2[j])
&& (U_2[j+1]<U_2[j+2]) && (U_2[j-1]<U_2[j-2]))
        {
                _gcvt(U_2[j], 15, buffer);
                szWriteData += CString(buffer)+" ";
                MinN=true;
        }
        j++;
```

```
}
szWriteData += szNewLine;
CFile ResultDataFile;
char* pFileName = "C:\\test.dat";
if (ResultDataFile.Open(pFileName,
CFile::modeCreate+CFile::modeNoTruncate+CFile::modeWrite))
{
DWORD dwActual =
ResultDataFile.SeekToEnd();
ResultDataFile.Write((LPCSTR)szWriteData,szWriteData.GetLength());
ResultDataFile.Close();
}
}
for (j = 0; j <= (i_T+i_M+i_W); j++)
{
U_0[j]=U_1[j];
U_1[j]=U_2[j];
U_2[j]=0;
}
}
}
```

VITA

Jie Zhu

Jie Zhu was born in Huaiying, Jiangsu Province, P.R. China in 1976. He received his B.S. in computer science from Nanjing University in 1998. He continued his study in electrical engineering department of Nanjing University and received his M.S. in 2002. In 2004 he joined intercollege graduate program in material engineering of the Pennsylvania State University as a graduate student. His research interests are focused on ultrasonic material characterization and ultrasonic transducer matching layer design. He is a member of the IEEE.